

Thermal and Deposition Modeling Update for the Canister Deposition Field Demonstration

Spent Fuel and Waste Disposition

***Prepared for
U.S. Department of Energy
Spent Fuel and Waste Science and
Technology***

Pacific Northwest National Laboratory

**SR Suffield
BJ Jensen**

**WA Perkins
D Carpenter-Graffy**

***September 1, 2023*
M2SF-23PN010208018
PNNL-34772**

DISCLAIMER

This information was prepared as an account of work sponsored by an agency of the U.S. Government. Neither the U.S. Government nor any agency thereof, nor any of their employees, makes any warranty, expressed or implied, or assumes any legal liability or responsibility for the accuracy, completeness, or usefulness, of any information, apparatus, product, or process disclosed, or represents that its use would not infringe privately owned rights. References herein to any specific commercial product, process, or service by trade name, trade mark, manufacturer, or otherwise, does not necessarily constitute or imply its endorsement, recommendation, or favoring by the U.S. Government or any agency thereof. The views and opinions of authors expressed herein do not necessarily state or reflect those of the U.S. Government or any agency thereof.

SUMMARY

This report provides an update on the thermal and deposition modeling being performed in support of the Canister Deposition Field Demonstration (CDFD). The goal of the CDFD testing is to collect deposition measurements on the surface of the dry shielded canister (DSC) to aid in chloride-induced stress corrosion cracking (CISCC) research. Ideally, this testing will occur in a marine coastal environment, but at the time of this report, no official site has been selected. The CDFD plans to use the NUHOMS[®] Advanced Horizontal Storage Module – High Seismic (AHSM-HS) with a 32PTH2 canister. The spent nuclear fuel (SNF) assemblies will be mimicked with electrical heaters. Canisters are currently being outfitted with these heaters and tested at Sandia National Laboratories (SNL). Thermal modeling was conducted to ensure the electrical heaters are representative of the temperature distribution found within a storage system with SNF. Temperature comparison plots show that the canister surface temperatures between the baseline SNF model and heater assembly models are similar.

Thermal transients were also run with the SNF baseline and heater assembly models to compare the thermal response of the canister due to differences in canister mass between a 32PTH2 canister loaded with electrical heaters instead of SNF. The SNF canister is estimated to be 2 times heavier than the heater assembly canister. Transient cases were run for both changing ambient temperatures and changing wind conditions. The modeling results indicate that there is no significant difference in the thermal response of the system with electrical heaters compared to a system loaded with SNF within a 12-hour time frame (environment conditions are expected to fluctuate between daytime and evening conditions). Based on the thermal transient results, there is no need to try to account for any canister mass differences with the electrical heaters.

A canister-only model with prototypic heaters was used to simulate SNL testing from 4.8 kW to 35 kW heat load test conditions. The resulting overall peak canister shell and peak heater temperatures predicted by the model compared well with the peak test measurements. An uncertainty analysis was run with the canister-only model at the 9.6 kW and 35 kW heat loads to determine the uncertainty in the temperature predictions. Results show that the canister surface temperature results predicted by the model were either within range or slightly overpredicted the measured thermocouple value. Both heat loads showed the same temperature profile as the experiment.

Deposition models were built to evaluate particulate deposition on SNF canisters. The CDFD testing will help to validate these models, which will then be used to plan and inform on-site test programs and provide predictive models for the timing and occurrence of canister CISCC. Steady state simulations were run using both the SNF baseline and heater assembly models, and the resulting predicted canister deposition is within 1.5% between the SNF and heater assembly model. An uncertainty analysis was run with the AHSM-HS heater assembly model to determine the uncertainty in the deposition predictions and provide a range over which the predicted deposition efficiency is expected to vary due to environmental variance (i.e., wind speed and direction, ambient temperature, relative humidity [RH]). The resulting mean canister deposition efficiency was predicted to be 10% with a +10%/-7% variance.

An approach for looking at the impact of particle resuspension was developed based on particle detachment theory and calculating a critical shear velocity for a sea salt aerosol (SSA) particle. Preliminary modeling shows that a small number of particles may be impacted by particle resuspension, but further work is needed to explore this topic. These results are preliminary and will be dependent on characterizing a particle size and distribution once a CDFD site has been selected. A preliminary site model was constructed to support a planned upcoming ambient aerosol characterization campaign. The long-term plan is to develop a site model to provide boundary conditions, such as wind speed and direction, to the detailed stand-alone deposition models of the AHSM-HS heater assembly models. Modeling was conducted to demonstrate how to account for wind in the stand-alone AHSM-HS model based on pressure differences at the inlets and outlets due to wind. Once a CDFD site has been chosen, a model specific to that site will be developed using lessons learned from the current modeling activity.

This page is intentionally left blank.

ACKNOWLEDGMENTS

This work was conducted as part of the U.S. Department of Energy Spent Fuel and Waste Science and Technology campaign. The authors thank Ned Larson of the Department of Energy for his support and leadership in this research program.

The authors would like to thank Sam Durbin, Dominic Fascitelli, and Greg Koenig of Sandia National Laboratories (SNL) for the information about their experiment. We would also like to thank Charles Bryan, Rebecca Schaller, and Andrew Knight of SNL for collaborating with us. We appreciate the information sharing provided by all the SNL staff members who were involved. Also, we would like to thank Prakash Narayanan and others at Orano for design information to support research related to the Orano TN NUHOMS[®] 32PTH2 dry shielded canisters and the associated horizontal storage modules. The authors would also like to thank our project management at Pacific Northwest National Laboratory, Brady Hanson and Steve Ross.

This page is intentionally left blank.

CONTENTS

SUMMARY	iii
ACKNOWLEDGMENTS	v
ACRONYMS	xiii
1. INTRODUCTION	1
2. THERMAL MODELING	3
2.1 Baseline Model Updates	3
2.1.1 Inlet Geometry	4
2.1.2 Measured Gap between the Canister Shell and Basket Rails	4
2.1.3 Updated Model Results	6
2.2 Heater Model Updates	6
2.2.1 Single AHSM-HS Model	6
2.2.2 Ambient Conditions	10
2.2.3 Comparisons with Baseline Model	10
2.2.4 Three AHSM-HS Model	15
2.3 Thermal Transients	17
2.3.1 Ambient Temperature Transients	17
2.3.1 Wind Transients	20
2.4 Canister Model with Prototypic Heaters	22
2.4.1 Experimental Setup	22
2.4.2 Model Description	22
2.4.3 Uncertainty Analysis	23
2.4.4 Comparisons with Measured TC Data	25
3. LINKAGE BETWEEN THERMAL AND DEPOSITION MODELS	31
4. DEPOSITION MODELING	33
4.1 Background on Previous Work	33
4.2 Deposition Comparisons with Baseline Model	33
4.3 Particle Distribution	38
4.4 Three AHSM-HS Deposition Model	41
4.4.1 Comparisons with Stand-Alone AHSM-HS Models	42
4.5 Particle Resuspension	43
4.5.1 Particle Detachment Theory	43
4.5.2 Material Properties	44
4.5.3 Computed Resuspension Conditions	47
4.5.4 Additional Physics	49
4.6 Site Model	49
4.6.1 Fire Dynamics Simulator	52
4.6.2 Application to Sequim Site	52
4.7 Connecting the Site Model and Stand-Alone Model	59
4.7.1 STAR-CCM+ Wind Effects Model	60
4.7.2 FDS Wind Effects Model	63

4.7.3	Stand-Alone AHSM-HS Model	67
4.7.4	Inlet Mass Flow Results	67
4.7.5	Three AHSM-HS Wind Effects Models	69
4.8	Uncertainty Analysis	73
4.8.1	Deposition Efficiency Results	74
4.8.2	Shear Velocity Results	75
5.	CONCLUSIONS AND RECOMMENDATIONS	81
6.	REFERENCES	83

FIGURES

Figure 2-1.	Cross-Sectional View of AHSM-HS with 32PTH2 Canister CAD Geometry.....	3
Figure 2-2.	Cross-Sectional View of the AHSM-HS through the Center of the Inlets for (a) the Original Geometry and (b) the Updated Tapered Entry (Air Regions Shown in Blue).....	4
Figure 2-3.	Measured Basket-to-Canister Gaps (0° Top of Canister) from Fascitelli and Durbin (2023).....	5
Figure 2-4.	AHSM-HS Single-Module Model Geometry (a) Overall Geometry and (b) Cross-Sectional View Near the Center of the AHSM-HS.....	7
Figure 2-5.	Loading Map for Heater Model.....	7
Figure 2-6.	Radial Temperature Contour Plot Through the Center of the 10 kW Case.....	9
Figure 2-7.	Radial Temperature Contour Plot Through the Center of the 40 kW Case.....	9
Figure 2-8.	Two Views of DSC Temperature Contour Plots at 10 kW—(Left) Baseline Model and (Right) Heater Assembly Model.....	10
Figure 2-9.	Two Views of DSC Temperature Contour Plots at 40 kW—(Left) Baseline Model and (Right) Heater Assembly Model.....	11
Figure 2-10.	Axial Canister Surface Temperatures at 10 kW.....	12
Figure 2-11.	Axial Canister Surface Temperatures at 40 kW.....	13
Figure 2-12.	Radial Canister Surface Temperatures at 10 kW Near the Center of the Heated Length.	14
Figure 2-13.	Radial Canister Surface Temperatures at 40 kW Near the Center of the Heated Length.	14
Figure 2-14.	AHSM-HS Three-Module Model Geometry.....	15
Figure 2-15.	Three AHSM-HS Thermal Model – DSC Temperature Contour Plot.....	17
Figure 2-16.	Canister Surface Temperature for Ambient Temperature Transients.....	18
Figure 2-17.	Average Canister Surface Temperature for Ambient Temperature Transients.....	19
Figure 2-18.	Peak Fuel or Heater Temperature for Ambient Temperature Transients.....	20
Figure 2-19.	Canister Surface Temperature for Wind Transients at 10 kW.....	21
Figure 2-20.	Peak Fuel or Heater Temperature for Wind Transients at 10 kW.....	21
Figure 2-21.	Cross-Sectional Plot of Heater Locations from Fascitelli and Durbin (2023).....	22
Figure 2-22.	Cartoon showing the extremes in canister – basket rail gap ovality (not to scale).....	24
Figure 2-23.	Illustration of a and b, the Major and Minor Diameters of the Ellipse.....	25
Figure 2-24.	Canister Temperatures at 9.6 kW Heat Load.....	26
Figure 2-25.	Canister Temperatures at 35 kW Heat Load.....	27
Figure 2-26.	Heater temperature with 9.6 kW heat load.....	28
Figure 2-27.	Heater Temperature with 35 kW Heat Load.....	29
Figure 2-28.	Comparison of Maximum Heater and Canister Surface Temperatures between Test and Model.....	30

Figure 4-1.	Canister Particle Deposition Contour Plots at the 40 kW Heat Load for (a) SNF Baseline Model and (b) Heater Assembly Model.....	35
Figure 4-2.	Particle Size Distribution on the Canister Surface at 10 kW	36
Figure 4-3.	Particle Size Distribution on the Canister Surface at 40 kW	36
Figure 4-4.	Angular Particle Location Distribution on the Canister Surface at 10 kW	37
Figure 4-5.	Angular Particle Location Distribution on the Canister Surface at 40 kW	37
Figure 4-6.	Particle Size Distribution on the Canister Surface at 10 kW for Particle Distribution Sensitivity	39
Figure 4-7.	Particle Size Distribution on the Canister Surface at 40 kW for Particle Distribution Sensitivity	39
Figure 4-8.	Angular Particle Location Distribution on the Canister Surface at 10 kW for Particle Distribution Sensitivity	40
Figure 4-9.	Angular Particle Location Distribution on the Canister Surface at 40 kW for Particle Distribution Sensitivity	40
Figure 4-10.	Canister Deposition for Three AHSM-HS 32PTH2 Heater Assembly Model	41
Figure 4-11.	Total Deposition for Three AHSM-HS 32PTH2 Heater Assembly Model	42
Figure 4-12.	Schematic Depicting Particle Detachment Theory	44
Figure 4-13.	Expected Precipitate Particle Size Based on Sea Spray Droplet Size at Creation.	46
Figure 4-14.	Computed Tabor Parameter over the Expected Precipitate Particle Size Range.	48
Figure 4-15.	Critical Shear Velocity Computed Using the DMT Adhesion Model and Assuming that Particles Can Roll on the Substrate.....	48
Figure 4-16.	PNNL-Sequim and Locations of Nearby Weather Stations.....	51
Figure 4-17.	PNNL-Sequim Campus.	53
Figure 4-18.	LIDAR-Derived DTM (Above) and DSM, (Below) Available for the PNNL-Sequim Site.	54
Figure 4-19.	Simulated Instantaneous Velocity in the Field along an East–West Plane (Above) and at 30 m Elevation (Below).....	55
Figure 4-20.	Massless Particle Tracks (or Streak Lines) from a Simulation with an Ambient Westerly Wind of 5 m/s Imposed.....	56
Figure 4-21.	Simulated Wind Speed (Above) and Direction (Below) at the Robb House and Field Sites.....	57
Figure 4-22.	Simulated Instantaneous Velocity around an Imaginary AHSM-HS in the Field Along an East–West Plane (Above) and at an Elevation of 30 m (Below).....	58
Figure 4-23.	5 m/s Wind Blowing Directly at the AHSM-HS Inlets.	59
Figure 4-24.	5 m/s Wind Blowing from Behind the AHSM-HS Inlets.	60
Figure 4-25.	External Boundary Size Sensitivity Study Results for the STAR-CCM+ Wind Effects Model.....	60
Figure 4-26.	External Boundary Mesh Size Sensitivity Study Results for the STAR-CCM+ Wind Effects Model.....	61

Figure 4-27.	Geometry for STAR-CCM+ Wind Effects Model.....	62
Figure 4-28.	Cross-Sectional Velocity Vector Plot through the Center of an Inlet on the AHSM-HS for the STAR-CCM+ Wind Effects Model	63
Figure 4-29.	Cross Section View of Mesh for the FDS Wind Effects Model	63
Figure 4-30.	Example of FDS Wind Effects Pressure Probe Locations.....	64
Figure 4-31.	Velocity Vector Plot for Flow Around the AHSM-HS for the FDS Wind Effects Model.....	65
Figure 4-32.	AHSM-HS Inlet and Outlet Numbering Scheme.....	67
Figure 4-33.	Total Mass Flow at AHSM-HS Inlets at 0 kW	68
Figure 4-34.	Total Mass Flow at AHSM-HS Inlets at 40 kW	69
Figure 4-35.	Velocity Vector Plot for Flow Around the three-Module AHSM-HS in FDS at 5 m/s and 0-Degrees.....	70
Figure 4-36.	Velocity Vector Plot for Flow at the Inlets Elevation for the three-Module AHSM-HS in STAR-CCM+ at 5 m/s and 0-Degrees.....	71
Figure 4-37.	Three-Module AHSM-HS Inlet and Outlet Numbering Scheme.....	72
Figure 4-38.	Total Mass Flow at Three-Module AHSM-HS Inlets at 0 kW	73
Figure 4-39.	LHS Analysis Results for Total and Canister Deposition.....	74
Figure 4-40.	Proposed Sampling Layout from Knight et al. (2023).....	75
Figure 4-41.	Resulting Plot for Particle Deposition and Shear Velocity at the Sampling Locations for 10 kW Heat Load and Natural Convection Flow.....	76
Figure 4-42.	LHS Analysis 0 kW Heat Load Results for Shear Velocity	77
Figure 4-43.	LHS Analysis 10 kW Heat Load Results for Shear Velocity	77
Figure 4-44.	LHS Analysis 40 kW Heat Load Results for Shear Velocity	78
Figure 4-45.	0 kW Heat Load Results for Particle Resuspension	79
Figure 4-46.	10 kW Heat Load Results for Particle Resuspension	79
Figure 4-47.	40 kW Heat Load Results for Particle Resuspension	80

TABLES

Table 2-1. Measured Gap between the Canister Shell and Basket Rails (0° Top of Canister)..... 6

Table 2-2. Updated Baseline Model Results 6

Table 2-3. Three Phase Power Distribution for Heater Model..... 8

Table 2-4. Emissivity Measurements for CFD Heater Rods 8

Table 2-5. Temperature Results for Single AHSM-HS Heater Assembly Model..... 8

Table 2-6. Canister Temperature Results 16

Table 2-7. Heater Rod Temperature and Inlet Mass Flow Results..... 16

Table 2-8. Heater Rod Temperature and Inlet Mass Flow Results..... 17

Table 2-9. Perturbation Parameters 23

Table 4-1. Resulting Deposition Comparison for AHSM-HS 32PTH2 Models 34

Table 4-2. Resulting Deposition Comparison for AHSM-HS 32PTH2 Models 38

Table 4-3. Three AHSM-HS Model Deposition Results..... 43

Table 4-4. Salt Precipitate Particle Size Estimated from Sea Spray Droplet Size at Creation. 46

Table 4-5. Particle and Substrate Physical Properties 47

Table 4-6. FDS Wind Effects Pressure Difference Results..... 65

Table 4-7. FDS Three-Module Wind Effects Pressure Difference Results..... 71

Table 4-8. Perturbation Parameters 74

ACRONYMS

AHSM-HS	Advanced Horizontal Storage Module – High Seismic
CAD	computer-aided design
CDFD	Canister Deposition Field Demonstration
CFD	computational fluid dynamics
CISCC	chloride-induced stress corrosion cracking
DSC	dry shielded canister
DSM	digital surface model
DTM	digital terrain model
FDS	Fire Dynamics Simulator
ISFSI	Independent Spent Fuel Storage Installation
LES	large eddy simulation
LHS	Latin hypercube sampling
LIDAR	Light Detection and Ranging
MCRL	Marine and Coastal Research Laboratory
NIST	U.S. National Institute of Standards and Technology
NRC	Nuclear Regulatory Commission
PNNL	Pacific Northwest National Laboratory
RANS	Reynolds-averaged Navier-Stokes
RH	relative humidity
SNF	spent nuclear fuel
SNL	Sandia National Laboratories
SSA	sea salt aerosol
TC	thermocouple

This page is intentionally left blank.

THERMAL AND DEPOSITION MODELING UPDATE OF THE CANISTER DEPOSITION FIELD DEMONSTRATION

1. INTRODUCTION

The goal of the Canister Deposition Field Demonstration (CDFD) is to collect surface deposition measurements over an extended time period on a dual-purpose canister to aid chloride-induced stress corrosion cracking (CISCC) research. The plan is to conduct the test in a marine coastal environment, but at the time of this report, no official site has been selected. The CDFD plans to use the NUHOMS® Advanced Horizontal Storage Module – High Seismic (AHSM-HS) with a 32PTH2 canister. To avoid worker exposure and to facilitate surface measurements, the spent nuclear fuel (SNF) assemblies will be mimicked by electrical heaters. Multiple storage modules are planned to be included to test multiple decay heat loads. A high heat load, low heat load, and no heat load canister will be incorporated into a connected set of three AHSM-HS modules. The no heat load canister will serve as a control, with deposition on this canister mainly driven by wind effects.

Updates to previously developed thermal and deposition models (Suffield 2021, Suffield 2022) are presented in this report along with current model results. Development of these models will continue. The thermal modeling was conducted to ensure the electrical heaters were representative of the thermal environment found within an SNF storage system and to verify that heat flux to the control canister (no heat load) was minimized. The deposition models were built from the thermal models and are being developed to predict the particulate deposition on SNF canisters. To understand environmental effects, such as wind on the storage system, initial wind effects models and a site wide model were also developed. Since no specific site has been selected, a site model of the Pacific Northwest National Laboratory (PNNL)-Sequim campus was constructed to support a future ambient aerosols sampling campaign that is planned for the Sequim location. The sampling campaign will measure quantity, chemical composition, and size of ambient aerosols at select locations within the PNNL-Sequim campus.

Section 2 presents the updated thermal models and results. Section 3 describes the linkage between the thermal and deposition modeling. Section 4 presents updates to the deposition modeling along with the latest model results. Section 5 summarizes the conclusions and recommendations from this work, and Section 6 lists the references.

This page is intentionally left blank.

2. THERMAL MODELING

Two model types are described in this section, baseline models and heater models. A baseline computational fluid dynamics (CFD) model of the 32PTH2 canister in a NUHOMS® AHSM-HS was constructed using the commercial software STAR-CCM+ (Siemens PLM Software 2022). The baseline model included SNF assemblies, which were modeled as single regions within each channel box in the basket. This model provided baseline temperature profiles that were compared against the heater assembly model. In the heater assembly model, the SNF assemblies were replaced by electrical heaters. The electrical heater parts were modeled in detail. The heater assembly model was expanded to a three AHSM-HS model to consider approaches to insulation between modules. A brief description of the models and preliminary temperature results are given in this section.

2.1 Baseline Model Updates

The baseline model of the NUHOMS® AHSM-HS with a 32PTH2 canister included SNF. The AHSM-HS and 32PTH2 canister model was built with information provided by Orano under a non-disclosure agreement. A cross-sectional plot of the computer-aided design (CAD) geometry for a single storage module is shown in Figure 2-1. The CAD geometry was generated using the commercial CAD software SolidWorks (Dassault Systemes SolidWorks Corp. 2021). Updates to the baseline model are described in this section.

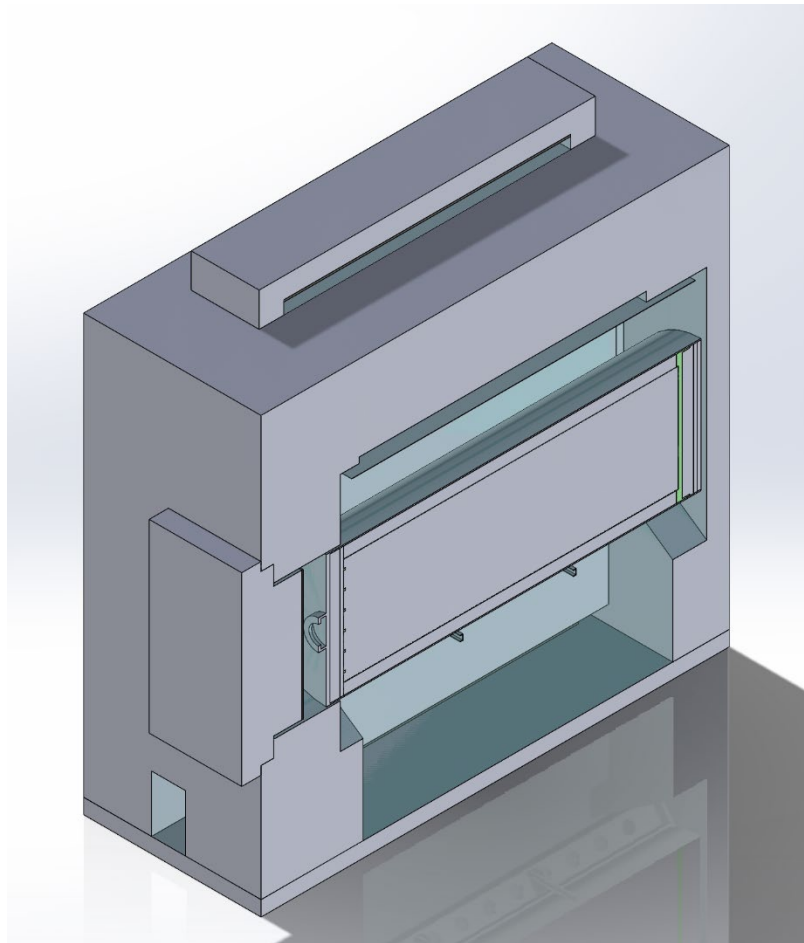


Figure 2-1. Cross-Sectional View of AHSM-HS with 32PTH2 Canister CAD Geometry

2.1.1 Inlet Geometry

The original baseline model reported in Suffield et al. (2022) was updated to correct the inlet geometry for the model. The original baseline model did not include a tapered entry. A comparison of the updated tapered inlet geometry with the older non-tapered entry is shown in Figure 2-2, which shows a cross-sectional view of the AHSM-HS assemblies through the center of the inlets. The air regions are shown in blue.

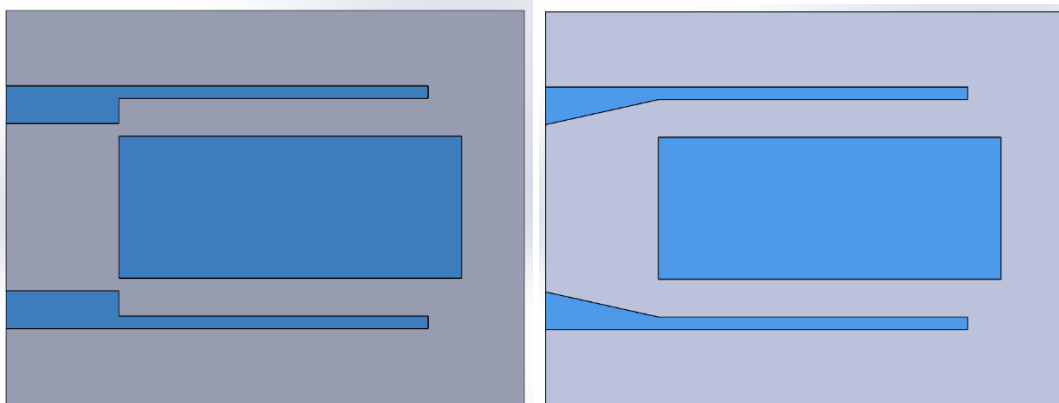


Figure 2-2. Cross-Sectional View of the AHSM-HS through the Center of the Inlets for (a) the Original Geometry and (b) the Updated Tapered Entry (Air Regions Shown in Blue)

2.1.2 Measured Gap between the Canister Shell and Basket Rails

In the 32PTH2 canister, extruded aluminum sections are used to fill the space between the basket assembly and the inner diameter of the canister. The gap between these transition rails and the inside of the canister was measured by Sandia National Laboratories (SNL) at ambient temperature and different heat loads. The resulting measurements are shown in Figure 2-3 (Fascitelli and Durbin 2023). The gap varies with angular position, with 0-degrees referring to the top of the canister with respect to gravity. The 9.6 kW and 35 kW measured gaps were used in the model to represent the 10 kW and 40 kW heat loads, respectively. Table 2-1 lists the resulting measurements provided as boundary conditions to the baseline model. The ambient gap is also listed in Table 2-1, and it was used for modeling the no heat canister with electrical heaters. Due to thermal expansion, these gaps will close further as power level is increased, but for now, the measurements at 9.6 kW were incorporated into the baseline model and were used for predictions at higher power levels.

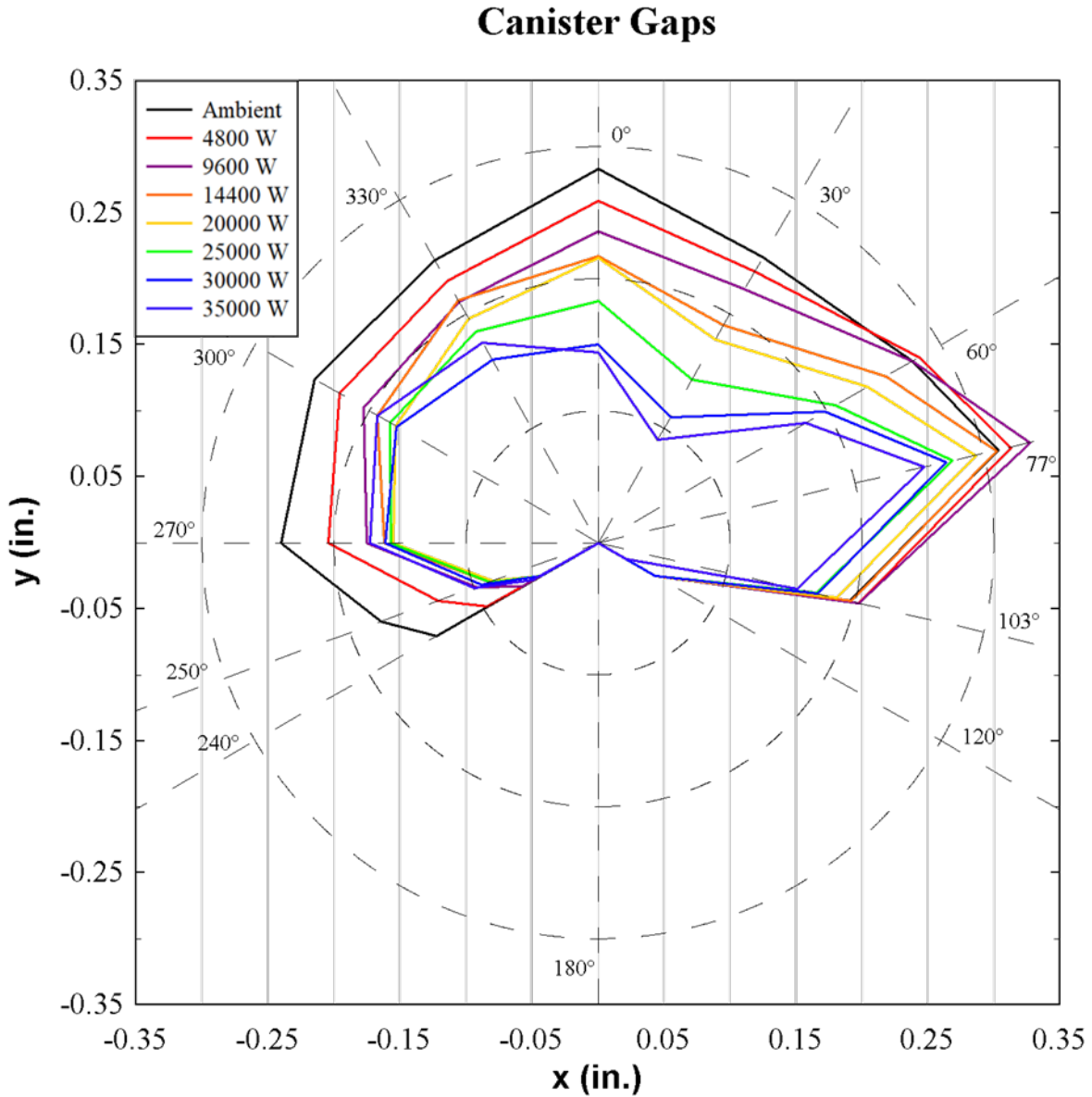


Figure 2-3. Measured Basket-to-Canister Gaps (0° Top of Canister) from Fascitelli and Durbin (2023)

Table 2-1. Measured Gap between the Canister Shell and Basket Rails (0° Top of Canister)

Gap Measurements (in.)			
Degrees	Ambient	9.6 kW	35 kW
0	0.30	0.24	0.14
30	0.27	0.22	0.09
60	0.28	0.28	0.18
77	0.31	0.34	0.25
103	0.23	0.20	0.16
120	0.06	0.05	0.03
180	0.00	0.00	0.00
240	0.14	0.07	0.06
250	0.16	0.10	0.10
270	0.20	0.18	0.17
300	0.19	0.21	0.19
330	0.23	0.21	0.18
360	0.30	0.24	0.14

2.1.3 Updated Model Results

The STAR-CCM+ model was updated with the tapered inlet entry and with the measured rail-canister gaps shown in Table 2-1. The updated baseline model with SNF was run assuming dry air at an ambient temperature of 100°F (37.8°C). Updated results are shown in Table 2-2.

Table 2-2. Updated Baseline Model Results

Heat Load (kW)	Peak Cladding Temperature (°C)
10	173
40	434

2.2 Heater Model Updates

For the CFD project, the SNF assemblies within the 32PTH2 DSC will be mimicked with electrical heater assemblies. The heater assemblies are being designed by SNL. This section describes updates to the previously developed thermal model of the AHSM-HS overpack with a 32PTH2 canister loaded with electrical heaters (Suffield et al. 2022).

2.2.1 Single AHSM-HS Model

The single-module AHSM-HS 32PTH2 with heater assembly model was modified to reflect the latest tapered entry to the inlets and measured gaps between the canister shell and basket rails that were also applied to the baseline SNF model and described in Section 2.1. The overpack geometry was also updated to incorporate the latest insulation design. For the single AHSM-HS model, the insulation is assumed to be located along the exterior walls. It is important to note that the single AHSM-HS model is not representative of the actual configuration since the three modules will be connected but is intended to provide a simplified model for development, comparisons, and sensitivity studies. Figure 2-4 shows the geometry for the updated single-module model.

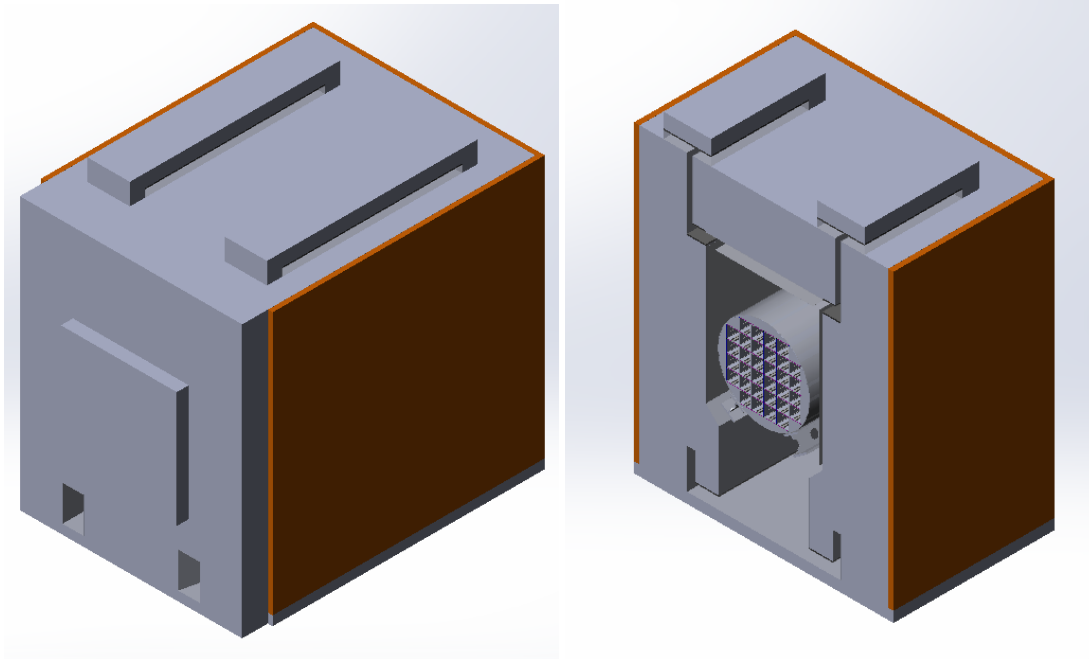


Figure 2-4. AHSM-HS Single-Module Model Geometry (a) Overall Geometry and (b) Cross-Sectional View Near the Center of the AHSM-HS

2.2.1.1 Loading Configuration

The baseline models with SNF use a three-zone loading pattern from the Final Safety Analysis Report that is appropriate for balancing shielding optimization with fuel temperature. For the electrically heated case, shielding is not an issue, and the goal instead is to maximize heater life while using a loading that works effectively with the three-phase power supply. The heater model was updated to reflect the latest power distribution provided by SNL. The planned loading configuration consists of three horizontally stacked zones and is shown in Figure 2-5 and Table 2-3. The power is uniformly distributed among the heaters within a zone (i.e. for the high heat case in zone A, each heater receives 1400 W).

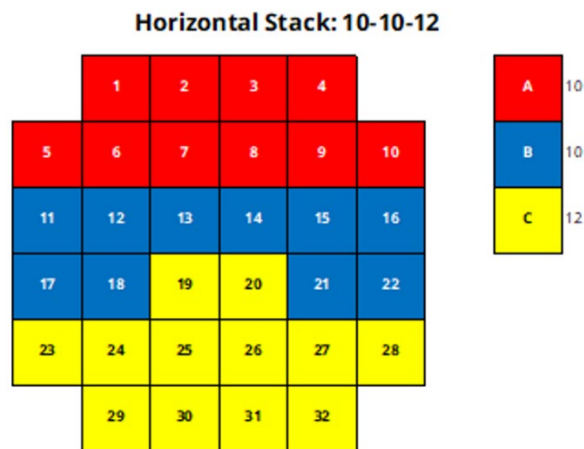


Figure 2-5. Loading Map for Heater Model

Table 2-3. Three Phase Power Distribution for Heater Model

Zone	A	B	C	Sum
Number of heaters	10	10	12	
Canister 1 40 kW (High Heat) Zone Power, W	14,000	14,000	12,000	40,000
Canister 2 10 kW (Low Heat) Zone Power, W	3,500	3,500	3,000	10,000

2.2.1.2 Measured Heater Rod Emissivity

SNL provided emissivity measurements for the surface of the CFD heater rods. These measurements were taken on coupons sectioned from a heater rod assembly. It is important to note that the emissivity was measured from a new, never used heater rod, and SNL plans to measure a used heater rod in the future. Due to the high temperatures seen by the heater rods, the surface of the heater rods may oxidize and increase the emissivity of the heater surface. The resulting measured emissivity is shown in Table 2-4. The measured value should be conservative for the heater rod temperatures since any oxidation would be expected to increase the surface emissivity and lower the rod temperature. The STAR-CCM+ single-module with heater assembly model was updated with the measured heater rod emissivity.

Table 2-4. Emissivity Measurements for CFD Heater Rods

Hardware Component	Measured Emissivity
Heater Rods	0.47

2.2.1.3 Temperature Results

The updated single AHSM-HS 32PTH2 heater assembly model was run for both the low, 10 kW, heat load, and the high, 40 kW, heat load. Both models were run assuming a conservative ambient temperature of 38°C (100°F). Resulting component temperatures are shown in Table 2-5. A radial cross-sectional temperature contour plot near the center of the AHSM-HS is shown for the high and low heat load cases in Figure 2-6 and Figure 2-7, respectively.

Table 2-5. Temperature Results for Single AHSM-HS Heater Assembly Model

Heat Load [kW]	Avg Canister Temp [°C]	Max Canister Temp [°C]	Avg Lid Temp [°C]	Max Lid Temp [°C]	Avg Fuel Temp [°C]	Max Fuel Temp [°C]
10	102	115	64	72	245	272
40	210	256	112	132	487	545

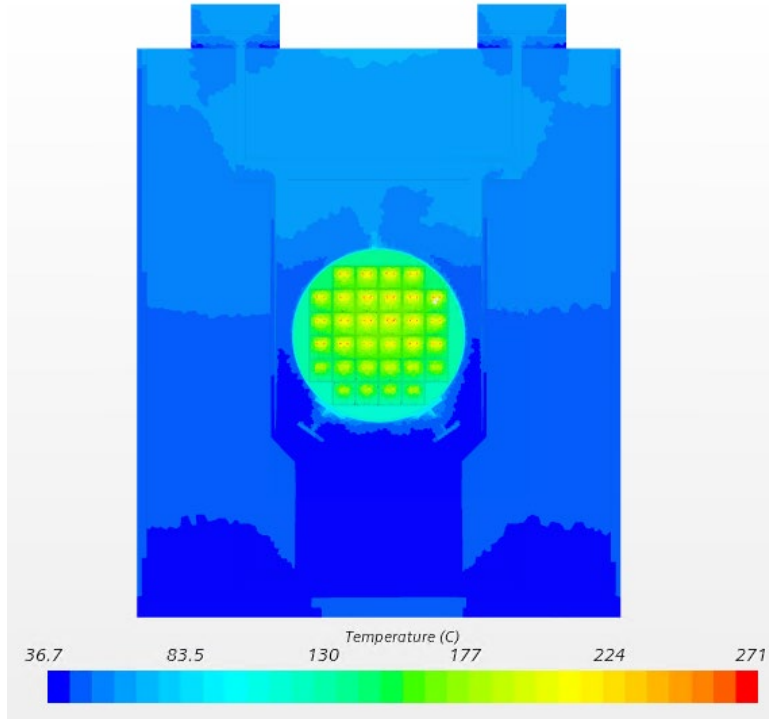


Figure 2-6. Radial Temperature Contour Plot Through the Center of the 10 kW Case

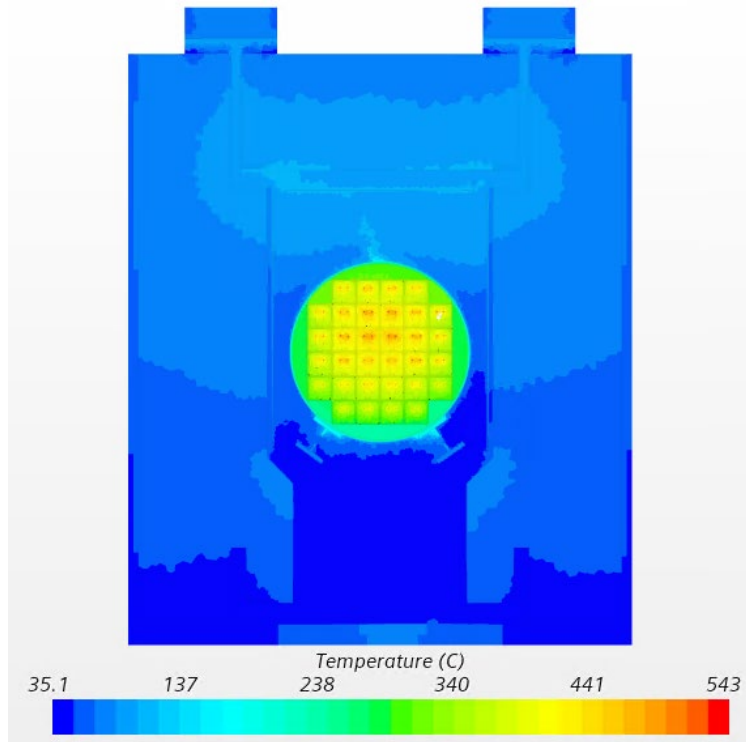


Figure 2-7. Radial Temperature Contour Plot Through the Center of the 40 kW Case

2.2.2 Ambient Conditions

At the time of this report, no official site has been selected for the CDFD project. The plan is to conduct the test in a marine coastal environment. To run the models at more realistic ambient conditions, meteorological data near a coastal Independent Spent Fuel Storage Installation (ISFSI) was analyzed to determine the average yearly ambient temperature and relative humidity (RH). The resulting average yearly ambient temperature of 63.4°F (17.4°C) and RH of 66.9% were estimated. These values represent expected ambient conditions at a coastal site, and once a site is officially selected, the ambient conditions of the site will be analyzed to produce updated boundary conditions for the models.

2.2.3 Comparisons with Baseline Model

The updated baseline SNF model and updated heater model were run at an ambient temperature of 63.4°F (17.4°C) and RH of 66.9%. Canister surface temperature contour plots comparing the new heater model and the updated baseline SNF model are shown in Figure 2-8 and Figure 2-9. Axial temperature comparisons were made along the canister surface at the 0-, 90-, 180-, and 270-degree locations with 0 degrees corresponding to the top of the canister. Figure 2-10 shows the resulting plots for 10 kW and Figure 2-11 shows the resulting plots for 40 kW. A radial comparison of temperatures was also plotted circumferentially along the canister surface near the center of the heated length and is shown in Figure 2-12 for the low heat load and Figure 2-13 for the high heat load.

Both models include tapered inlets and measured rail-canister gaps. The heater model includes the latest heat loading configuration described in Section 2.2.1.1 and the measured heater rod emissivity. All plots show that the temperatures between the baseline SNF model and heater assembly models are similar.

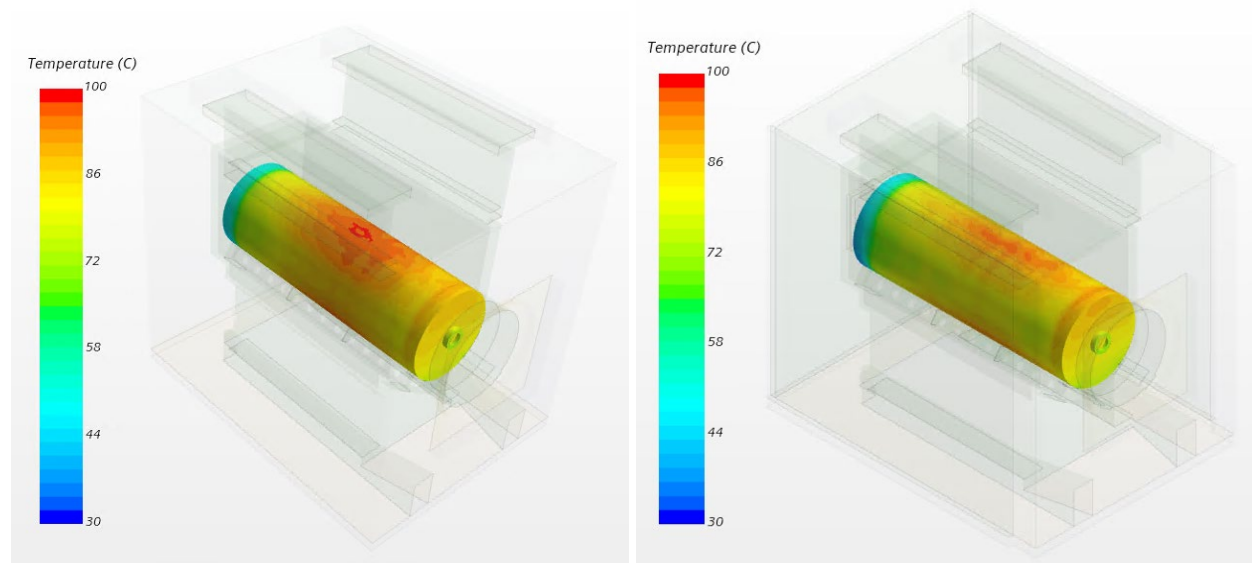


Figure 2-8. Two Views of DSC Temperature Contour Plots at 10 kW—(Left) Baseline Model and (Right) Heater Assembly Model

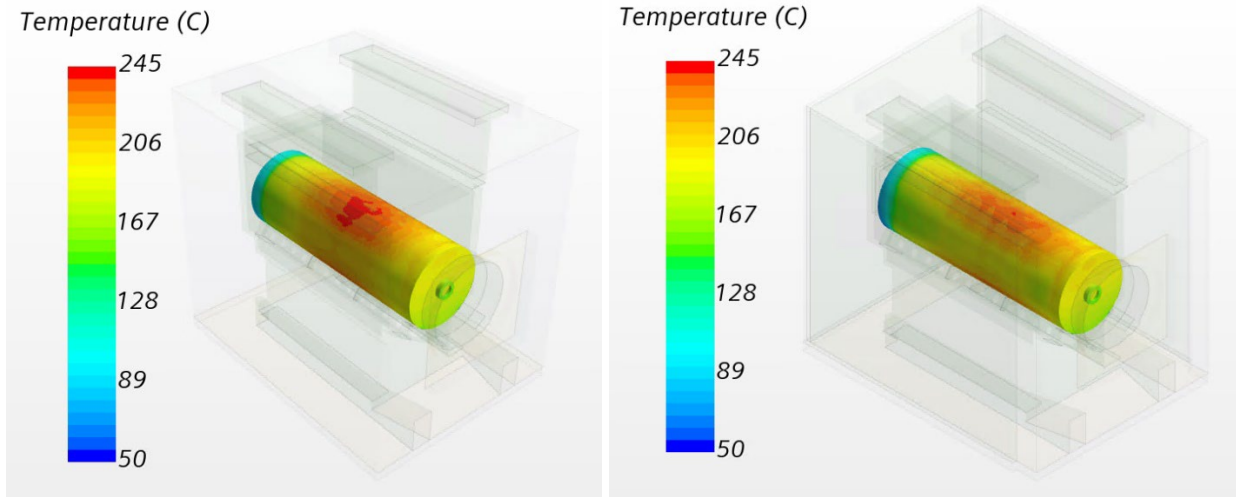


Figure 2-9. Two Views of DSC Temperature Contour Plots at 40 kW—(Left) Baseline Model and (Right) Heater Assembly Model

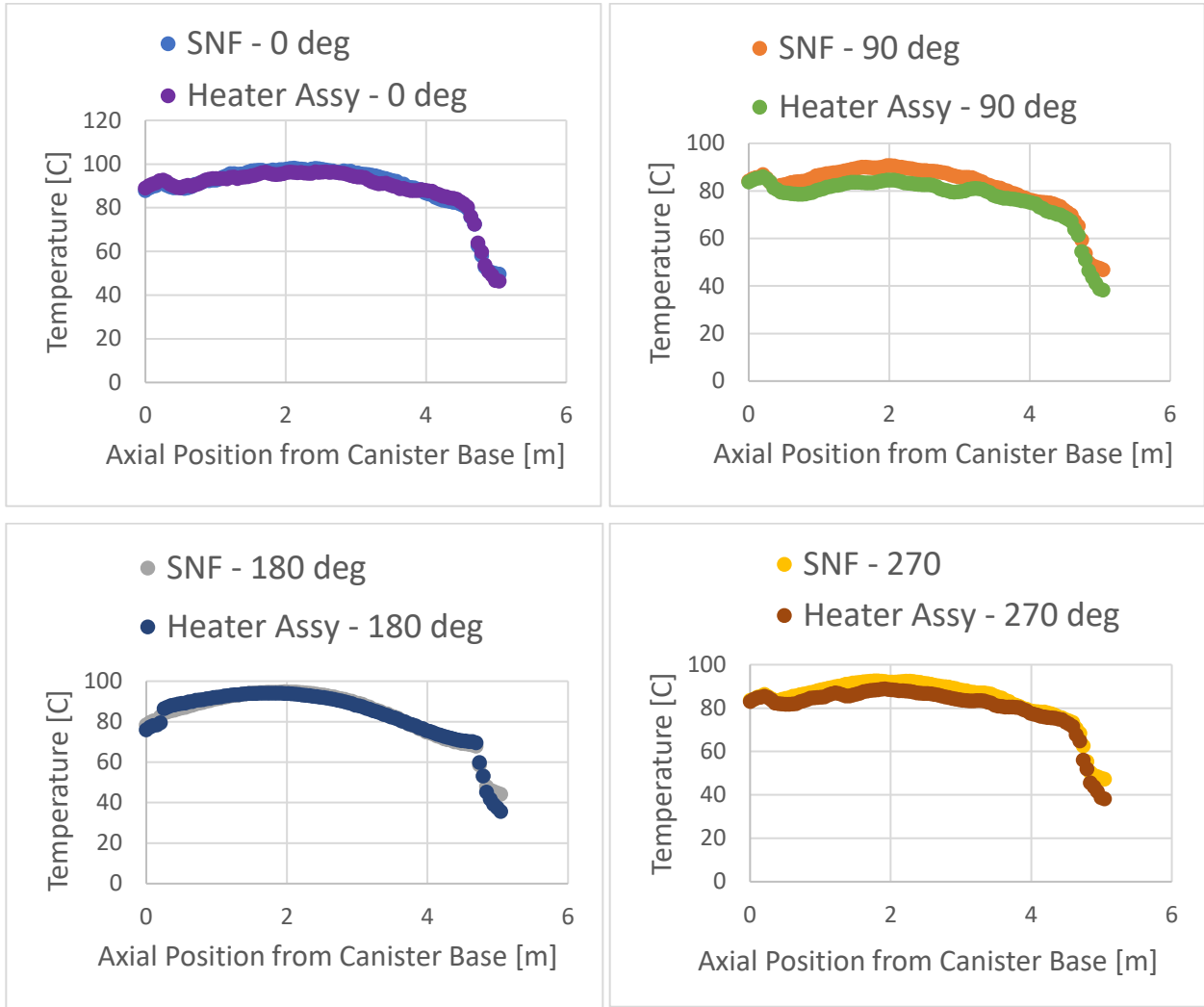


Figure 2-10. Axial Canister Surface Temperatures at 10 kW

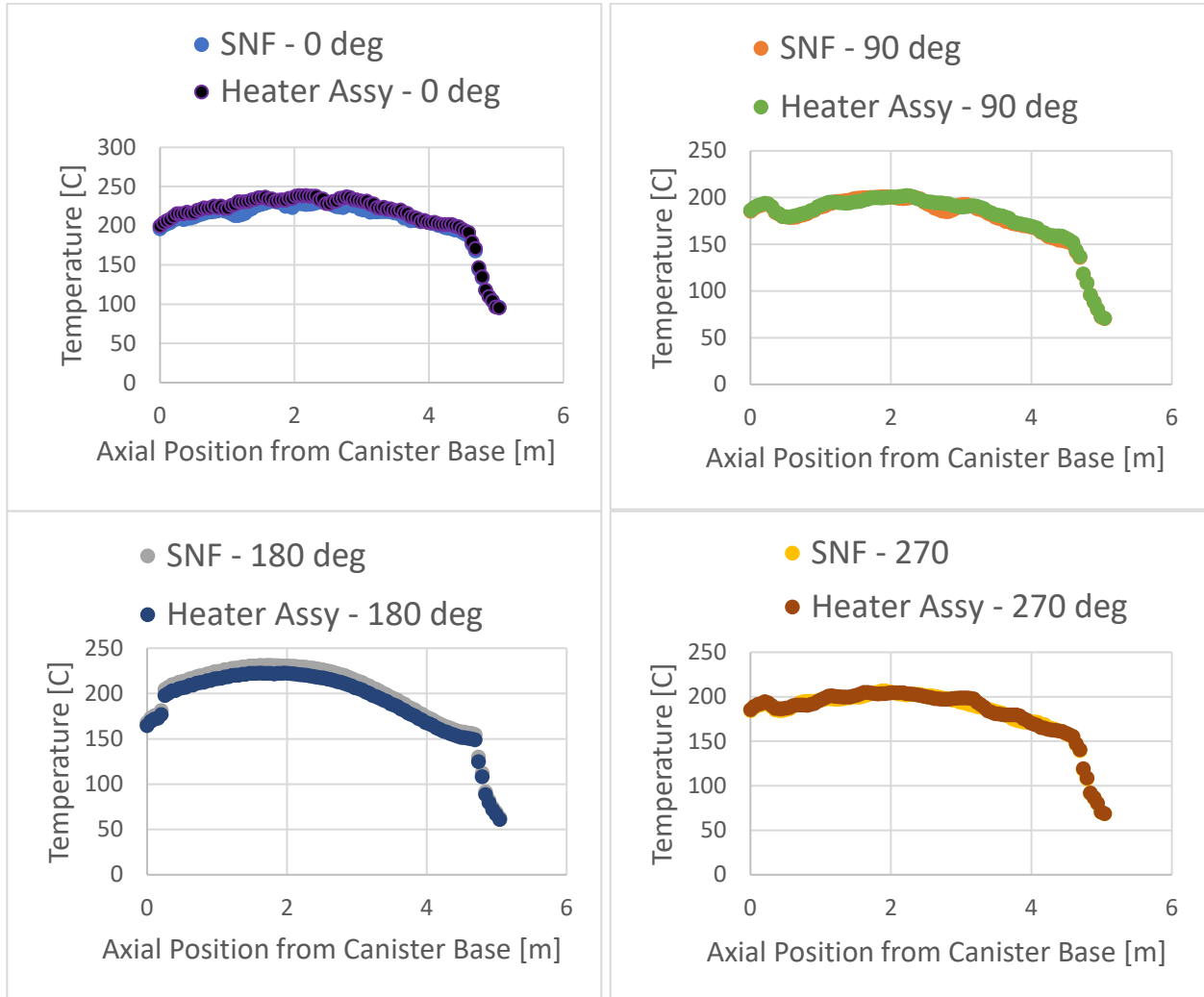


Figure 2-11. Axial Canister Surface Temperatures at 40 kW

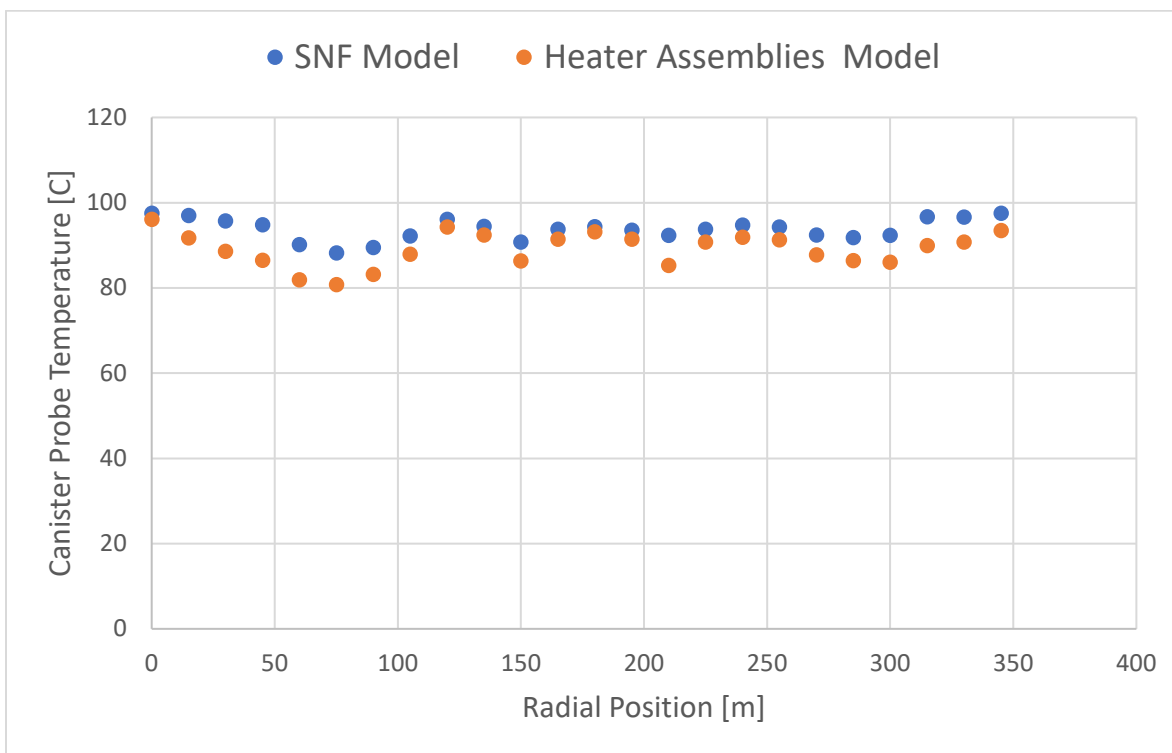


Figure 2-12. Radial Canister Surface Temperatures at 10 kW Near the Center of the Heated Length

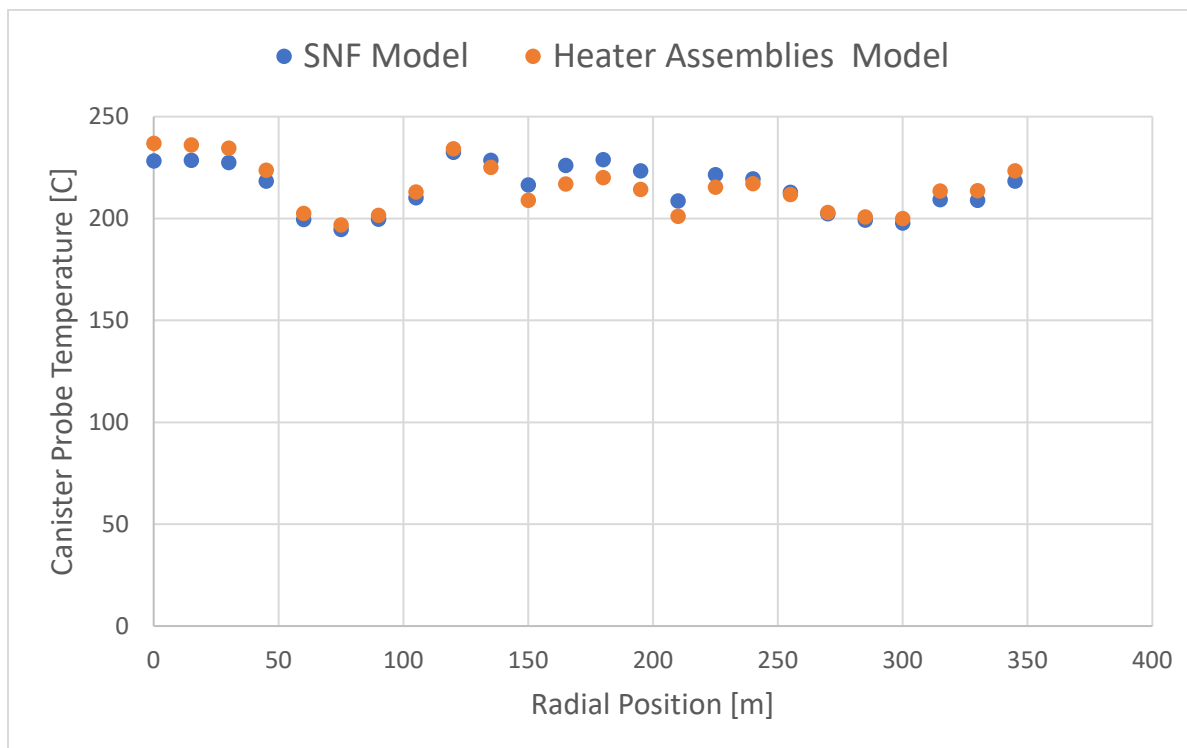


Figure 2-13. Radial Canister Surface Temperatures at 40 kW Near the Center of the Heated Length

2.2.4 Three AHSM-HS Model

The current plan for the CFD project is to have three modules assembled in a row, with each module having a unique heat load. There will be a “high heat” canister with a heat load of 40 kW, a “low heat” canister with a heat load of 10 kW, and a “no heat” canister that is unheated. The NUHOMS[®] AHSMs are designed to be attached to an adjacent module with shared inlets. This creates a challenge for isolating modules from each other, especially for the no heat canister. An intermediate wall was designed to be placed between modules to help isolate the heated canisters from the no heat canister. The previously developed three AHSM-HS model (Suffield et al., 2022) was updated to reflect the previously described changes to the single AHSM-HS heater assembly model (tapered inlets, measured canister to basket rails gap, heat loading configuration, and heater rod emissivity). The ambient gap listed in Table 2-1 was applied to the no heat canister, the 9.6 kW gap was applied to the low heat canister (10 kW), and the 35 kW gap was applied to the high heat canister (40 kW). Figure 2-14 shows the geometry for the three AHSM-HS heater assembly model. The insulation of the internal intermediate wall is nonsymmetrical.

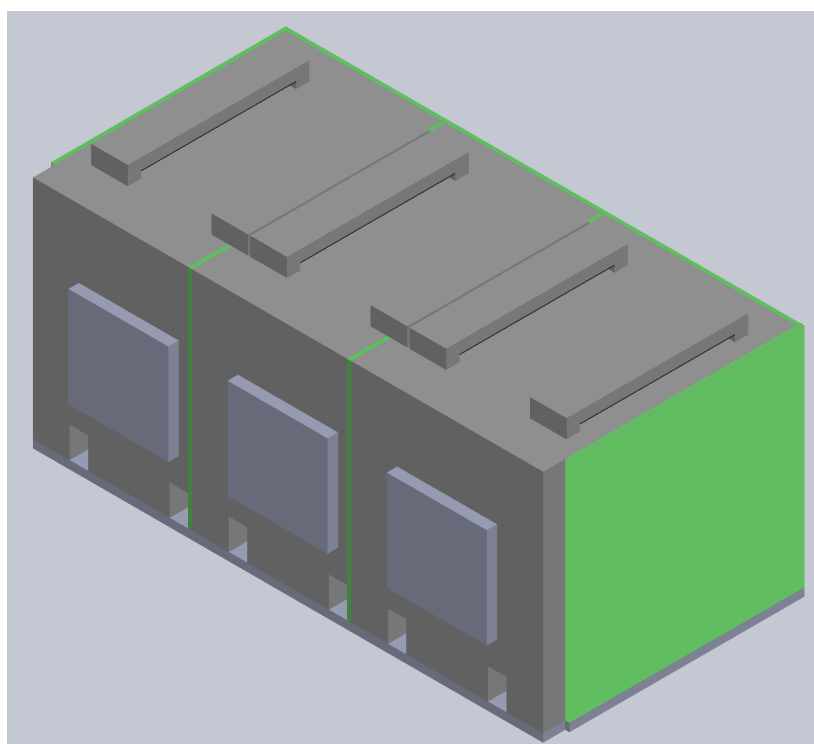


Figure 2-14. AHSM-HS Three-Module Model Geometry

2.2.4.1 Temperature Results

The updated three AHSM-HS 32PTH2 heater assembly model was run assuming an ambient temperature of 63.4°F (17.4°C) and RH of 66.9% based on the estimated average ambient conditions for a coastal site (Section 2.2.2). Resulting temperatures are shown for the canister in Table 2-6. Table 2-7 compares the maximum heater rod temperatures and resulting mass flow rates at the inlets between the single and three AHSM-HS 32PTH2 heater assembly models. The resulting canister temperatures are within 9°C on the high heat canister and within 6°C for the low heat canister between the two models. The peak heater rod temperatures are within 5°C on the low heat canister but are 25°C higher on the three-module model compared to the single-module model. This could be due to the differences in the insulation placement between the models—the single AHSM-HS model had the outer insulation placed symmetrically along the outer side walls, but the inner insulation within the three-module design is nonsymmetrical. Even with the differences in temperatures, especially for the high heat canister, the mass flow rate of air entering the

inlets is identical between the two models for all heat loads. A temperature contour plot of canister surface temperatures is shown in Figure 2-15. The high heat load module is located on the far left, the no heat module in the center, and the low heat module on the far right. Overall, the single AHSM-HS 32PTH2 heater assembly model reasonably represents the canister temperatures and air mass flow rates for each heat load.

Table 2-6. Canister Temperature Results

Model	Total Heat Load (kW)	Avg Canister Temp (°C)			Max Canister Temp (°C)		
		High Heat Canister	No Heat Canister	Low Heat Canister	High Heat Canister	No Heat Canister	Low Heat Canister
Three AHSM-HS	50	177	20	76	249	21	103
Single AHSM-HS	40	173	-	-	240	-	-
Single AHSM-HS	0	-	20	-	-	21	-
Single AHSM-HS	10	-	-	76	-	-	97

Table 2-7. Heater Rod Temperature and Inlet Mass Flow Results

Model	Total Heat Load (kW)	Max Heater Rod Temp (°C)			Mass Flow at Inlets (kg/s)		
		High Heat Canister	No Heat Canister	Low Heat Canister	High Heat Canister	No Heat Canister	Low Heat Canister
Three AHSM-HS	50	561	21	268	0.68	0.19	0.45
Single AHSM-HS	40	536	-	-	0.68	-	-
Single AHSM-HS	0	-	20	-	-	0.19	-
Single AHSM-HS	10	-	-	263	-	-	0.45

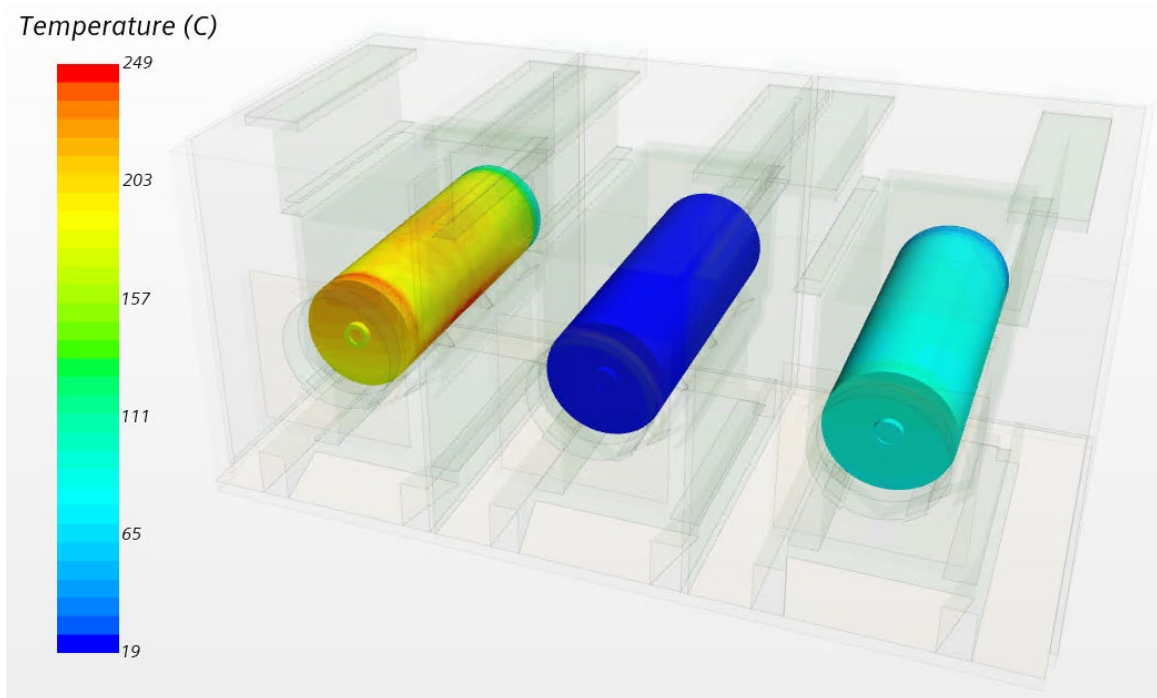


Figure 2-15. Three AHSM-HS Thermal Model – DSC Temperature Contour Plot

2.3 Thermal Transients

There are differences in canister mass between a 32PTH2 canister loaded with electrical heaters instead of SNF. The total canister mass was estimated in Fascitelli and Durbin (2023); the SNF canister is approximately 49,000 kg (108,000 lb), and the heater assembly canister is approximately 23,000 kg (51,000 lb). Based on these weight estimates, the SNF canister is approximately 2 times heavier than the heater assembly canister when loaded. This difference in mass between the two canisters could translate to differences in the thermal response of the canister to changes that would affect the temperature profile of the canister surface, such as ambient temperature or air flow into the storage module. Transient analyses were run to compare the thermal response between the baseline SNF and the heater models.

2.3.1 Ambient Temperature Transients

Ambient temperature varies due to diurnal cycles over a 24-hour period. To look at the effect of temperature swings during a 24-hour period, the average evening and daytime conditions shown in Table 2-8 were assumed. The average ambient temperatures and RH in Table 2-8 are expected to represent a typical upper temperature swing for a coastal site.

Table 2-8. Heater Rod Temperature and Inlet Mass Flow Results

	Avg Temp [°C]	Avg RH
Evening	14.6	83.5
Daytime	23.8	54.3
Δ	9.2	29.2

To initialize the transient simulation, each model was run at steady state conditions based on the evening conditions shown in Table 2-8. The transient analysis was then started assuming the daytime conditions

given in Table 2-8 and was run out a maximum of 12 hours. The STAR-CCM+ adaptive timestep model was used to automatically adjust the timestep during the simulation to ensure an average convective Courant number of less than 1. After 12 hours, the ambient temperature would be expected to swing back to the evening average. Natural convection flow (i.e., no wind) was assumed for the ambient temperature transients, and both a low heat load (10 kW) and high heat load (40 kW) case were run. The resulting transient response of the canister surface for both the baseline SNF and heater assembly model is shown in Figure 2-16. Overall, the plots show a minimal response from either a canister loaded with SNF or electrical heaters. Figure 2-17 shows a zoomed in plot of the average canister temperature for the 10 kW heat load, and it does show some differences in the thermal response between the two models, but this difference is small. Results showed that the thermal mass impact is within 2°C on the canister, meaning that within 12 hours, the maximum change in temperature at the canister surface is 2°C.

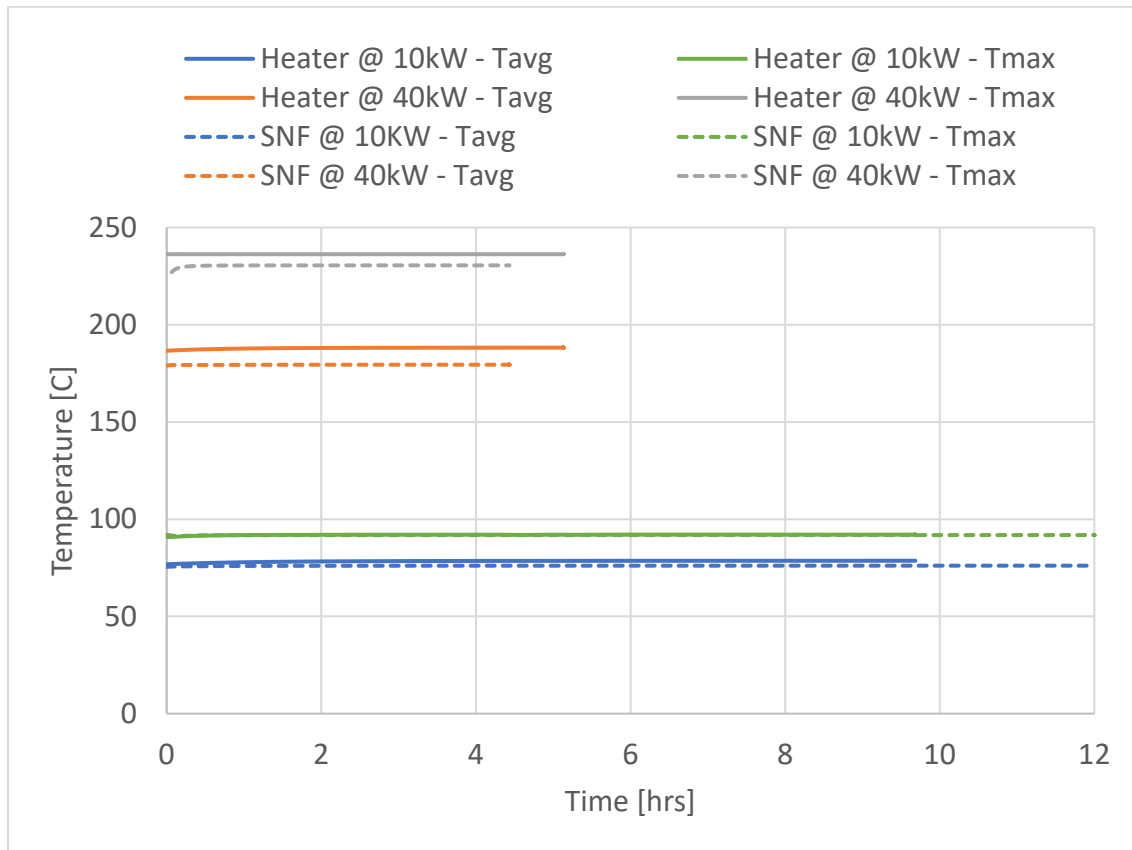


Figure 2-16. Canister Surface Temperature for Ambient Temperature Transients

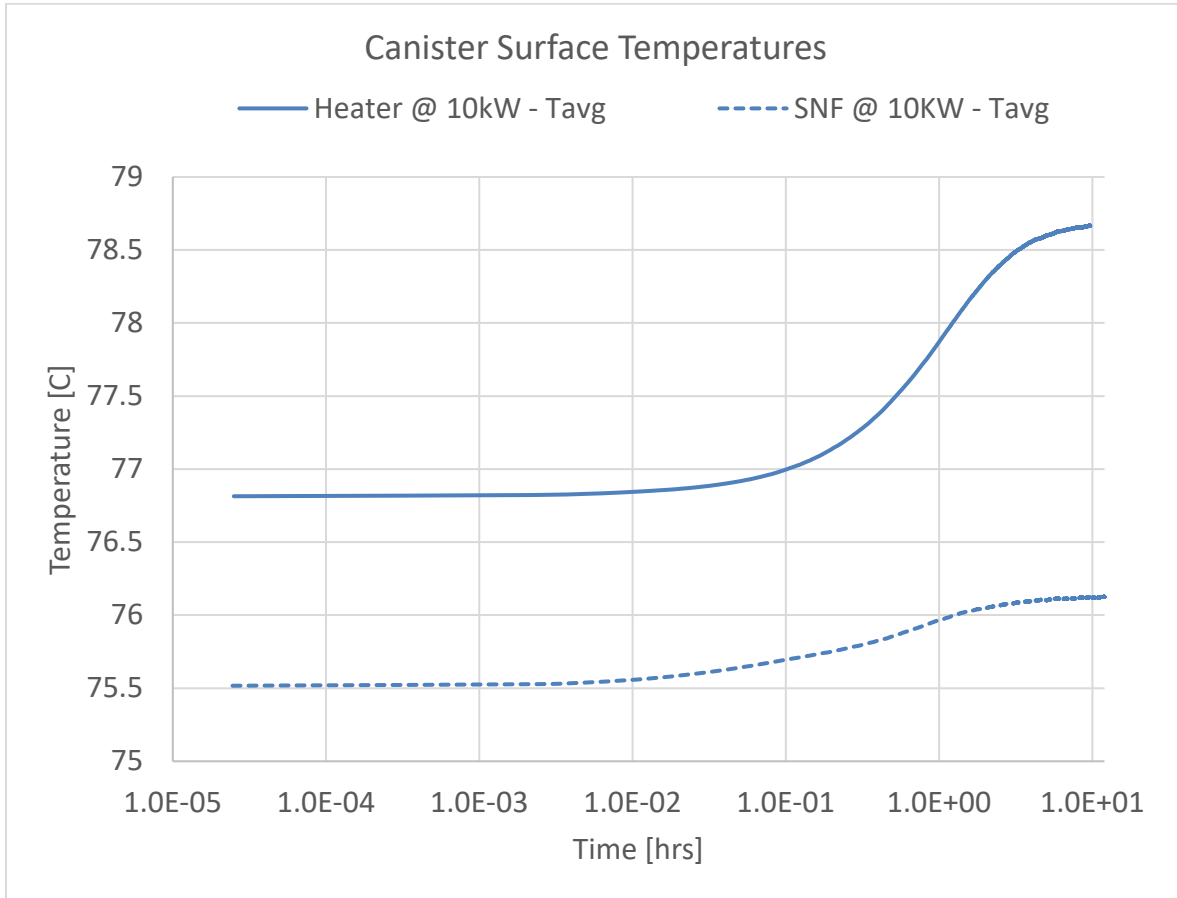


Figure 2-17. Average Canister Surface Temperature for Ambient Temperature Transients

Figure 2-18 shows the resulting maximum fuel or heater temperatures for the ambient temperature transients. Within 12 hours, neither model saw a significant change in the peak fuel or heater temperature. It is important to note that the baseline and heater assembly models have different peak values due to the differences between SNF and the electrical heaters.

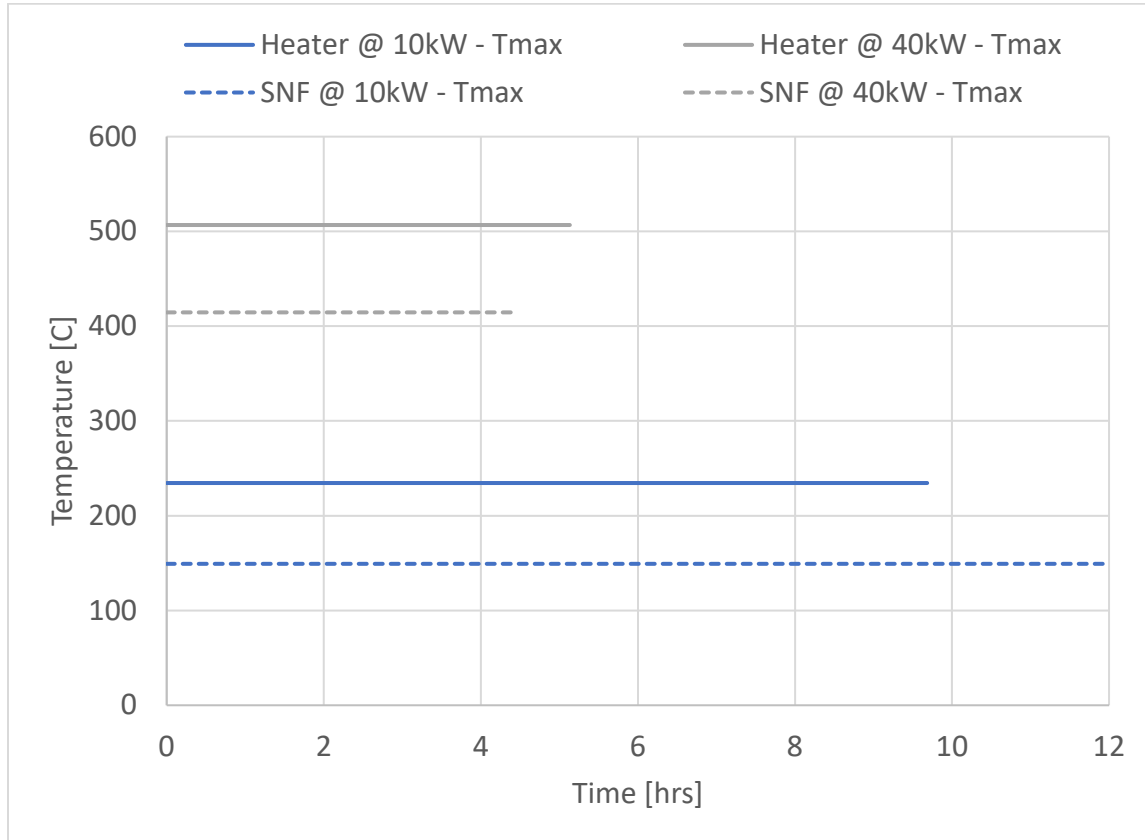


Figure 2-18. Peak Fuel or Heater Temperature for Ambient Temperature Transients

2.3.1 Wind Transients

Additional transients were run to look at the response of the system to changes in the average air flow through the module. As with the ambient transients, the models were initialized with a steady state simulation based on the evening conditions shown in Table 2-8 and natural convection air flow (no wind). For the transient, the ambient temperature and RH were held constant at the evening conditions shown in Table 2-8, but a 5 m/s wind was applied to the model. Only the low heat, 10 kW case was run for each model. Figure 2-19 shows the thermal transient response of the canister surface, and Figure 2-20 shows the resulting thermal response of the peak fuel or heater temperature. The wind transient did result in a slightly larger thermal response of the canister compared to the ambient temperature response, with the maximum thermal mass impact $\sim 4^{\circ}\text{C}$ on the canister for the wind case versus $\sim 2^{\circ}\text{C}$ for the ambient temperature case. It is important to note that the maximum 4°C change in the average canister surface temperature occurs with the heater assembly model, but the resulting difference in average canister surface temperatures between the SNF and heater assembly models at the end of the wind transient is $\sim 2^{\circ}\text{C}$, resulting in a minimal temperature difference between the two systems. There is no significant change to the SNF or heaters within 12 hours. The modeling results indicate that there is no significant difference in the thermal response of the system with electrical heaters compared to a system loaded with SNF. Based on the thermal transient results, there is no need to try to account for any canister mass differences with the control system for the electrical heaters for the CFD project.

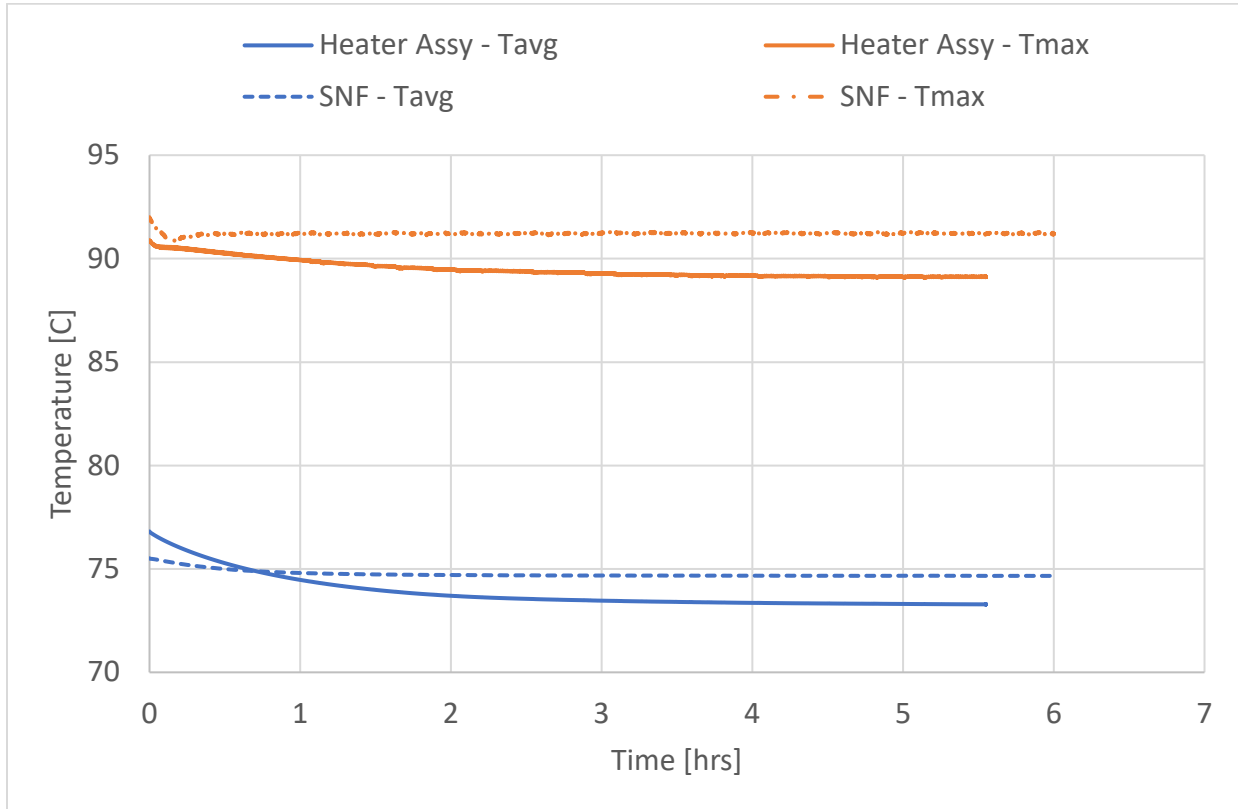


Figure 2-19. Canister Surface Temperature for Wind Transients at 10 kW

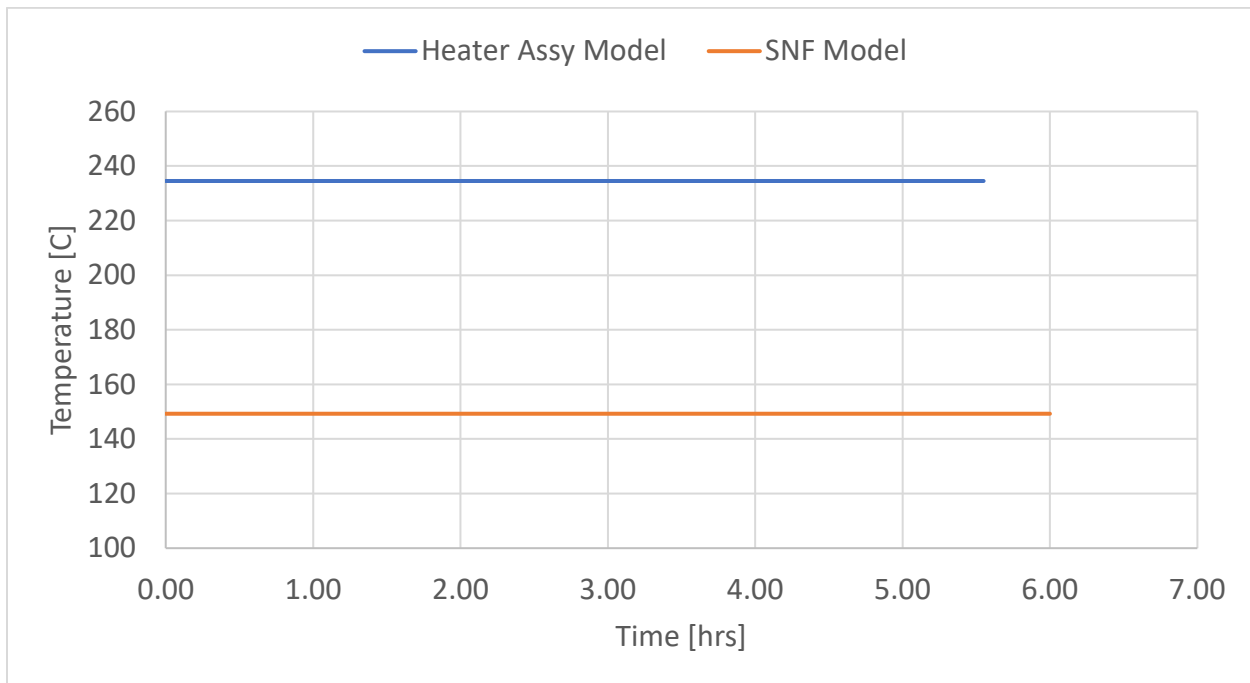


Figure 2-20. Peak Fuel or Heater Temperature for Wind Transients at 10 kW

2.4 Canister Model with Prototypic Heaters

SNL conducted preliminary heater tests within a 32PTH2 canister to verify the proposed heater design (Fascitelli et al. 2022 and Fascitelli and Durbin 2023). The testing consisted of a 32PTH2 DSC, with no AHSM-HS overpack, sitting on insulated blocks in an open room. A STAR-CCM+ model of the preliminary heater test system was previously developed (Suffield 2022) to simulate the experimental setup and conditions.

2.4.1 Experimental Setup

Various heat loads were applied uniformly to twelve prototypic heater assemblies. Four of the heater assemblies were located within the centermost basket positions, and the remaining eight heaters were distributed near the corners of the basket. Figure 2-21 shows the basket cells that the heaters were located within (Fascitelli and Durbin 2023). Details of the preliminary testing are given in Fascitelli and Durbin (2023).

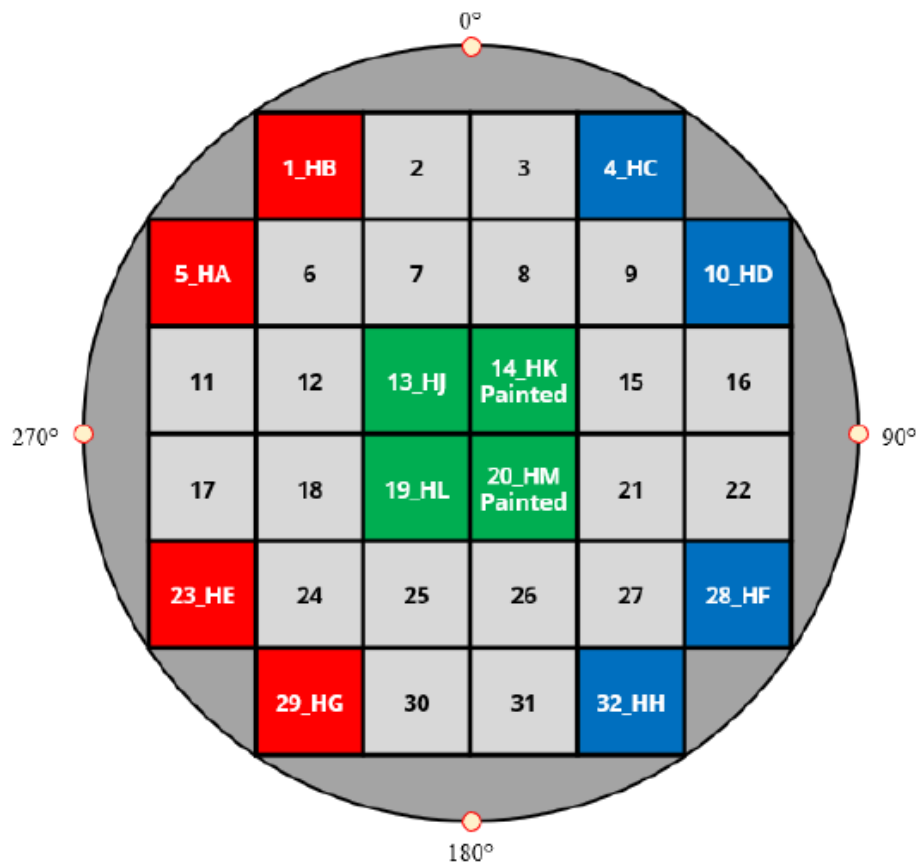


Figure 2-21. Cross-Sectional Plot of Heater Locations from Fascitelli and Durbin (2023)

2.4.2 Model Description

Testing conditions at SNL were applied to the canister-only model with prototypic heaters. Cases were run to simulate the 9.6 kW and 35 kW heat load test conditions. Temperatures predicted by the model were compared with thermocouple (TC) measurements recorded during testing. An uncertainty analysis was run with the canister-only model to determine the uncertainty in the temperature predictions and provide a range over which the predicted temperatures are expected to vary.

2.4.3 Uncertainty Analysis

Uncertainty analysis was run using the software Dakota (Dakota 2021). Dakota was developed by SNL with a variety of capabilities, including uncertainty quantification and parametric analyses. Dakota can use statistical methods to generate input parameters that are then used in an analysis software. In this case a sampling based uncertainty analysis method was used with STAR-CCM+ to run a large number of simulations after which statistical analysis of the results is performed by Dakota or another software package. Number of simulations is an engineering decision based off of the variation of input parameters and the sensitivity of the model to those parameters.

A Latin hypercube sampling uncertainty quantification (LHS UQ) method was used to run the uncertainty analysis and generate 95-95 confidence intervals. That is the range in which 95% of the results are expected to fall with 95% confidence. The equations for calculating the lower and upper 95-95 intervals are:

$$\text{lower} = 2\sigma_{95CI_lower} + (\text{overall}_{\text{mean}} - \text{lower}_{95CI_{\text{mean}}}) \quad \text{Eq. 2-1}$$

$$\text{upper} = 2\sigma_{95CI_upper} + (\text{upper}_{95CI_{\text{mean}}} - \text{overall}_{\text{mean}}) \quad \text{Eq. 2-2}$$

The perturbation parameters used for the LHS analysis and are listed in Table 2-9. The parameters were assumed to have a uniform distribution with the minimum and maximum values listed in Table 2-9. Using these parameters, 30 samples are analyzed to determine input uncertainty as represented by 95-95 confidence intervals.

Table 2-9. Perturbation Parameters

Parameter	Min	Max	Units
Heater emissivity (incoloy)	0.55	0.7	
Ambient Temp	-3.0	+3.0	K
Heater Power	-0.5	+0.5	%
Other Component emissivity	-5	+5	%
Canister – Basket Rail Gap	0.144	0.274	in.
Canister Ovality	0	50	%

Based on previous uncertainty analyses with SNF storage systems (Richmond 2022), and engineering judgement these parameters are expected to be the most important to this sensitivity case. The minimum and maximum parameter values are chosen to reflect experimental measurement error and uncertainty. Some of these parameters are difficult to measure and have limited data available. Others are easy to measure and have well-defined uncertainties from the measurement device.

The first parameter to be investigated is heater surface emissivity, which will have a significant impact on maximum heater temperature. Having an accurate model of the maximum heater temperature is important to determine whether the heaters are going to exceed the maximum temperature limit of the heater assemblies, especially at higher heat loads. At the time of this analysis, measured values for heater emissivity (incoloy) are not available. The lower measured heater rod emissivity would be expected to increase the peak temperatures for the heater, though it important to note that the measured value was taken from a new, never used heater assembly, from the latest heater design. The prototypic heaters are pre-oxidized, so a range of emissivity representing moderate oxidation was used. A moderately oxidized

heater emissivity ranges from 0.55 to 0.7 was used (Shurtz 2018). At the time, this range covered the expected emissivity values of the heater cladding. SNL plans to take future measurements on the used prototypic heater rods after testing.

Ambient temperature, heater power, and other component emissivities can be measured with varying degrees of difficulty. Ambient temperature and heater power are easily measured. The devices used to measure ambient temperature, heater power, and emissivity have published accuracies. These parameters are set to the measured value plus/minus the published accuracy of the measurement device.

The canister–basket rail gap is of particular importance to this task because it has a significant impact on both canister surface and heater temperatures. In addition, measuring the canister–basket rail gap can be quite difficult, especially at higher heat loads. because of access considerations measurements near the top of the canister are easier to obtain than near the bottom. This means that the gap across the axial length of the canister is not well characterized. SNL provided measurement data for the gap near the lid at ambient temperature and various heat loads, with a maximum heat load of 35 kW (Fascitelli 2023). From the SNL measurements, there appears to be some ovality in the canister shell that is impacting the canister–basket rail gap profile. It is assumed that the canister shell is out of round at the mouth of the canister where the lid attaches and becomes rounder toward the base. The thick base of the canister provides support to maintain the roundness of the canister.

For this sensitivity study, the canister–basket rail gap range is set to the minimum and maximum measured gap at the 12 o’clock position on the canister–basket rail. The ovality of the canister is set to 0% to 50%. 100% ovality is where both the top and bottom inner surface of the canister are touching the outer surface of the basket rail. 50% ovality represents a 50% reduction in gap at the 12 o’clock position due to the ovality of the canister. Figure 2-22 illustrates the difference between 0% ovality and 100% ovality.

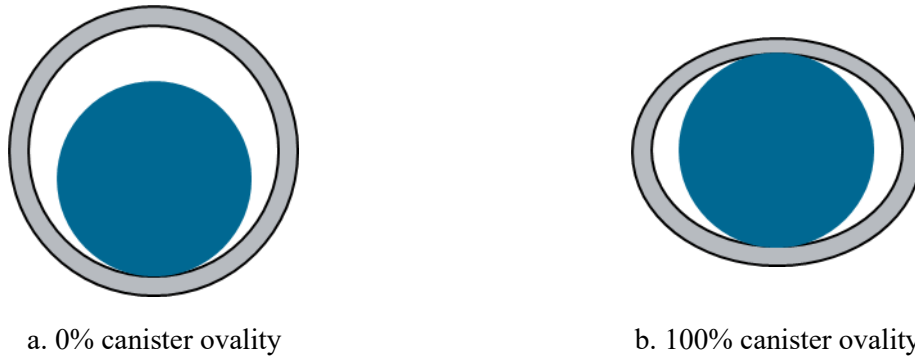


Figure 2-22. Diagram showing the extremes in canister – basket rail gap ovality (not to scale)

The following equations are used to calculate the gap between the inner surface of the canister shell and outer surface of the basket rails used for the contact resistance applied in STAR-CCM+. These equations are meant to represent the impact of the canister’s ovality on the performance of the canister. The actual geometry of the canister is not changing in the model. Since the basket rail and canister shell are circles sitting inside of each other, there is circular eccentricity. The gap between two eccentric circles as a function of angular position is (Li 2021):

$$\delta(\theta) = h - e_c \cos(\theta) \tag{Eq. 2-3}$$

where h is the gap between eccentric circles, and e_c is the eccentricity of the circles. For a circle within an

ellipse, the following equations can be applied:

$$h = \frac{b}{\sqrt{1 - (e_e \cos(\theta))^2}} \quad \text{Eq. 2-4}$$

$$b = can_{ID} - gap_{max} \cdot can_ovality/2 \quad \text{Eq. 2-5}$$

$$a = 2can_{ID} - b \quad \text{Eq. 2-6}$$

$$e_e = \sqrt{1 - \left(\frac{b}{a}\right)^2} \quad \text{Eq. 2-7}$$

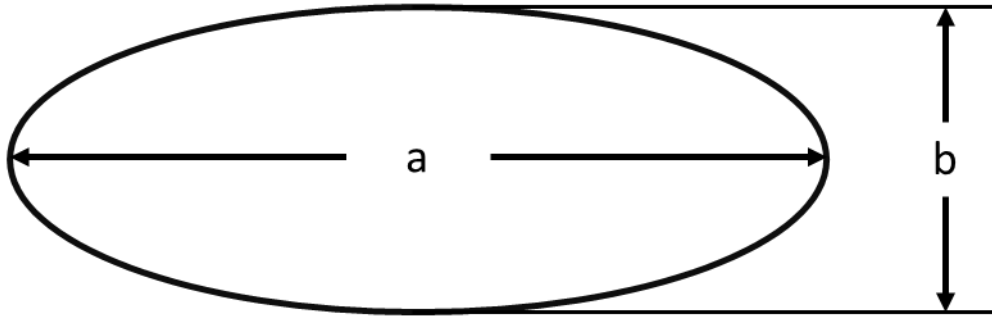


Figure 2-23. Illustration of a and b, the Major and Minor Diameters of the Ellipse

A and b are the major and minor diameters of the ellipse. Can ovality is the amount of ovality that exists (from 0 to 1.0), and gap_{max} is the amount of gap that exists when the canister is perfectly round. Finally, e_e is the eccentricity of the ellipse, not to be confused with the circular eccentricity. When adjusting the amount of ovality in the canister, it is assumed that the canister maintains a constant perimeter. The minor diameter b is adjusted in relation to the gap between the canister and the basket rail. So, 50% ovality would be 50% reduction in gap at the 12 o'clock position. Then, major diameter a is calculated to preserve the perimeter of the canister.

2.4.4 Comparisons with Measured TC Data

The uncertainty quantification results for the STAR-CCM+ canister model with prototypic heaters are compared with measured TC data in Figure 2-24 and Figure 2-25. Measurement results were provided by SNL. The TCs are labeled by the angular location and axial position on the canister surface, with zero degrees corresponding to the top of the canister (12 o'clock) and the axial length is measured from the bottom of the canister. The dot in the center of the error bar is the mean value from the uncertainty analysis. For both of these heat loads, the CFD model matches the SNL test canister fairly well. The 35 kW case has a visibly better agreement with the SNL test canister. One possible cause for this difference is the approximation of natural convection at the surface of the canister in the CFD model. The test canister is inside a warehouse sitting on wooden blocks close to the ground. The wood blocks are

represented in the model, but the ground is not. Future work will include modeling with an updated heater design and all 32 heater cells filled with heaters to simulate future testing planned by SNL. It should be noted that the peak canister temperatures occur at the bottom of the canister (180°) for the canister only test and model, but for the models with the canister sitting in the overpack the peaks occurred at the top of the canister (0°) as shown in Figure 2-10 and Figure 2-11. The difference in peak temperatures at the bottom (180°) and top (0°) locations in the overpack model is relatively small, within 8°C for the 40 kW case, compared to the canister only model where the bottom of the canister temperatures were as large as 40°C for the 35 kW case. This difference is likely due to differences in convective flow along the bottom of the canister. When the canister is sitting within the overpack on the rail assembly it is subject to more convective flows than when sitting on the wooden blocks near the ground in the canister only test.

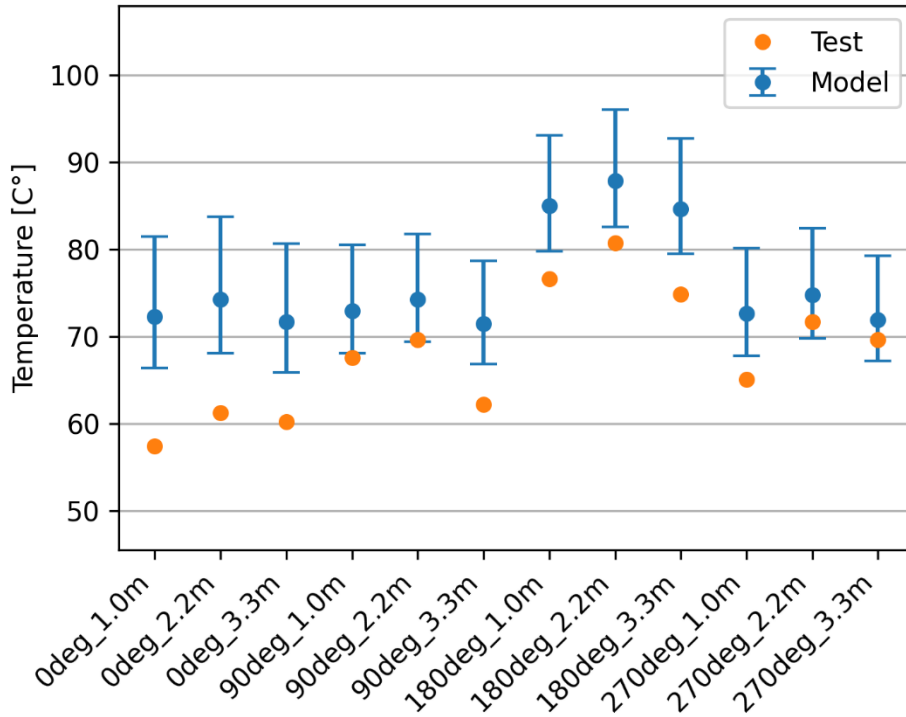


Figure 2-24. Canister Temperatures at 9.6 kW Heat Load

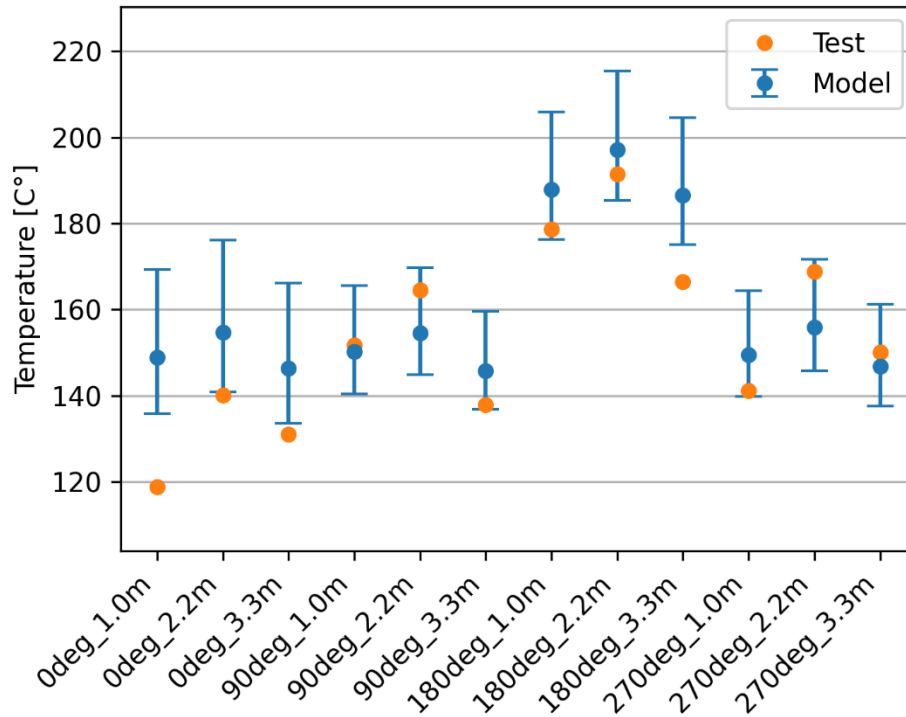


Figure 2-25. Canister Temperatures at 35 kW Heat Load

Figure 2-26 and Figure 2-27 show the comparison in heater temperatures between the model and test canister at 9.6 kW and 35 kW heat load. At the 9.6 kW heat load, most of the temperatures from the CFD model are close to the SNL test canister. The heaters located at the top of the canister (cells 1, 4, 5, and 10) are within the error bars from the uncertainty analysis. The rest of the test heater temperatures, located in the center and bottom of the canister, are slightly outside the model error bars. Despite this, the model matches the trends of the test canister. TCs 28HF_1.0m to 28HF_3.3m represent the heater in cell 28 at 1.0 m, 2.2 m, and 3.3 m, axial position as measured from the bottom of the canister. Looking at these three axial measurements, the temperature of the middle TC located 2.2 meters from the bottom of the canister is warmer than the other two located near the ends at 1.0 meter and 3.3 meters. Although the model does not match the test data perfectly, the model captures the trends of these temperature measurements from the model. Overall, the model compares well with the test data outside one outlier for the 9.6 kW heat load. It is important to note that the outlier data point reported a much lower temperature than the other TC measurements and it is not know why this TC would be reporting a significantly lower temperature.

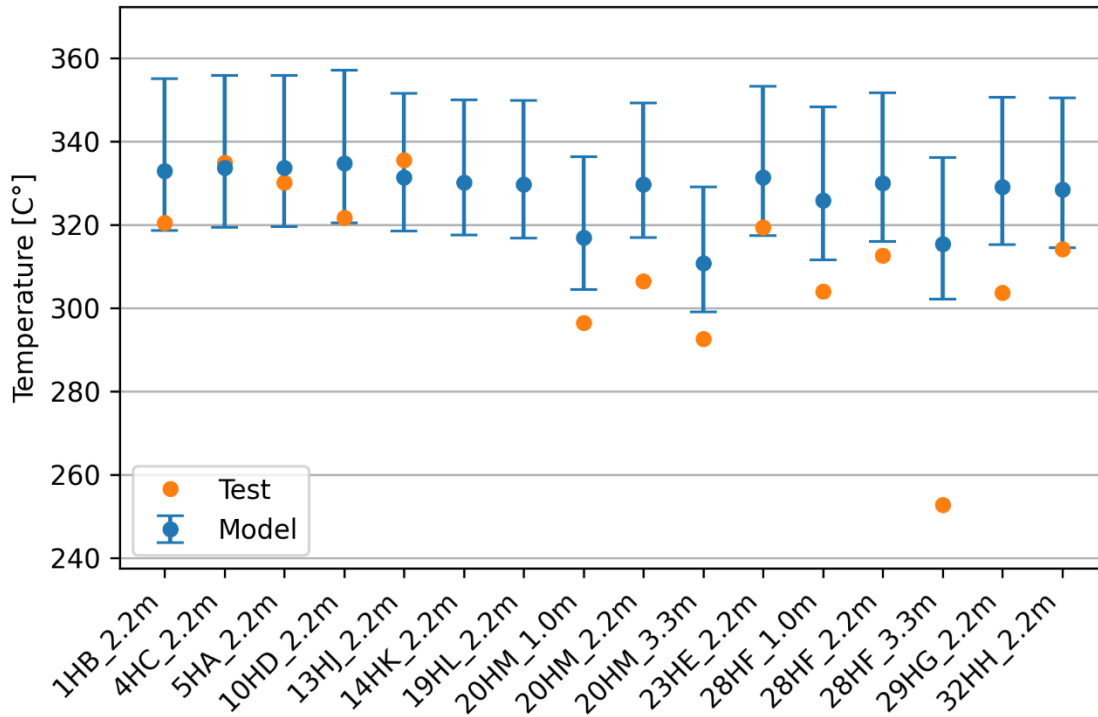


Figure 2-26. Heater temperature with 9.6 kW heat load

Figure 2-27 compares the heater thermocouple temperature for the 35kW heat load and the results of the uncertainty analysis. For the 35 kW heat load, the model and test temperature deviate a bit more from the previous lower heat load of 9.6 kW. The model results show the same trends as the test measurements.

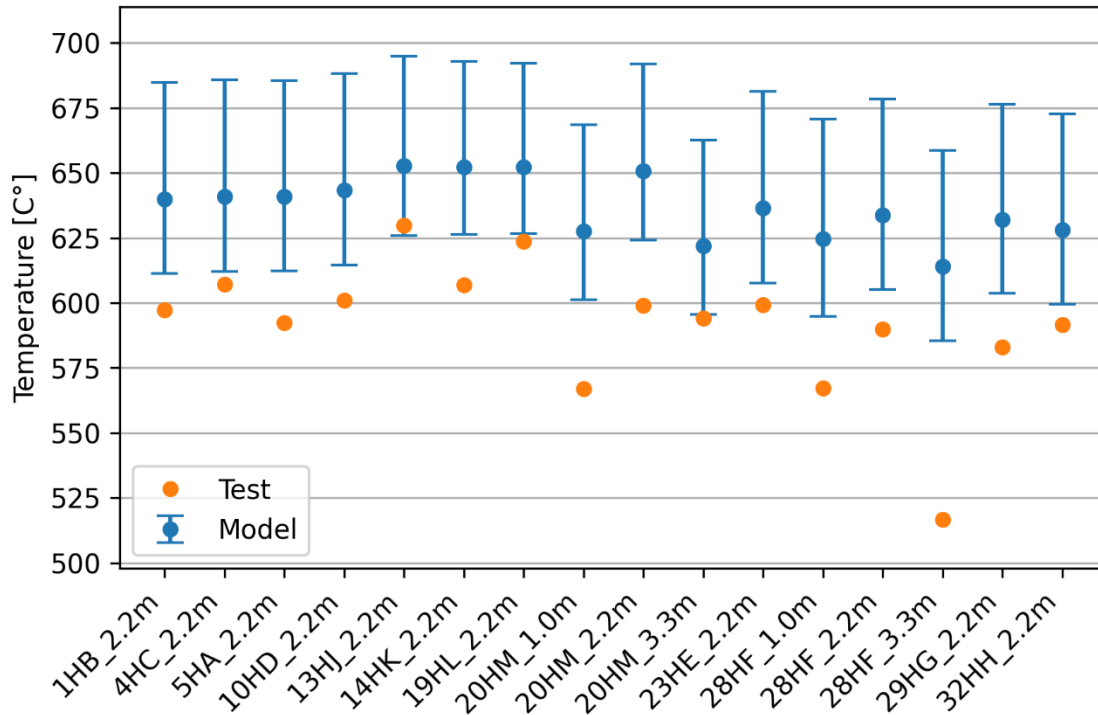


Figure 2-27. Heater Temperature with 35 kW Heat Load

Figure 2-28 compares the maximum heater and maximum canister surface thermocouple temperatures between the STAR-CCM+ canister-only model and the SNL test canister. The plots show all of the heat loads tested. Over the different heat loads tested, the model and test show good agreement with each other. The uncertainty analysis was only performed on the 9.6 kW and 35 kW heat loads, so confidence intervals are omitted from this figure. For the maximum heater temperatures, both the model and test match very well at the lower heat load. As the heat load increases, there is a slight deviation. For the maximum canister surface temperatures, the lower and higher heat loads match very well between the model and the test. Overall, the maximum heater and maximum canister surface temperatures show good agreement between the experimental test and model.

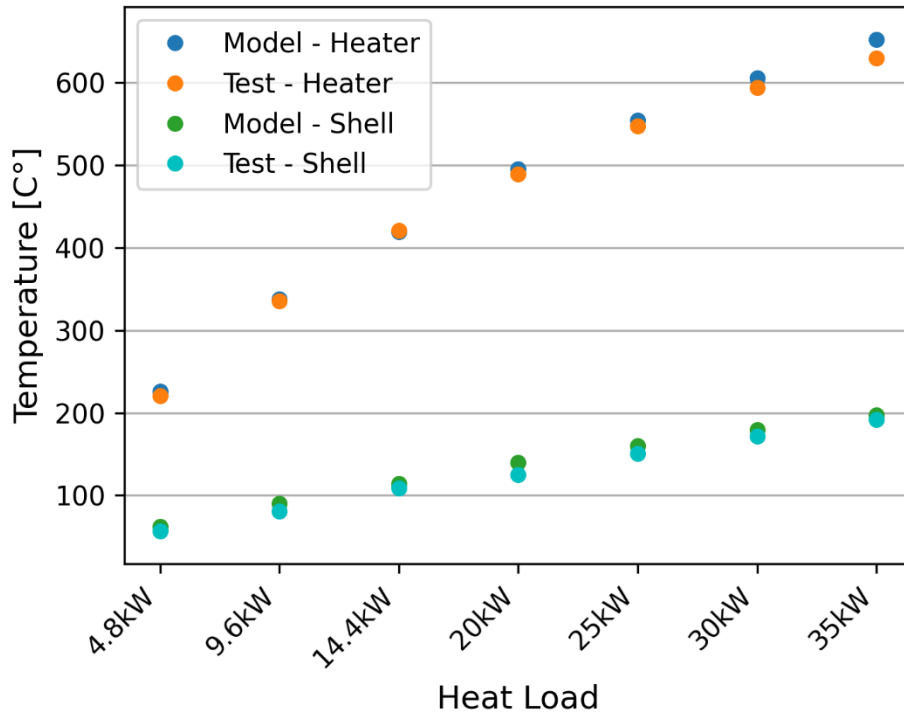


Figure 2-28. Comparison of Maximum Heater and Canister Surface Temperatures between Test and Model.

3. LINKAGE BETWEEN THERMAL AND DEPOSITION MODELS

The PNNL STAR-CCM+ particle deposition models are built from the PNNL STAR-CCM+ thermal models. PNNL has extensive experience developing thermal models for storage and transportation canisters of SNF. Previous PNNL STAR-CCM+ thermal models have been through validation exercises, such as the High Burnup Spent Fuel Data Project (Fort et al. 2019) and Dry Cask Simulator (Suffield et al. 2019 and Suffield et al. 2020). These validation exercises have provided validation and confidence in the PNNL thermal models.

The PNNL thermal models are well suited for looking at particle deposition since the flow and temperature profiles have already been set up and solved. Particle deposition is incorporated by adding particle tracking sub-models to the physics of the thermal model, creating particle injectors at the inlets, and iterating the solution with particle tracking on. While the PNNL thermal models are well developed, the deposition models are preliminary and will require further development. The CDFD project will help validate the deposition models.

The CDFD project will use a no heat canister as a control. It is key to limit the thermal loadings in the no heat module to limit natural convection. This will allow deposition in the no heat canister to be mainly driven by wind effects. Eliminating backflow through the outlets ensures that the wind driven flow impacting canister deposition is entering through the inlets only. This highlights the interplay between the thermal and deposition models.

This page is intentionally left blank.

4. DEPOSITION MODELING

This section describes preliminary particle tracking and deposition models, which were developed to predict the deposition of particulates on SNF canisters. The modeling results shown are preliminary and for information only. The models are useful for understanding the physics of particle tracking and deposition as it applies to SNF canisters. However, they are not the final analysis of the systems discussed, and additional model development and testing will be needed before models such as these can be useful for determining the likelihood of CISCC on SNF canisters.

4.1 Background on Previous Work

During dry storage, the primary canister degradation process is likely to be CISCC at the heat-affected zones of the canister welds (NRC 2012). While it is currently unknown if there is a threshold concentration for CISCC initiation, one can assume that the onset and progress of material degradation will depend on local particulate concentration, the properties of the particulate species, and synergistic effects when multiple particulates are present. The primary particulate of concern is chloride, which is dispersed in the atmosphere and then deposits onto the canisters. Currently, the rate of chloride deposition onto the canisters is unknown. Modeling is being developed that will aid in filling this knowledge gap.

Initial PNNL deposition modeling work focused on investigating the feasibility of modeling and identifying key phenomena to include in the models. This work is documented in *Preliminary Deposition Modeling: For Determining the Deposition of Corrosive Contaminates on SNF Canisters* (Jensen et al. 2020a). Follow-on work and model development is presented in *Status Update: Deposition Modeling for SNF Canister CISCC* (Jensen et al. 2020b). Initial deposition models were developed for the AHSM-HS 32PTH2 module and are described in Suffield et al. (2021 and 2022).

4.2 Deposition Comparisons with Baseline Model

Deposition cases were run with the updated AHSM-HS 32PTH2 baseline model with SNF and the heater assembly model described in Section 2. A multicomponent liquid representing an SSA particle made up of water and NaCl was injected at the inlets of the storage module. A uniform particle size distribution ranging from 0.25 to 25 μm in diameter was assumed for the injected particles at the inlets. The initial droplet composition assumed a solid mass fraction of 3.5% based on the salinity of ocean water (Zakowski 2014).

Steady state simulations were run using both the SNF baseline and heater assembly models. The simulations assumed an ambient temperature of 63.4°F (17.4°C) and RH of 66.9%. Deposition was evaluated by calculating the deposition efficiency for each steady state run. The deposition efficiency was calculated based on the solid particle mass since the liquid droplet mass will be changing as it moves through the heated overpack and evaporates. Deposition efficiency was calculated based on the following equation:

$$\text{Deposition Efficiency} = \frac{\text{Solid Particle Mass of Stuck Particles}}{\text{Total Solid Particle Mass of Particles Entering Overpack}} \quad \text{Eq. 4-1}$$

The model currently assumes a very simple “stuck” surface condition, where if the particle contacts the surface, it is indefinitely stuck to the surface. Both a low heat (10 kW) and high heat (40 kW) case was run with both the SNF and heater assembly model. Table 4-1 shows the resulting deposition efficiency of the canister and for all inner surfaces of the storage module (total deposition). The results show that the

predicted canister deposition is within 1.5% between the SNF and heater assembly model at both heat loads, and the total deposition is within 2%. Canister particle deposition plots are shown for the SNF baseline and heater assembly models in Figure 4-1 for the 40 kW case. Both models show more deposition along the top of the canister and there is noticeable particle “build up” along the very top of the canister, creating narrow lines of high deposition.

Table 4-1. Resulting Deposition Comparison for AHSM-HS 32PTH2 Models

Model	Heat Load [kW]	Canister Deposition Efficiency	Total Deposition Efficiency
SNF Baseline	10	10.9%	73.5%
Heater Assy Model	10	11.1%	72.6%
SNF Baseline	40	10.6%	73.5%
Heater Assy Model	40	9.4%	75.5%

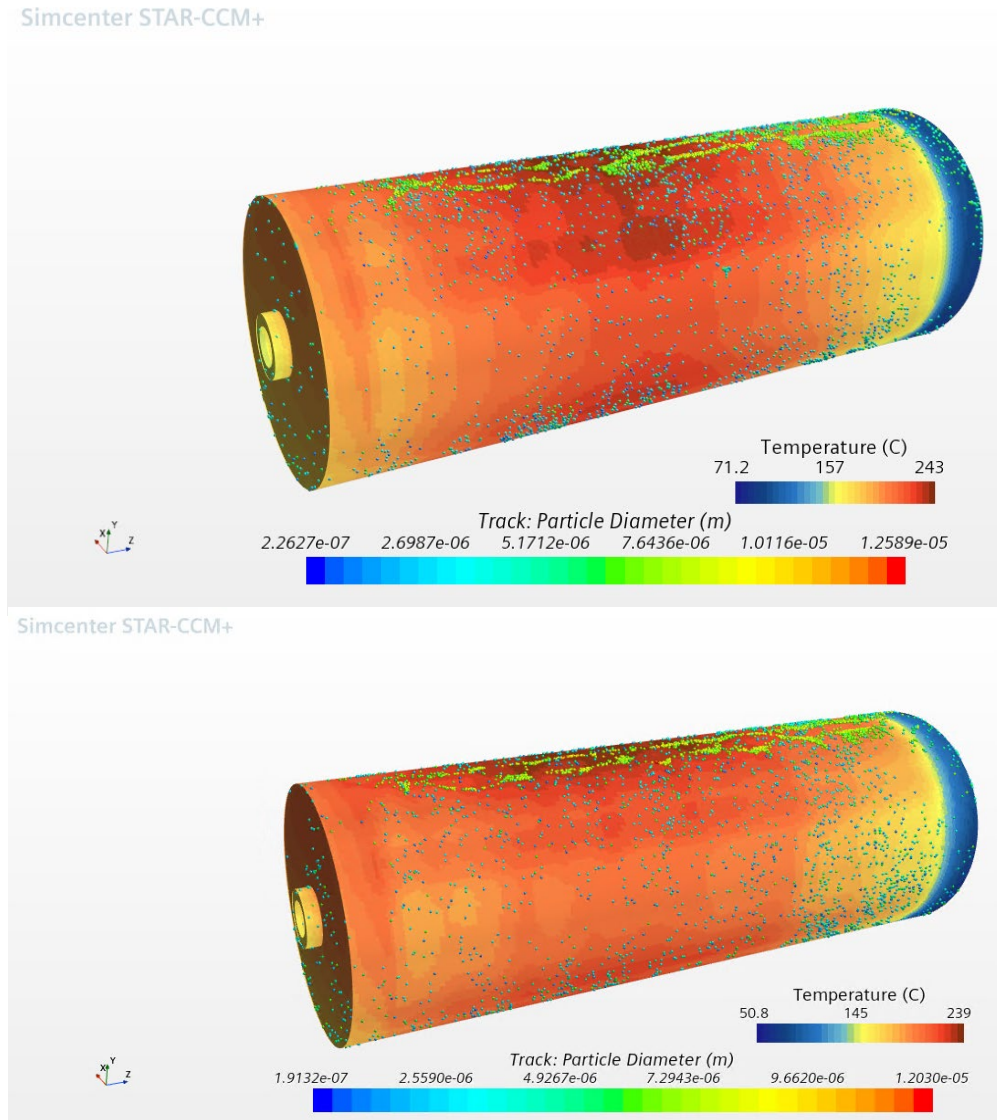


Figure 4-1. Canister Particle Deposition Contour Plots at the 40 kW Heat Load for (a) SNF Baseline Model and (b) Heater Assembly Model

The distribution of particle sizes that deposited on the canister are shown in Figure 4-2 and Figure 4-3 for the SNF and heater assembly models at both the 10 kW and 40 kW heat loads. Figure 4-2 and Figure 4-3 plot the fraction of deposited particles on the canister for different diameter ranges (e.g., a value of 4–5 on the x-axis and 0.15 on the y-axis represents that 15% of the particles deposited on the canister had a particle diameter size between 4 and 5 μm). The plots show a similar particle distribution between the SNF baseline and heater assembly models. For both models' particles sized from 5 to 6 μm had the highest frequency of deposition on the canister at the low heat load (Figure 4-2). At the high heat load for both models, most of the deposited particles ranged from 1 to 7 μm (Figure 4-3).

Figure 4-4 and Figure 4-5 plot the angular location distribution of particles on the canister for the SNF and heater assembly models at both the low and high heat loads. The top of the canister corresponds to the 0-degree location and bottom of the canister corresponds to the 180-degree location. Again, the plots show a similar particle distribution between the SNF baseline and heater assembly models. The low heat load plot shows that most of the deposition occurs near the top of the canister (Figure 4-4), and the high heat

load plot shows slightly more deposition along the bottom of the canister (Figure 4-5). Overall, the electrical heaters provide a canister surface temperature and deposition profile very similar to a canister loaded with SNF.

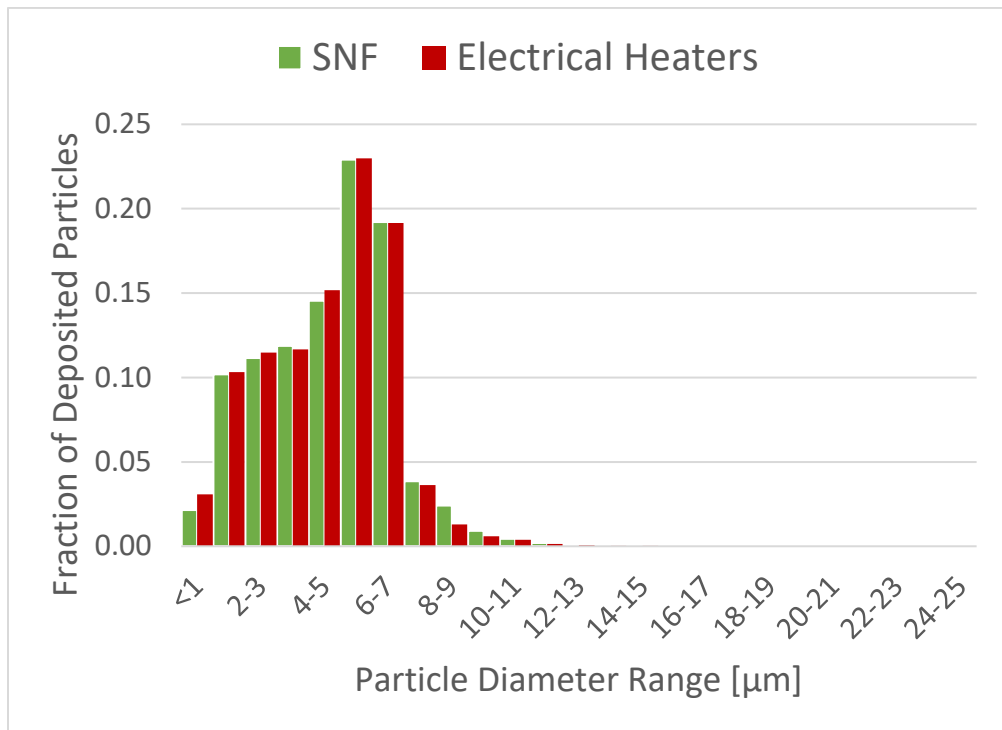


Figure 4-2. Particle Size Distribution on the Canister Surface at 10 kW

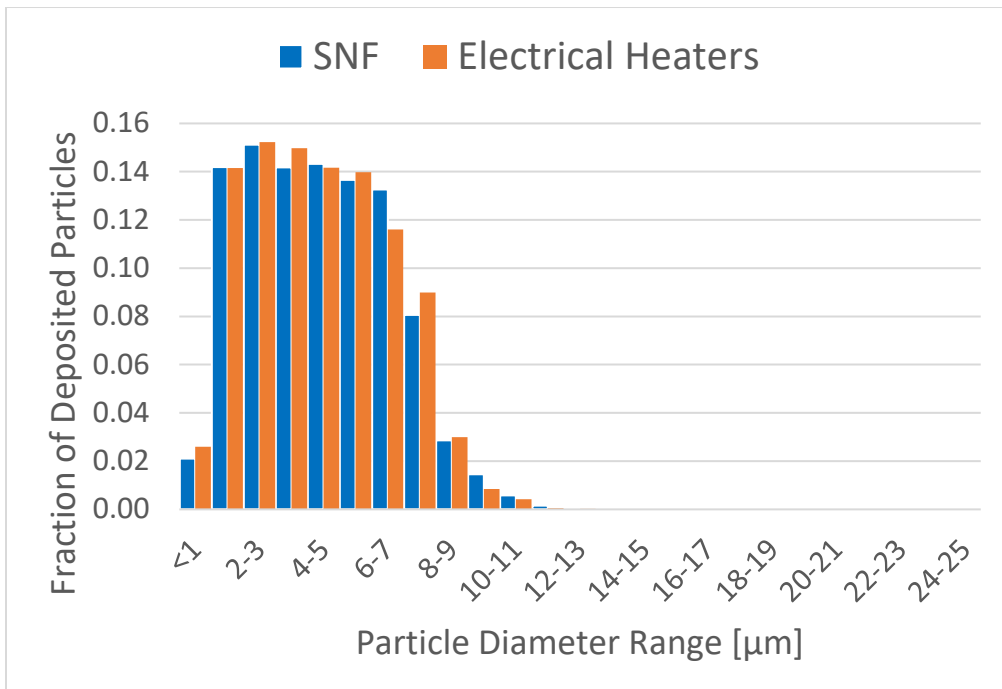


Figure 4-3. Particle Size Distribution on the Canister Surface at 40 kW

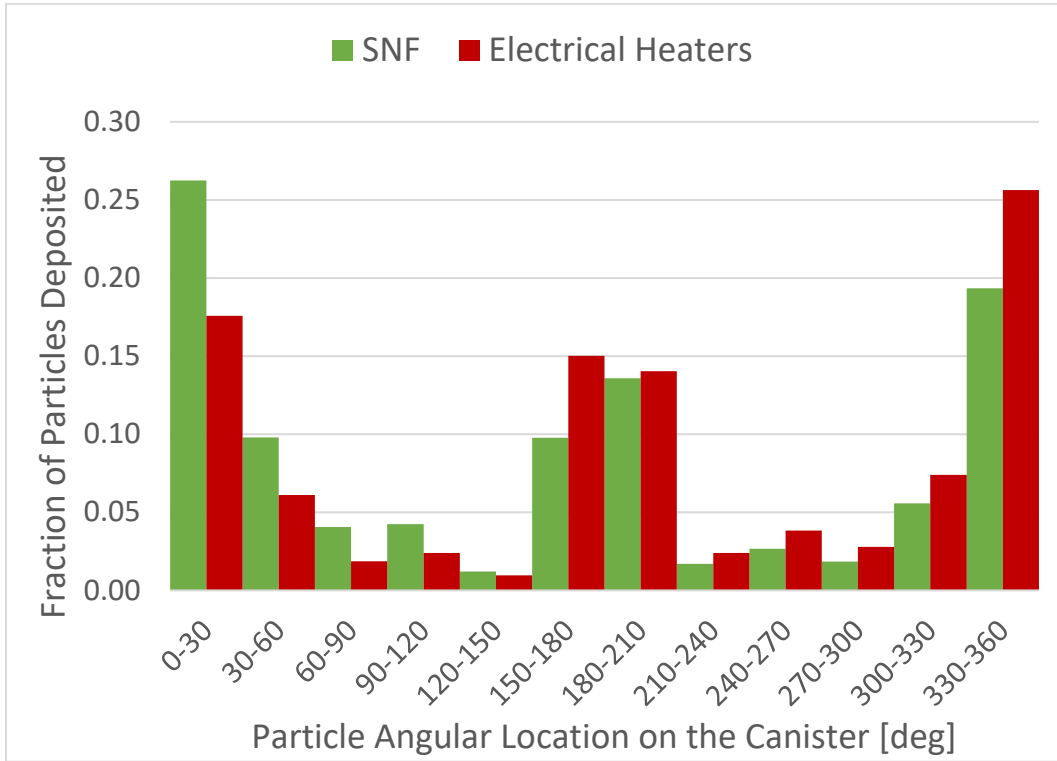


Figure 4-4. Angular Particle Location Distribution on the Canister Surface at 10 kW

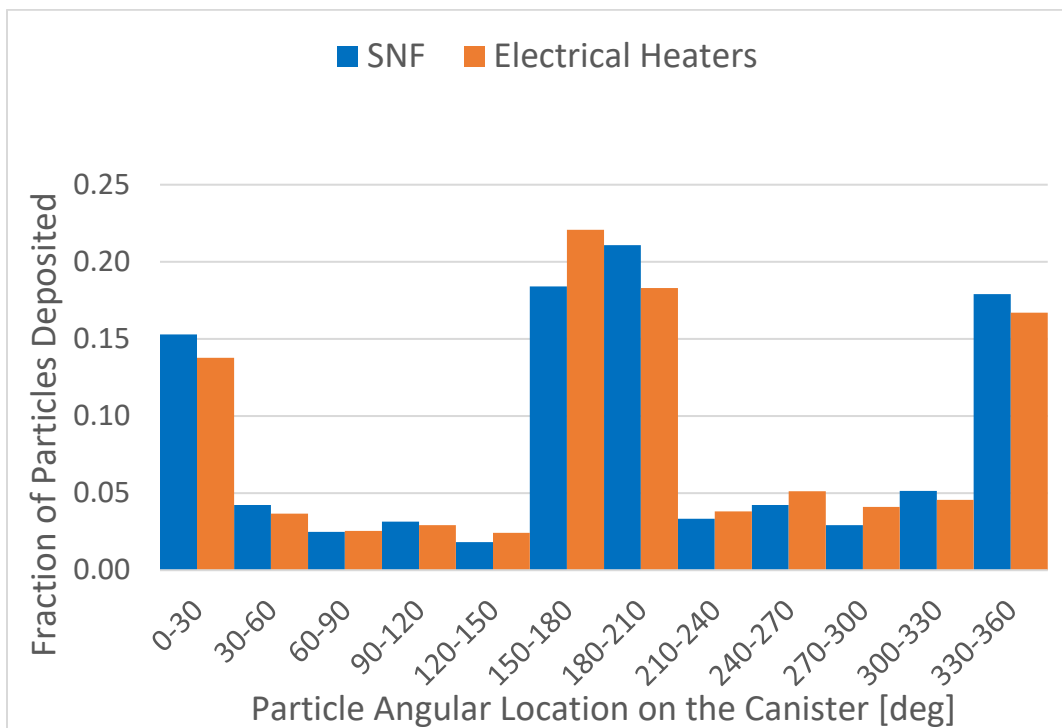


Figure 4-5. Angular Particle Location Distribution on the Canister Surface at 40 kW

4.3 Particle Distribution

The PNNL deposition model has historically assumed a uniform particle distribution, meaning an equal number of every size particle, ranging from 0.25 to 25 μm for particles entering the inlets. This particle size range and distribution is meant to be a placeholder in the model until a source term can be identified. In reality the particle distribution would not be expected to be uniform. Once a site has been identified, an ambient particle source term and distribution will be characterized. The updated particle size range and distribution for the CDFD site will provide the size distribution for particles entering the inlets of the AHSM-HS.

A sensitivity analysis was run to look at how the particle size distribution would impact canister deposition. The heater assembly model was run with a normal particle size distribution. The normal distribution assumed a mean particle diameter of 12 μm , standard deviation of 5 μm , minimum of 0.25 μm , and maximum of 25 μm . Table 4-2 compares the resulting canister deposition for the uniform and normal particle distributions. The canister deposition efficiency is within 0.5% between the two distributions. Future work will look at a log-normal distribution.

Figure 4-6 and Figure 4-7 compare the distribution of particle sizes that deposited on the canister for 10 kW and 40 kW heat loads, respectively. The normal particle size distribution results in a more normal canister particle deposition distribution. For both heat loads, the normal particle size distribution results in particles with a diameter from 3 to 4 μm , making up the largest fraction of deposition on the canister. Plots comparing the angular location distribution of particles on the canister are shown in Figure 4-8 for 10 kW and Figure 4-9 for 40 kW. The top of the canister corresponds to the 0-degree location. The resulting angular particle location distribution along the canister surface is very similar between the two different particle size distributions. Overall, the normal particle size distribution provided results like the uniform distribution. Since a normal distribution is expected to be a more realistic distribution, it will be used going forward with the AHSM-HS deposition models until an ambient site source term has been determined.

Table 4-2. Resulting Deposition Comparison for AHSM-HS 32PTH2 Models

Particle Size Distribution	Heat Load [kW]	Canister Deposition Efficiency
Uniform	10	11.1%
Normal	10	10.7%
Uniform	40	9.4%
Normal	40	9.2%

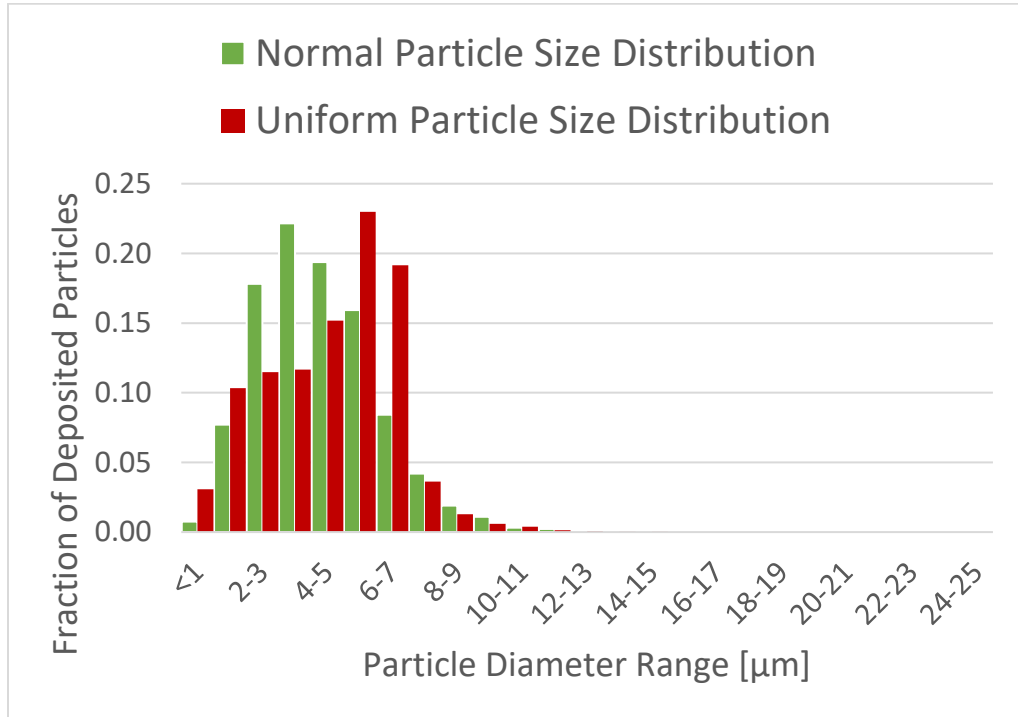


Figure 4-6. Particle Size Distribution on the Canister Surface at 10 kW for Particle Distribution Sensitivity

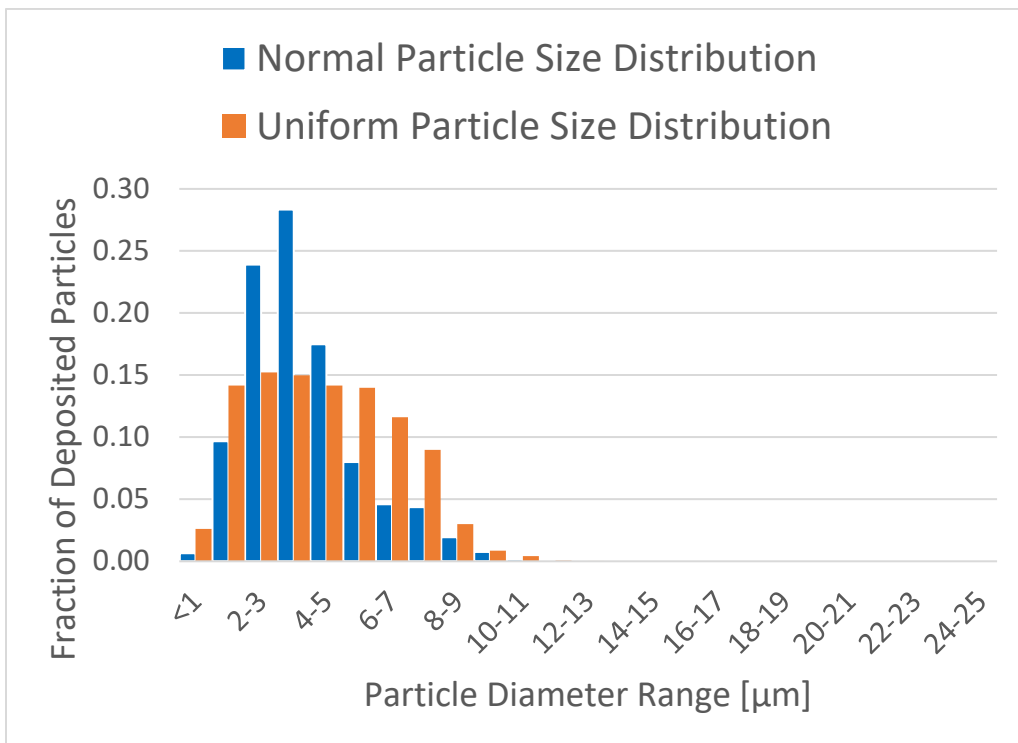


Figure 4-7. Particle Size Distribution on the Canister Surface at 40 kW for Particle Distribution Sensitivity

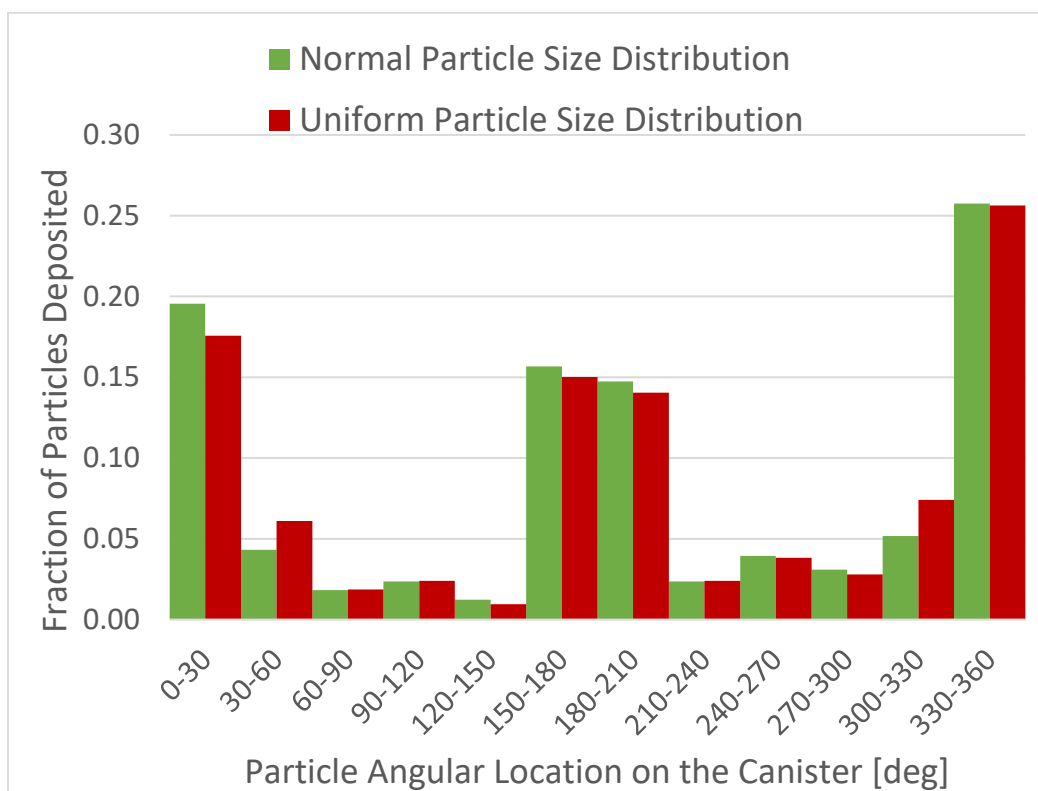


Figure 4-8. Angular Particle Location Distribution on the Canister Surface at 10 kW for Particle Distribution Sensitivity

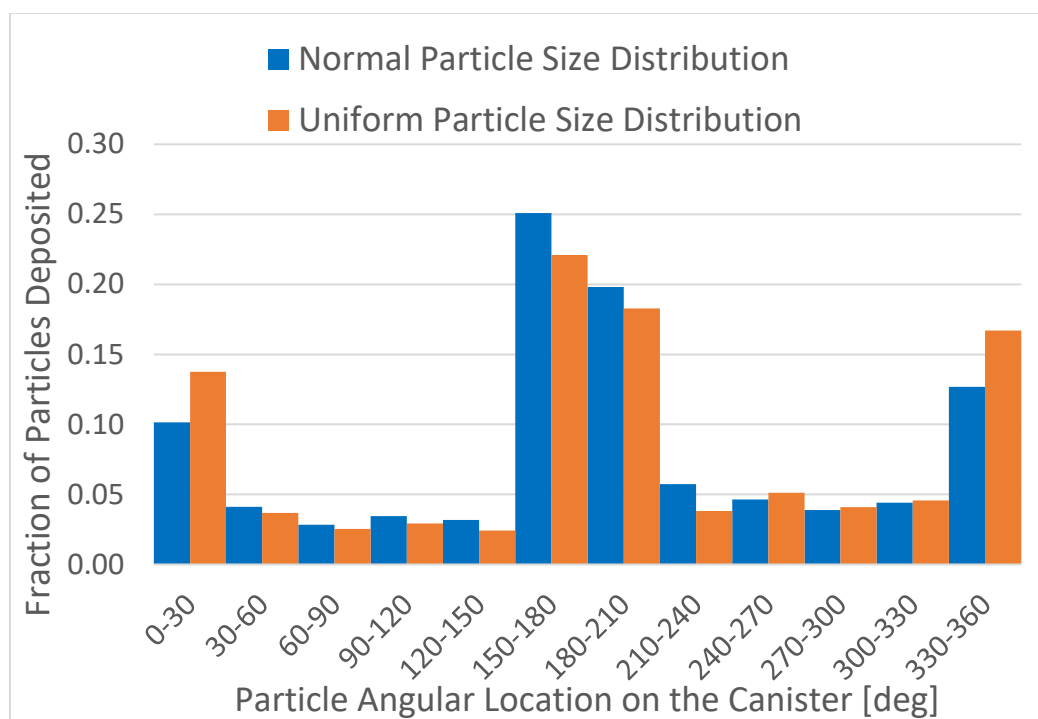


Figure 4-9. Angular Particle Location Distribution on the Canister Surface at 40 kW for Particle Distribution Sensitivity

4.4 Three AHSM-HS Deposition Model

Steady state simulations were also run with the updated three AHSM-HS 32PTH2 heater assembly model described in Section 2. The model was run assuming an ambient temperature of 63.4°F (17.4°C) and RH of 66.9% based on the estimated average ambient conditions for a coastal site. The normal particle size distribution described in Section 4.3 was applied to inject particles at the inlets of the modules. The normal distribution assumed a mean particle diameter of 12 μm, standard deviation of 5 μm, minimum of 0.25 μm, and maximum of 25 μm. The particles assumed a multicomponent liquid representing an SSA particle made up of water and NaCl. The initial droplet composition assumed a solid mass fraction of 3.5% for NaCl. The steady state simulations assumed natural convection flow through the storage modules. Canister deposition is plotted in Figure 4-10 for the three-module model, and the total deposition within the storage module is shown in Figure 4-11.

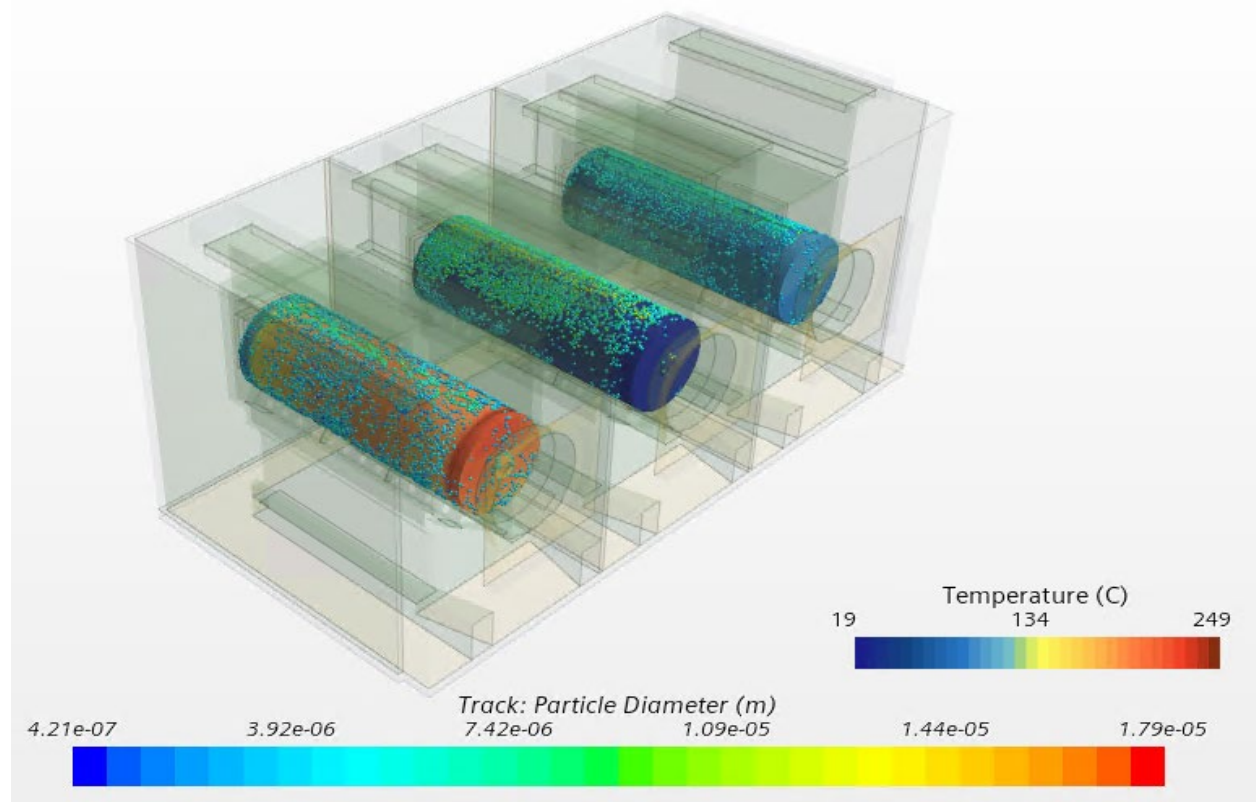


Figure 4-10. Canister Deposition for Three AHSM-HS 32PTH2 Heater Assembly Model

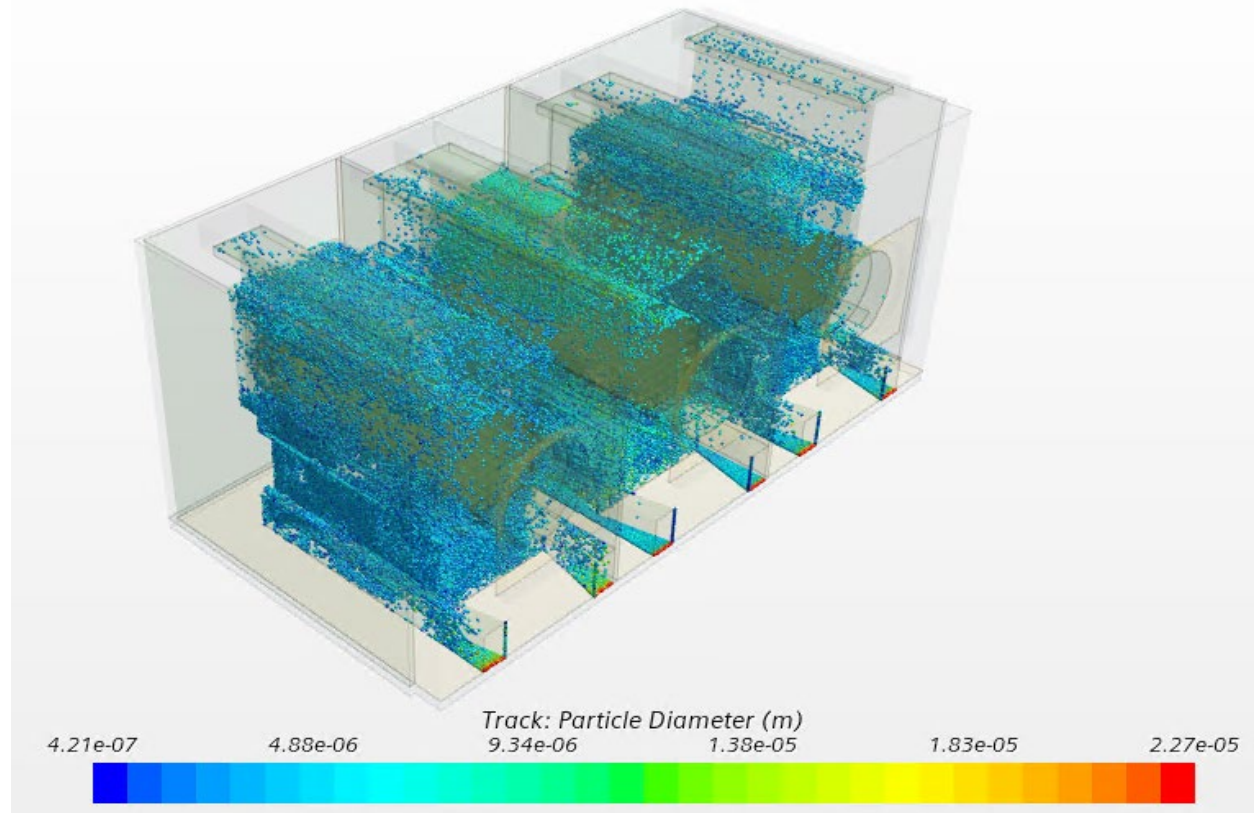


Figure 4-11. Total Deposition for Three AHSM-HS 32PTH2 Heater Assembly Model

4.4.1 Comparisons with Stand-Alone AHSM-HS Models

The three AHSM-HS 32PTH2 heater assembly model was run and compared with the stand-alone AHSM-HS 32PTH2 heater assembly model at the corresponding heat load configuration (i.e., no heat load, low heat load, and high heat load). For the no heat load stand-alone model, solar loadings are the significant thermal loads that are driving the natural convection flow. Previous thermal modeling of the three AHSM-HS 32PTH2 heater assembly model showed that with insulation placed between AHSM-HS assemblies there is minimal heat transfer between modules (Suffield et al. 2021 and Suffield et al. 2022). Table 4-3 shows the resulting canister deposition and mass flow at the inlets for both the three AHSM-HS models and stand-alone AHSM-HS models. Overall, the canister deposition is very comparable between the three-module and one-module models, with the high heat (40 kW) canister deposition within 2% between models, and both the no heat and low heat (10 kW) canister deposition within 0.5% between models. The smaller, more computationally efficient, single AHSM-HS heater assembly model provides a representative deposition model of the storage module system attached to the neighboring modules.

The results show that the heated canisters have a higher deposition efficiency than the non-heated canister. This seems to correlate with the higher air flow rates through the module for the heated canister and natural convection flow.

Table 4-3. Three AHSM-HS Model Deposition Results

Model	40 kW Canister		0 kW Canister		10 kW Canister	
	Avg Inlet Mass Flow	Canister Deposition Efficiency	Avg Inlet Mass Flow	Canister Deposition Efficiency	Avg Inlet Mass Flow	Canister Deposition Efficiency
	[kg/s]	[%]	[kg/s]	[%]	[kg/s]	[%]
3 Module	0.68	11.1%	0.19	6.7%	0.45	11.0%
1 Module High Heat	0.68	9.2%				
1 Module No Heat			0.19	7.0%		
1 Module Low Heat					0.45	10.7%

4.5 Particle Resuspension

Sea spray deposition simulations for the AHSM-HS have not considered particulate resuspension. It would be conservative to assume that any deposited chloride particles would stay on the canister surface. This may be overly conservative, however. This section presents preliminary investigation into the conditions whereby solid chloride particles deposited on the AHSM-HS canister surface may resuspend. It is hoped that this analysis will produce a reasonable estimate. If it appears that resuspension is significant, further study may be necessary to include it in deposition analyses.

4.5.1 Particle Detachment Theory

The theory of particle detachment is based on a balance of forces acting on a particle adhered to a flat surface (see Figure 4-12). An assumed spherical particle is attracted to the surface material, or substrate, by some force or forces (e.g., Van der Waal and other forces, gravity, etc.). This attraction force deforms the spherical particle against the substrate. Fluid flow over the substrate generates lift (F_L) and transverse drag (F_t) forces on the particle. Lift can cause the particle to detach directly off the substrate if it overcomes the particle-substrate attraction. Drag can cause the particle to slide or roll along the substrate. Rolling is initiated by torque around point **O**.

A number of models are available to describe particle attraction force and the resulting particle deformation. Several of these are presented by Soltani and Ahmadi (1994) and Nasr et al. (2017) and will not be repeated here for brevity. For this work, two models were considered, JKR and DMT, as defined by those authors. The JKR adhesion is best for large, soft particles, whereas the DMT is more appropriate for small, hard particles. Both assume elastic deformation of the particle.

Adhesion model applicability is determined by the Tabor parameter (Nasr et al. 2017, equation 2.12)

$$\mu_T = \left(\frac{8d W_A^2}{p A} \frac{3}{9K^2 z_0} \right)^{1/3} \quad \text{Eq. 4-2}$$

where d_p is particle diameter, z_0 is the minimum equilibrium separation distance ($\approx 4 \text{ \AA}$), and K is the composite Young's modulus defined as

$$K = \frac{4}{3} \left[\frac{1-\nu_1^2}{E_1} + \frac{1-\nu_2^2}{E_2} \right]^{-1} \quad \text{Eq. 4-3}$$

W_A is work of adhesion between the particle and substrate given by (Nasr et al. 2017, equation 2.5)

$$W_A = \frac{A}{12\pi z_0^2} \quad \text{Eq. 4-4}$$

where W_A is specific to a material and A is the Hamaker constant. The Hamaker constant is computed from material-specific values (Visser 1972, equation 4):

$$A = \sqrt{A_{particle} A_{substrate}} \quad \text{Eq. 4-5}$$

The JKR model is valid when $\mu_T \gg 1$. DMT is applicable when $\mu_T \ll 1$. Neither is appropriate when $\mu_T \approx 1$.

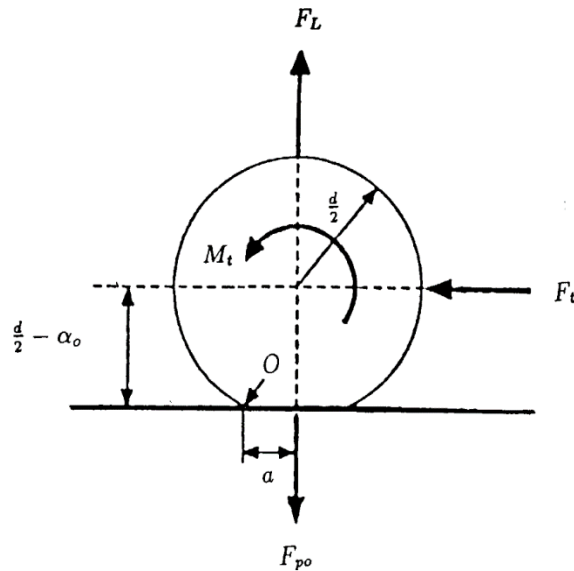


Figure 4-12. Schematic Depicting Particle Detachment Theory

4.5.2 Material Properties

For this analysis, it was assumed that the source of chloride is sea spray with generated droplet sizes from 0.2 to 150 μm (consistent with simulations by Jensen et al. [2020]). The salt mass in these droplets was

assumed to be entirely NaCl and constant even if the droplet size changed through evaporation or condensation. Furthermore, droplets of the entire size range were available at and might enter the storage module intake and deposit. When a droplet deposits on the canister surface, it was assumed that it evaporates quickly precipitating the entire salt mass. Bryan et al. (2022) may provide some justification for this assumption. Table 4-5 shows material properties used for NaCl particles deposited on a stainless steel surface. Using these assumptions and some typical values for sea water density (1023.6 kg/m³) and salt content (34.48 ppt), the expected size range of precipitated particles is 0.051 to 38 μm (Table 4-4, Figure 4-13). This work will be re-run with the site specific particle distribution as it becomes available.

Bryan and Enos (2014) observed sea salt crystals, containing NaCl, and MgSO₄ aggregates, in the Diablo Canyon SNF canisters and had this to say about particle size:

These large aggregates, which formed by evaporation of aerosolized seawater droplets, generally range in size from 5–20 μm. Although sea-salt grains occur in the finer size fractions (e.g., <2.5 μm), the majority of the salts on the tops of the Diablo Canyon packages, in terms of mass, are present as coarse aggregates such as these.

That general size range (5–20 μm) is shown in Figure 4-13 and falls within the expected particle size range in this analysis.

Table 4-4. Salt Precipitate Particle Size Estimated from Sea Spray Droplet Size at Creation.
 Sea water density was assumed to be 1023.6 kg/m³ with a salt content of 34.48 ppt composed entirely of NaCl.

Sea Spray Droplet			Precipitate Particle		
Diameter (μm)	Volume (m ³)	Mass (kg)	Mass (kg)	Volume (m ³)	Diameter (μm)
0.10	5.236E-22	5.360E-19	1.876E-20	8.684E-24	0.026
0.20	4.189E-21	4.288E-18	1.501E-19	6.948E-23	0.051
0.50	6.545E-20	6.699E-17	2.345E-18	1.086E-21	0.128
1.00	5.236E-19	5.360E-16	1.876E-17	8.684E-21	0.255
2.00	4.189E-18	4.288E-15	1.501E-16	6.948E-20	0.510
5.00	6.545E-17	6.699E-14	2.345E-15	1.086E-18	1.275
10.00	5.236E-16	5.360E-13	1.876E-14	8.684E-18	2.550
20.00	4.189E-15	4.288E-12	1.501E-13	6.948E-17	5.100
40.00	3.351E-14	3.430E-11	1.201E-12	5.558E-16	10.201
50.00	6.545E-14	6.699E-11	2.345E-12	1.086E-15	12.751
100.00	5.236E-13	5.360E-10	1.876E-11	8.684E-15	25.502
150.00	1.767E-12	1.809E-09	6.331E-11	2.931E-14	38.254
200.00	4.189E-12	4.288E-09	1.501E-10	6.948E-14	51.005
500.00	6.545E-11	6.699E-08	2.345E-09	1.086E-12	127.512

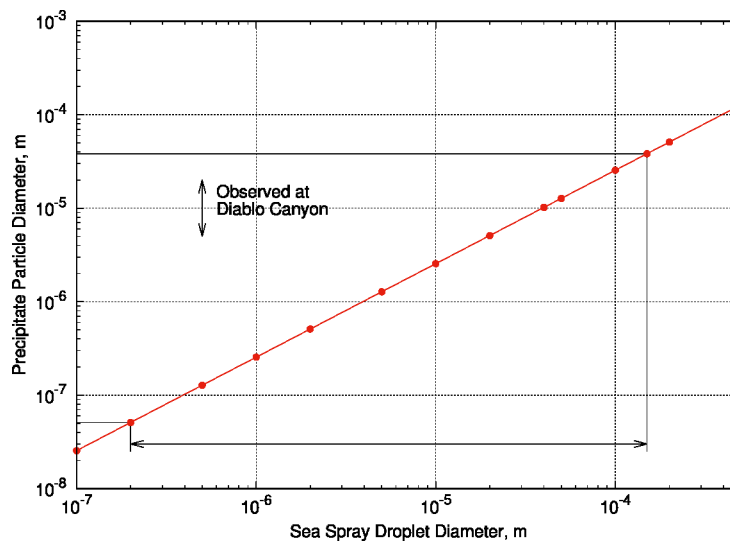


Figure 4-13. Expected Precipitate Particle Size Based on Sea Spray Droplet Size at Creation. The observed range is from data collected by Bryan and Enos (2014) at Diablo Canyon SNF canisters.

Table 4-5. Particle and Substrate Physical Properties

Particles: Halite (NaCl)		
Density, ρ	2160 kg/m ³	American Elements (2022)
Young's Modulus	4.0×10 ¹⁰ Pa	
Poisson Ratio	0.252	
Hamaker Constant	6.48×10 ⁻²⁰ J	Bergström (1997)
Substrate: 304 Stainless Steel		
Density	7850 kg/m ³	AZO Materials (2022)
Young's Modulus	1.9×10 ¹¹ Pa	
Poisson Ratio	0.265	
Hamaker Constant	2.12×10 ⁻¹⁹ J	Soltani and Ahmadi (1994)
Interface Properties		
Composite Young's Modulus	4.10×10 ¹⁰ Pa	Eq. (4-6)
Hamaker Constant	1.17×10 ⁻¹⁹ J	Eq. (4-7)
Work of Adhesion	0.0194 J/m ²	Eq. (4-8)

4.5.3 Computed Resuspension Conditions

A Matlab code (babaknasr 2019), which appears to be a companion to Nasr et al. (2017), was used to compute the critical shear velocity at which particles would detach. This code can use either the JKR or DMT adhesion models. Given the material properties above, the Tabor parameter (Eq. 4-2) was computed over the expected salt particle size range as shown in Figure 4-14. The DMT attachment model is appropriate for the expected precipitate particle size range in this analysis.

In addition to the adhesion model, two other options were enabled. One, particles were allowed to roll off the substrate into resuspension rather than requiring fluid forces to lift the particle directly off the substrate. This typically reduces the critical shear velocity considerably. Two, turbulence effects were enabled. Turbulence was represented in two ways: "Burst" assumed that peak velocity variation was important to resuspension and "Sublayer" assumed that the average of velocity variation was important. This is represented in the relation between flow velocity and critical shear velocity (Nasr et al. 2017, equation 2.26)

The estimated critical shear velocity is shown in Figure 4-15. In Star-CCM+, the wall shear stress vector, τ_w , is computed and readily available on wall boundaries. Simulated wall shear velocity can then be computed as

$$u_* = \sqrt{\frac{|\tau_w|}{\rho}} \quad \text{Eq. 4-9}$$

So, a direct comparison of AHSM-HS simulations to Figure 4-15 can be done.

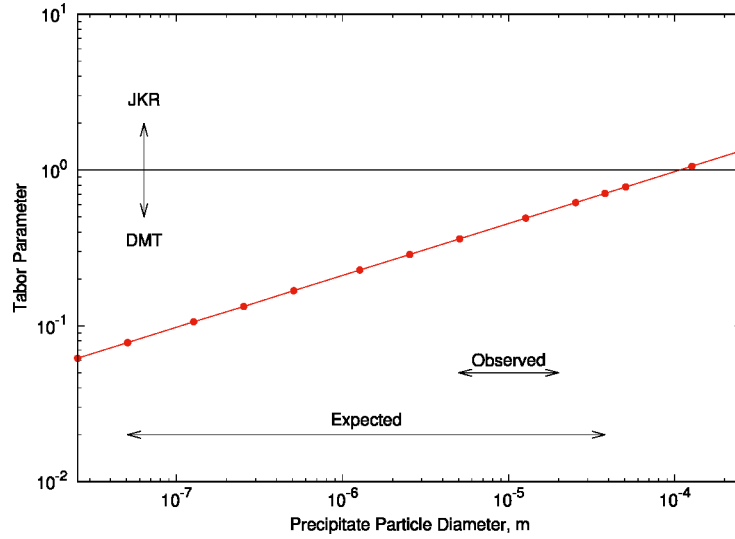


Figure 4-14. Computed Tabor Parameter over the Expected Precipitate Particle Size Range. The Tabor parameter determines the applicability of the JKR or DMT adhesion models as shown. See text for a brief observed range is from data collected by Bryan and Enos (2014) at Diablo Canyon SNF canisters.

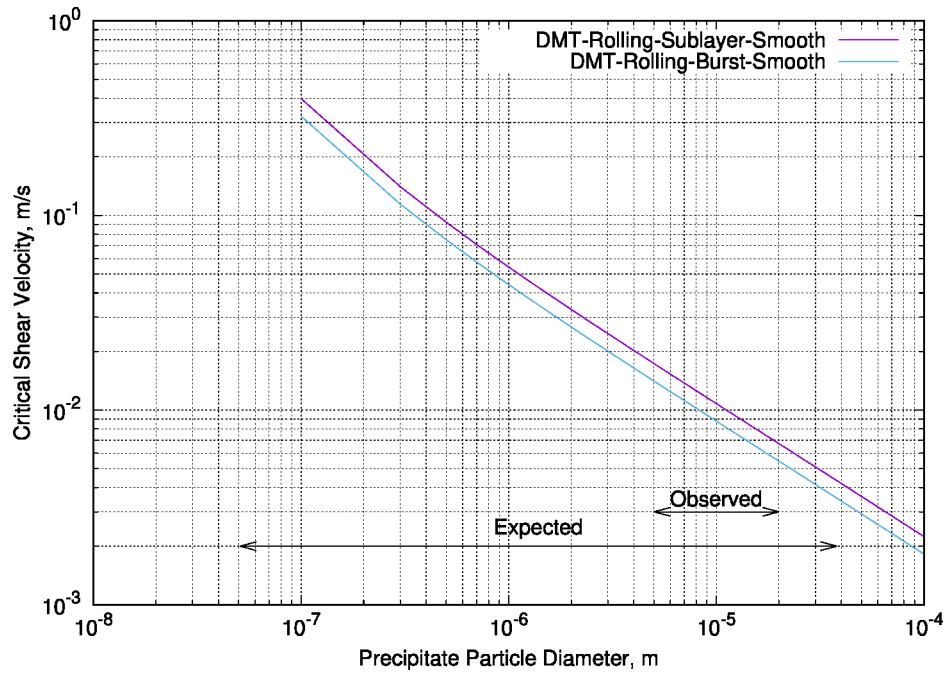


Figure 4-15. Critical Shear Velocity Computed Using the DMT Adhesion Model and Assuming that Particles Can Roll on the Substrate. The distinction between “Sublayer” and “Burst” is in how turbulent flow was represented (see text). The observed range is from data collected by Bryan and Enos (2014) at Diablo Canyon SNF canisters.

4.5.4 Additional Physics

A number of assumptions were made in this analysis. Some were made to simplify the analysis. Some were made because insufficient data was available. While these assumptions may affect the results, it is still hoped that this analysis is a reasonable estimate, at least enough to indicate whether further investigation is necessary.

This analysis did not include gravity. Gravity can only be included if it can be adjusted to the orientation of its magnitude based on the location on the SNF cylinder. Inclusion of gravity would increase critical shear velocity on the top of the AHSM-HS cylinder but lower it on the bottom. In the Matlab code used (babaknasr 2019), the effect of gravity was fixed in magnitude and direction. Some (re)coding would have been necessary to incorporate the effects of gravity.

Surface roughness is not included either. Substrate and particle roughness tends to reduce critical shear velocity, so it probably needs to be included. Several parameters are needed to describe roughness, which were not immediately available.

It was assumed here that deposited salt particles were made up entirely of halite (NaCl). In reality, sea salt content is much more complicated (Babel and Schreiber 2014). For example, Bryan and Enos (2016) describe the composition of sea salt deposition on Diablo Canyon SNF canister surfaces as follows:

The final salt assemblage at dryout consists mostly of halite, with minor amounts of Bischofite ($MgCl_2 \cdot 6H_2O$) and Kieserite ($MgSO_4 \cdot 2H_2O$) and trace amounts of Anhydrite, Carnallite ($KMgCl_2 \cdot 6H_2O$), and Hydromagnesite ($Mg_5(CO_3)_4(OH)_2 \cdot 4H_2O$). As sea-spray aerosols dry out, these salts are precipitated, and salts, or a mixture of salts and brine, may be deposited on the canister surface.

It is not known if the presence of magnesium chlorides and sulfates significantly changes the particulate material properties, Young's modulus and work of adhesion, from those of pure halite. Data for such a combination could not be located.

4.6 Site Model

The CDFD site model concept was introduced by Suffield et al. (2021). In that work, a site model was prepared for a fictitious reactor site with SNF stored on-site. Suffield et al. (2022) similarly prepared and exercised a site model for an existing decommissioned nuclear generation site that might be a candidate for CDFD deployment. However, the site was not yet identified, so renderings of simulation results were limited to the ISFSI and a small area around it. These applications were used to demonstrate possible site model uses. Recently, a candidate CDFD site was identified on the PNNL-Sequim campus, which houses the Marine and Coastal Research Laboratory (MCRL). This has provided an opportunity to prepare and exercise a site model.

The PNNL-Sequim campus is located in western Washington state on the north end of the Olympic peninsula on the western shore of Sequim Bay (Figure 4-16). The city of Sequim is located just west of the campus. A number of nearby weather stations are available to supply necessary data, like wind speed. Figure 4-16 shows wind roses generated from the entire record of some nearby weather stations.^a

^a Sources: WSU Ag Weather Net (<https://weather.wsu.edu>), National Centers for Environmental Information, Hourly/Sub-Hourly Observational Data (<https://www.ncei.noaa.gov/maps/hourly>).

Observed wind patterns show an interesting pattern. A very strong westerly flow is present in the Strait of Juan de Fuca. A more southerly flow comes from Puget Sound. The area around the MCRL campus appears quite sheltered. A WSU station very near the campus (“Smith Farm”) shows that wind speeds are quite low most of the time but can be strong from the west and southeast.

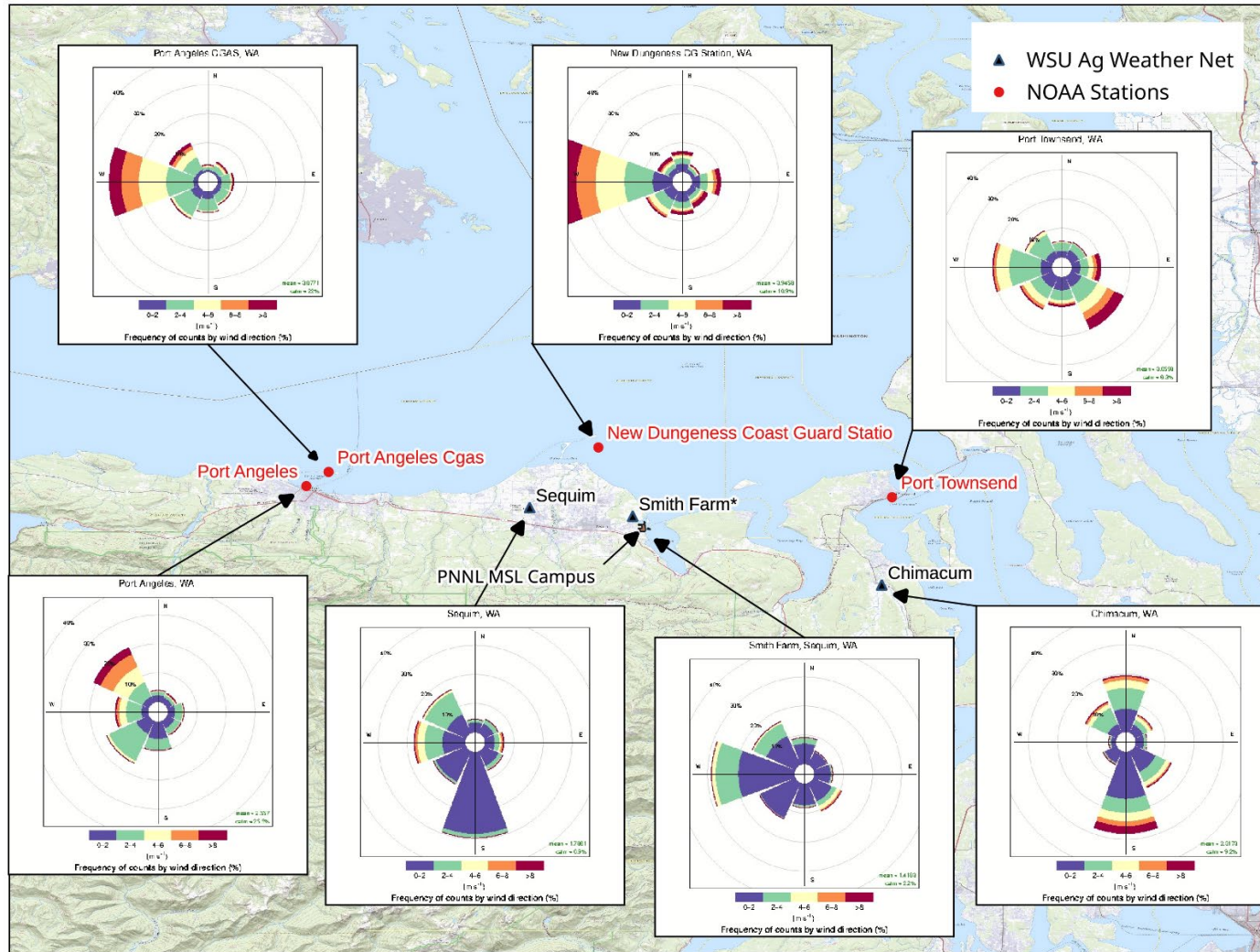


Figure 4-16. PNNL-Sequim and Locations of Nearby Weather Stations. Wind roses shown are for the available station record.

4.6.1 Fire Dynamics Simulator

The Fire Dynamics Simulator (FDS) (McGrattan et al. 2013) is a CFD code that simulates low Mach number air flows and the effects of combustion on those flows. FDS was developed and is maintained by the U.S. National Institute of Standards and Technology (NIST). The primary FDS application space has included thermally driven flows within buildings, design of fire suppression systems, and forensic analysis of historic building fires. The FDS application space has expanded to include outdoor air flow and fire, including wildfire and pollutant dispersion, which makes it applicable to simulations of stored SNF environs at the site scale.

FDS has a number of capabilities that make it attractive as a simulator at the site scale. FDS uses the large eddy simulation (LES) method for air phase simulation. Relative to Reynolds-averaged Navier-Stokes (RANS), LES preserves larger, transient, turbulent flow structures given sufficient mesh resolution. Such turbulent structures can be significant, particularly to the dispersion of Lagrangian particles. FDS also simulates thermal energy transport and the effect of thermal gradients and radiation on the flow field. Full theoretical documentation of these capabilities can be found in McGrattan et al. (2017). A more detailed account of FDS history and capability is presented by NIST (2018).

4.6.2 Application to Sequim Site

Two possible CDFD sites have been identified: “Field” site and “Robb House.” FDS was configured to simulate a 1.6×1.2 km area centered on the “Field” site (Figure 4-17). Through the Washington Light Detection and Ranging (LIDAR) Portal,^b a 2019 LIDAR survey was available for the area (titled “Olympics South Opsw 2019”). A digital terrain model (DTM) and digital surface model (DSM) with 1 m resolution were obtained (Figure 4-18). A DSM is the result of a LIDAR survey and contains all reflective surfaces, like vegetation and buildings, in addition to the ground surface. A DTM is a processed DSM in which identifiable vegetation and buildings are removed. The DTM was used to prepare a geometry for FDS. All elevations lower than 1.2 m were set to 1.2 m so that water surfaces were at the same elevation.

^b <https://lidarportal.dnr.wa.gov>



Figure 4-17. PNNL-Sequim Campus. The 1.6×1.2 km FDS model domain is centered on the proposed Field CDFD site.

Some simulations were performed with a 2 m spatial resolution. This configuration of FDS has not been calibrated or validated, so these simulations simply exercise the configuration. Results should be considered preliminary.

In the first simulation, a constant ambient westerly wind of 5.0 m/s was imposed. Figure 4-19 shows some instantaneous velocities along some planes in the area around the Field site. The vertical plane goes through the middle of the field. The horizontal plane is at 30 m elevation. As one would suspect, this area is rather sheltered. The wake of the hill above Field is plainly visible as is the wake of the near-shore cliff. Figure 4-20 shows some massless particle tracks (or streak lines) from that simulation.

A second simulation was performed where the direction of a 5 m/s ambient wind was swept 360 degrees, starting from north, in 2 hours. Figure 4-21 shows how simulated wind speed and direction responded at the Robb House and Field sites. The Field site shows a lower wind speed at nearly all wind directions.

In a third simulation, a pad with an AHSM-HS on top was inserted into the model geometry at the Field site. The same westerly 5.0 m/s ambient wind was imposed. Figure 4-22 shows how the existence of an AHSM-HS might change the velocity field (compare with Figure 4-19).

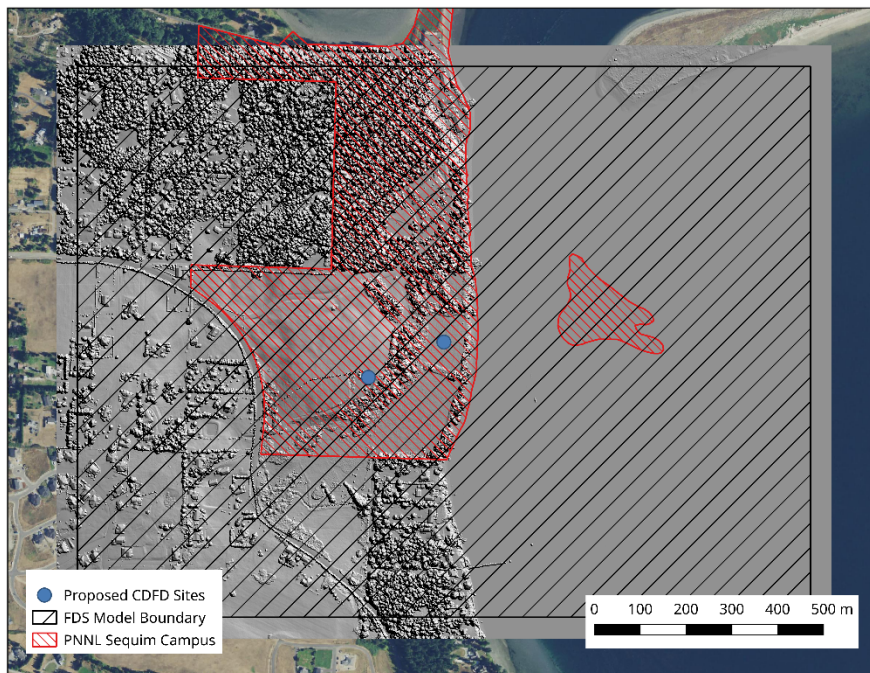
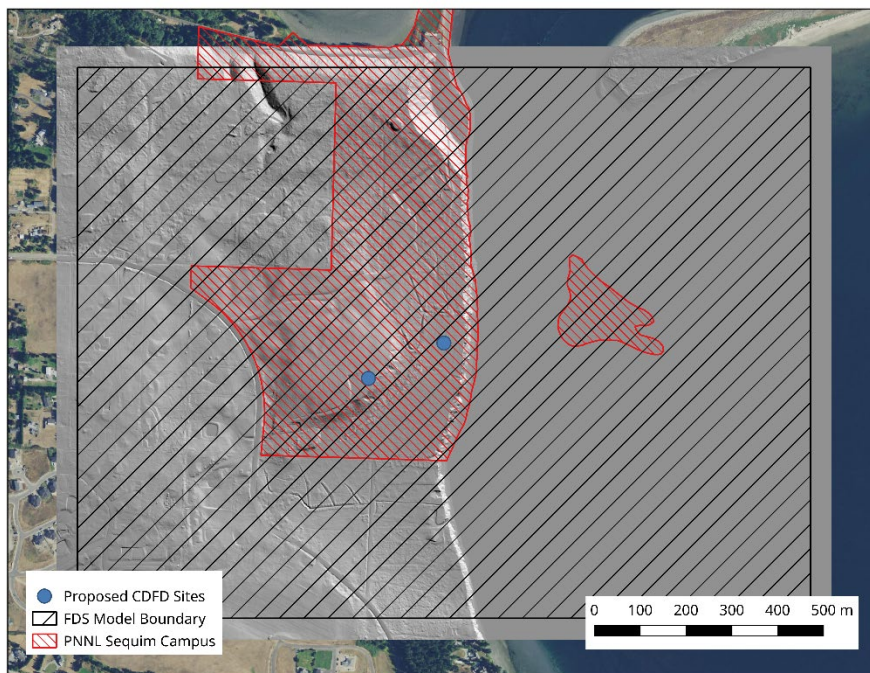


Figure 4-18. LIDAR-Derived DTM (Above) and DSM, (Below) Available for the PNNL-Sequim Site.

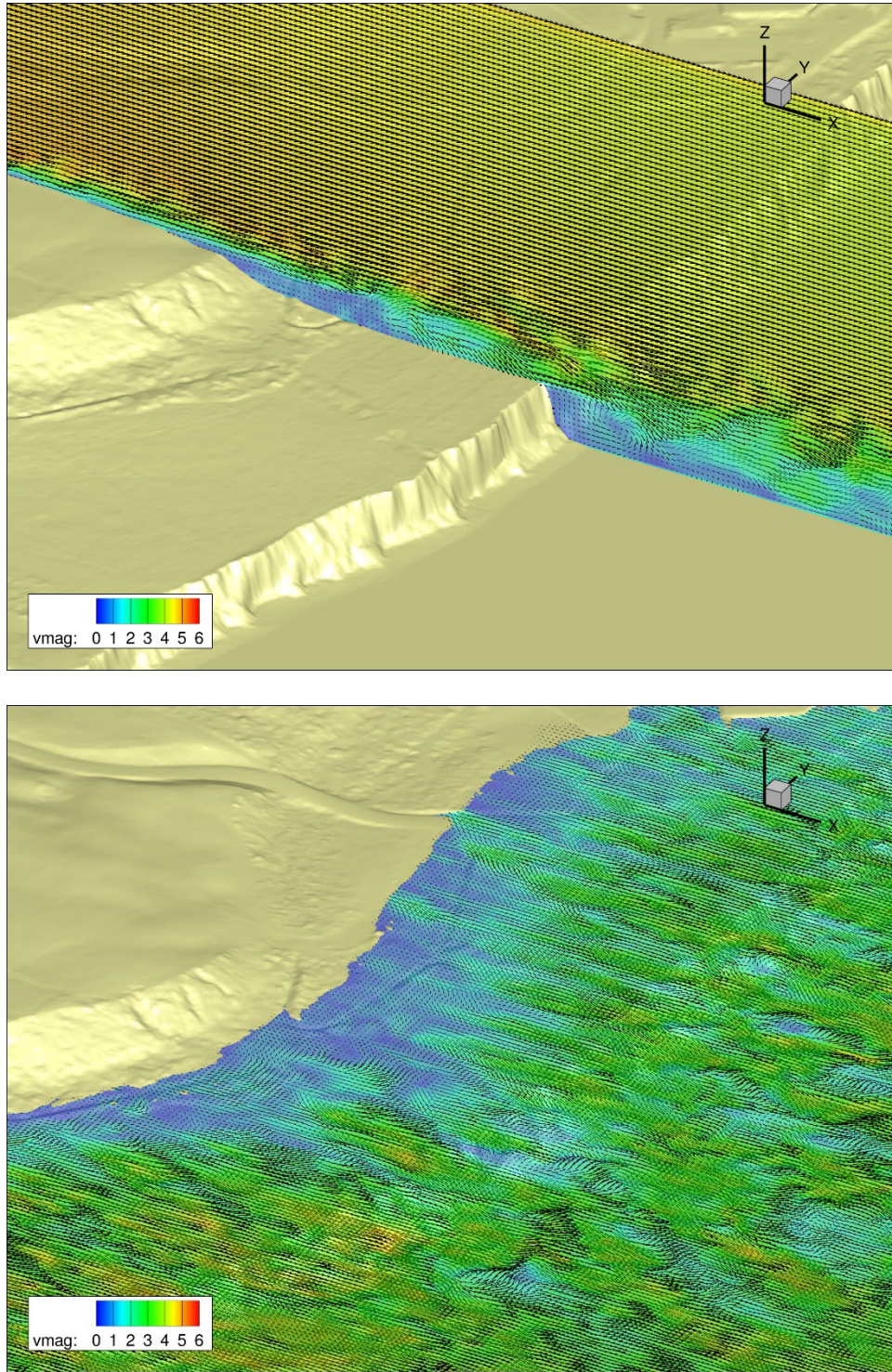


Figure 4-19. Simulated Instantaneous Velocity in the Field along an East–West Plane (Above) and at 30 m Elevation (Below). The ambient wind was 5 m/s from the west.

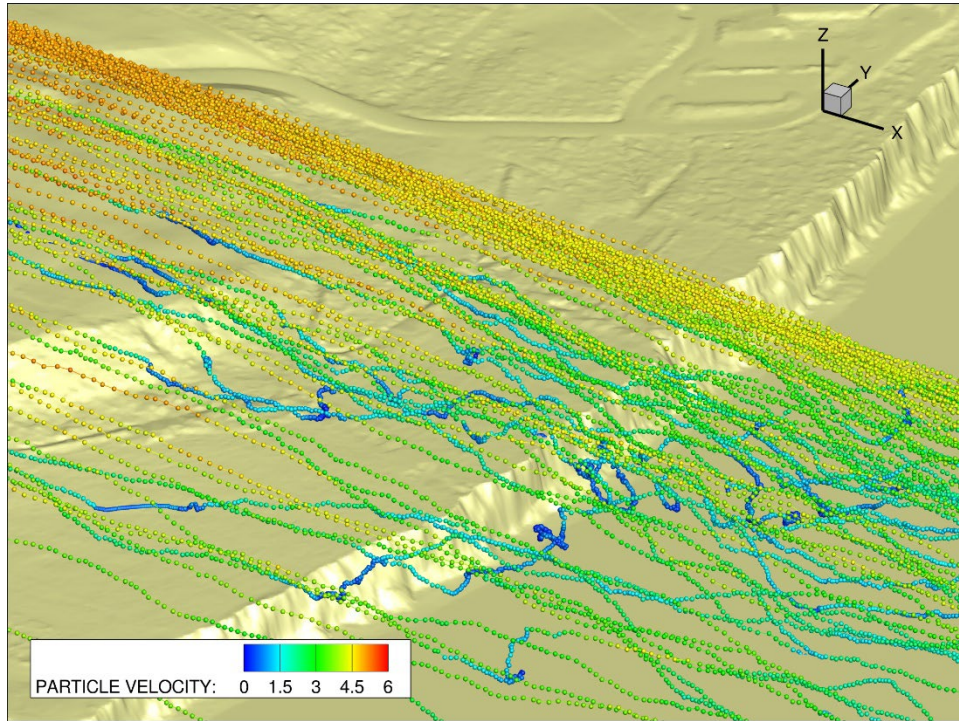


Figure 4-20. Massless Particle Tracks (or Streak Lines) from a Simulation with an Ambient Westerly Wind of 5 m/s Imposed.

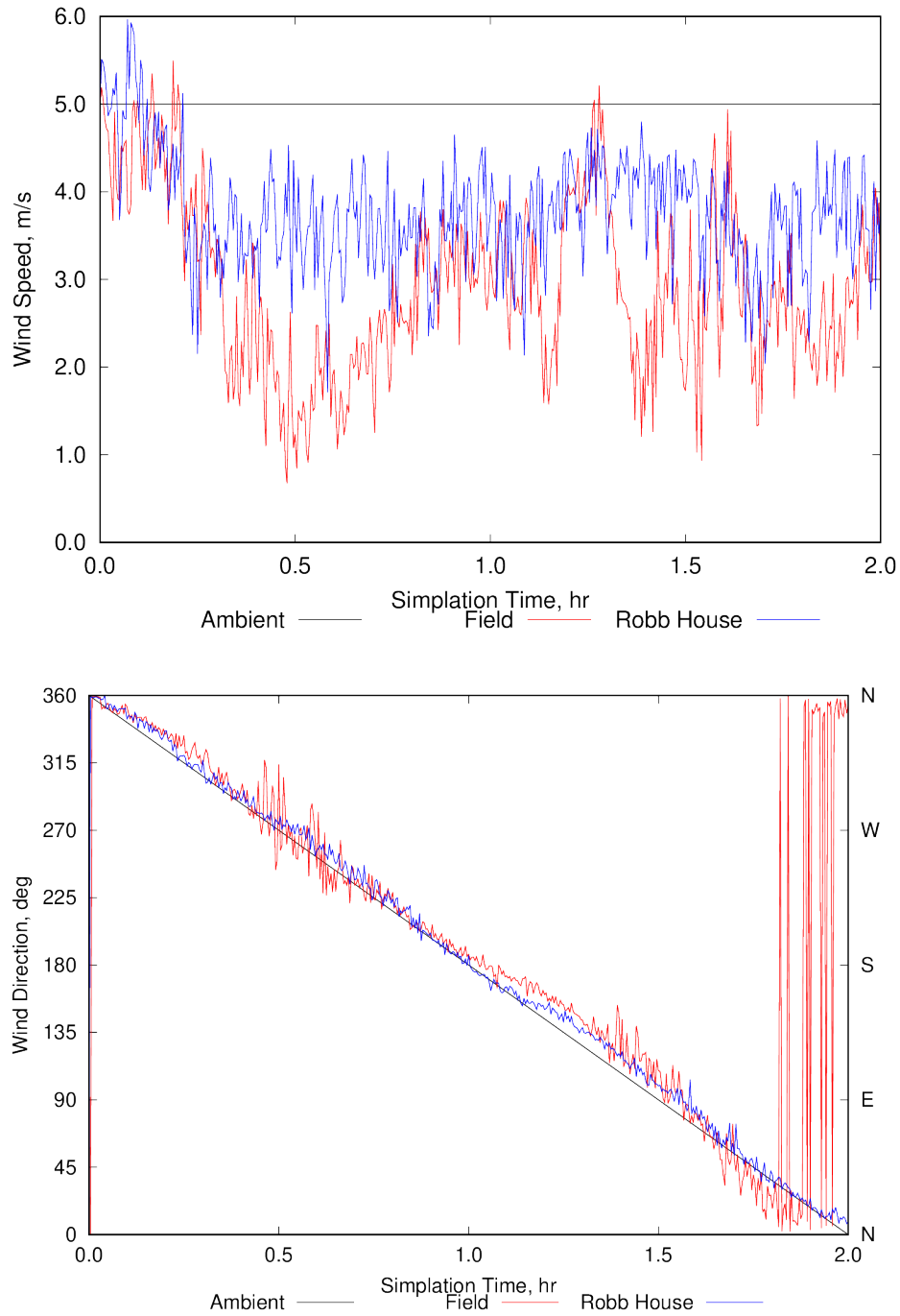


Figure 4-21. Simulated Wind Speed (Above) and Direction (Below) at the Robb House and Field Sites.

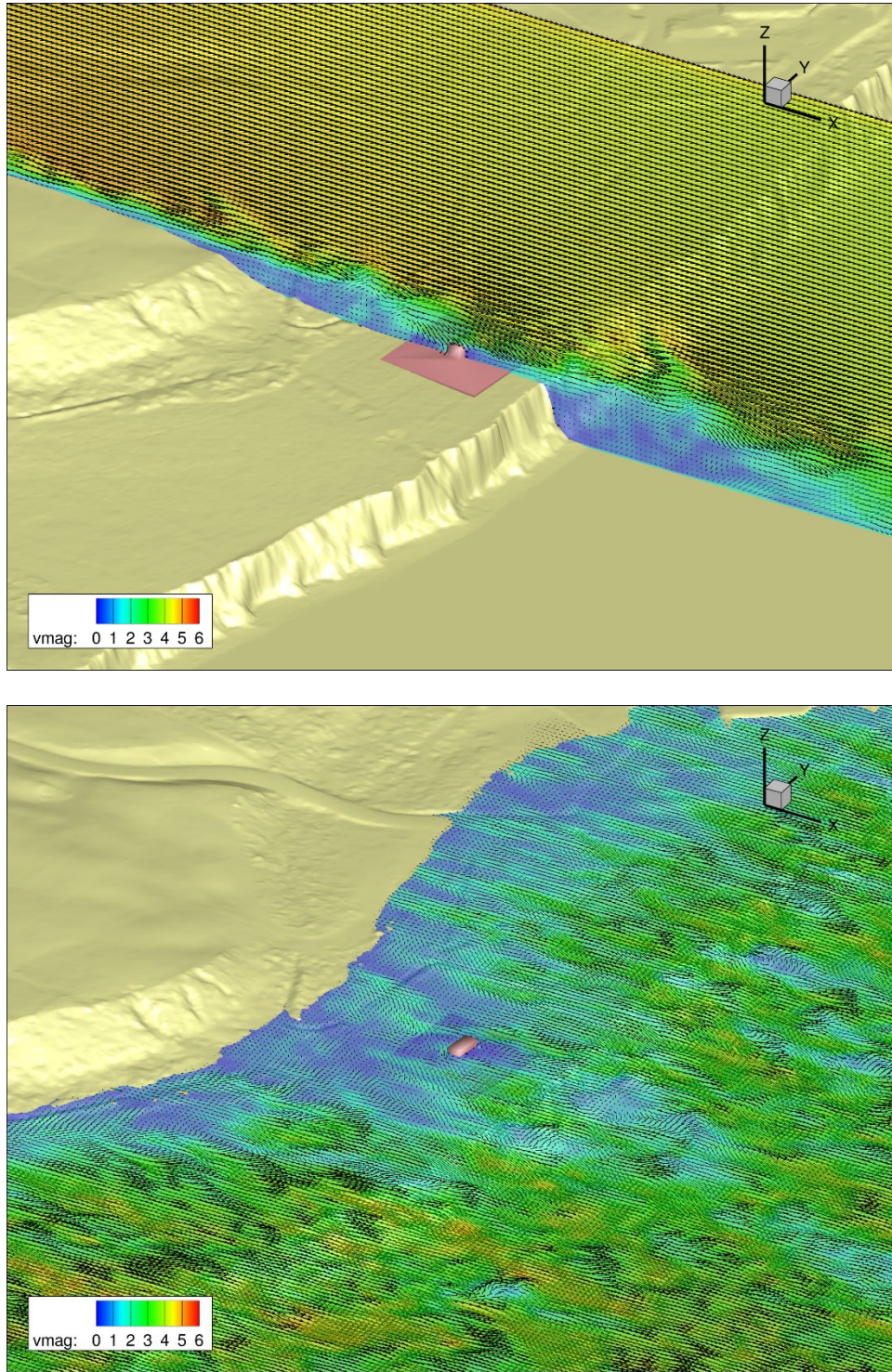


Figure 4-22. Simulated Instantaneous Velocity around an Imaginary AHSM-HS in the Field Along an East–West Plane (Above) and at an Elevation of 30 m (Below). Simulation conditions and view are the same as Figure 4-19

4.7 Connecting the Site Model and Stand-Alone Model

The long-term plan is to have the site model provide boundary conditions, such as wind speed and direction, to the detailed stand-alone STAR-CCM+ models (the single and three AHSM-HS models). Currently, the stand-alone models assume thermally driven natural convection flow without any influence of external airflow. Wind flow around the storage modules will cause a pressure distribution along external surfaces and openings, resulting in a pressure difference between the inlets and outlets of the storage module, and this will impact airflow through the module. The stand-alone model will need to account for both wind and thermally driven flows in the heated storage modules. To investigate how to account for wind in the stand-alone model, two different wind effects models were developed: a STAR-CCM+ wind effects model that modeled the external environment around the AHSM-HS and flow through the module, and an FDS wind effects model that modeled the external environment surrounding the AHSM-HS but did not model flow through the module. The FDS wind effects model with no flow through AHSM-HS will be more representative of the FDS site model and will be used to feed boundary conditions to the stand-alone STAR-CCM+ AHSM-HS heater assembly model. The air flow through the STAR-CCM+ wind effects model will be compared to the resulting air flow through the AHSM-HS with the stand-alone model and FDS pressure boundary conditions.

Preliminary modeling concluded that only positive pressures at the inlets of the wind effects model represent wind at that boundary. The effect of a positive pressure can be seen in Figure 4-23 and Figure 4-24. Figure 4-23 shows a 5 m/s wind blowing directly at the inlets, which would result in wind driving flow into the inlets, resulting in a positive pressure at the inlets. Figure 4-24 shows a 5 m/s wind that originates from behind the model, which is not expected to result in flow being driven into the inlets, and results in a negative pressure at the inlets. It is important to note that a previous study with the STAR-CCM+ wind effects model concluded backflow should not be a concern with the current AHSM-HS outlet geometry (Suffield et al. 2022). The AHSM-HS outlets are open on two sides, allowing wind-blown air to pass from one side of the outlet to the other, instead of taking a 90-degree turn into the AHSM-HS module. Based on the results, positive outlet pressures can be neglected for the AHSM-HS.

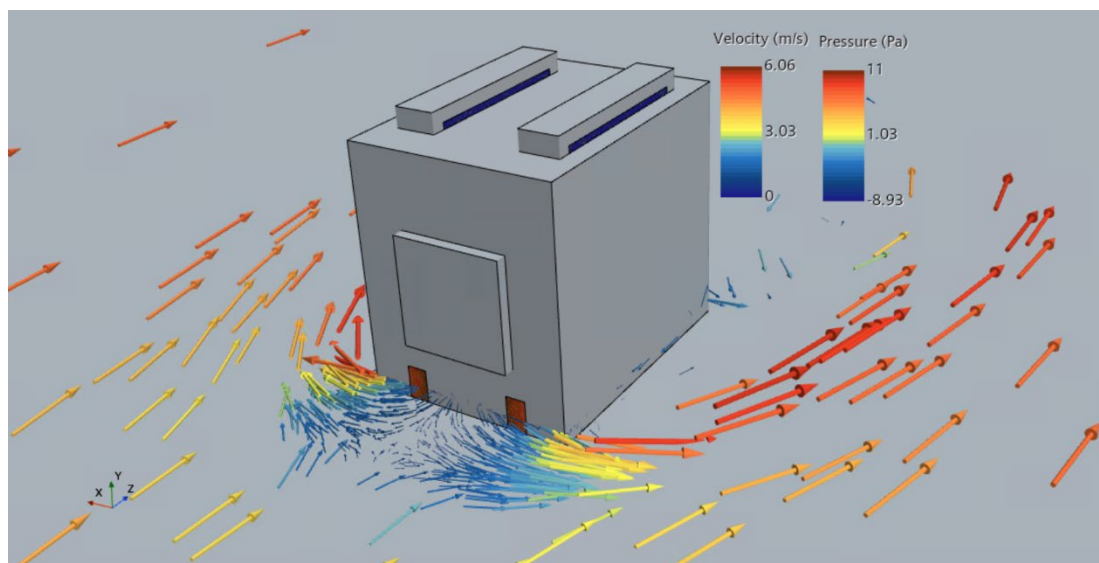


Figure 4-23. 5 m/s Wind Blowing Directly at the AHSM-HS Inlets.

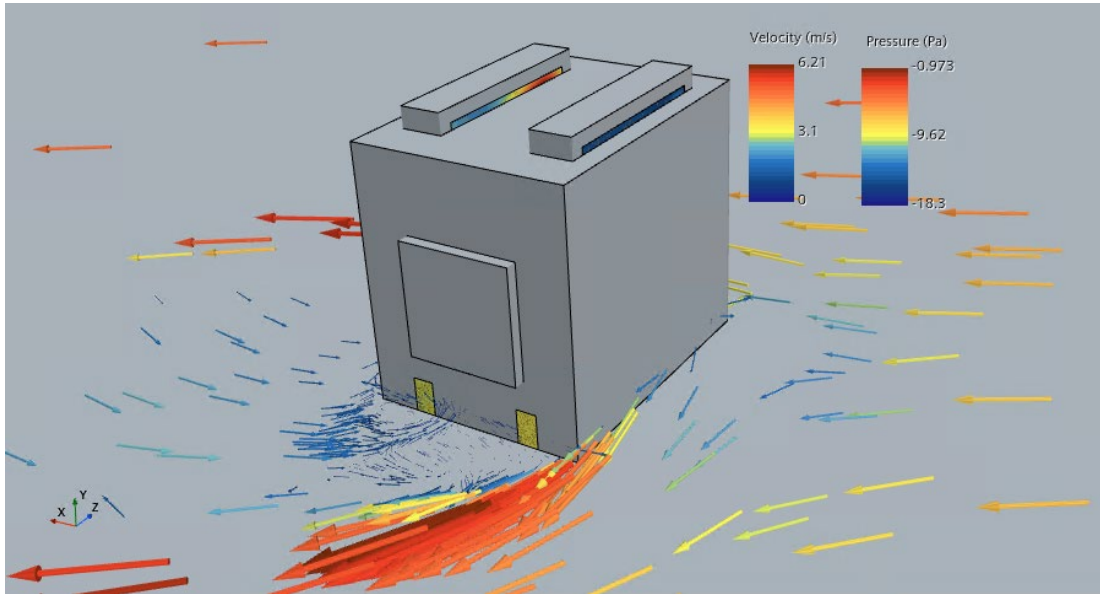


Figure 4-24. 5 m/s Wind Blowing from Behind the AHSM-HS Inlets.

4.7.1 STAR-CCM+ Wind Effects Model

The previously developed STAR-CCM+ single AHSM-HS wind effects model (Suffield et al. 2021; Suffield et al. 2022) was updated to move the external environment boundaries further from the module. A sensitivity study was performed looking at various square and half-sphere sizes of the external environment with the module placed in the center. Figure 4-25 shows the results of the sensitivity study. A 220 m diameter semi sphere (110 m radius) was selected to use as the external environment geometry going forward. Figure 4-27 shows the resulting geometry of the STAR-CCM+ wind effects model.

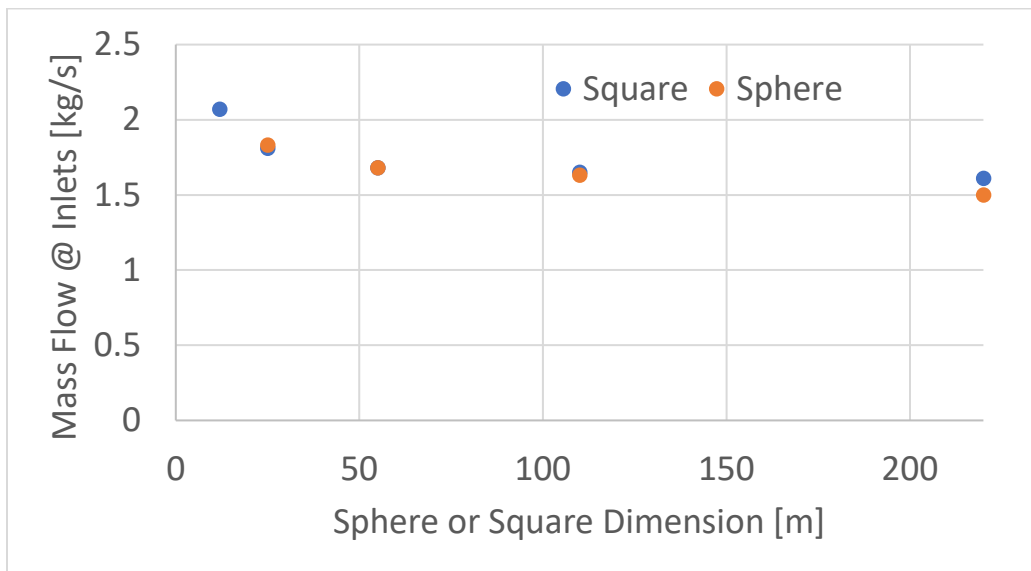


Figure 4-25. External Boundary Size Sensitivity Study Results for the STAR-CCM+ Wind Effects Model

In addition to looking at the sensitivity of the external boundary shape, an external boundary mesh size investigation was performed. The mesh size sensitivity study is isolated to the external boundary. No mesh refinements are performed on the region inside of the cask. The motivation for this exercise is to find the coarsest external boundary mesh while minimizing the mass flow rate error through the cask. From the previous investigation, the 220 m square boundary (corresponds to the 110 m radius semi-sphere external boundary) was selected to test five different mesh sizes. These results are applicable to the semi-spherical boundary geometry as well. The external boundary mesh sizes range from 8 m cells to 0.5 m cells, which results in a total mesh count for the external boundary of about 650,000 to 36 million cells. This range in mesh cell size covers a coarse to very fine mesh for the external boundary. The same parameters were run for each mesh size to determine solution convergence. The flow through the cask is driven by a 5 m/s wind normal to the inlets of the cask.

Figure 4-26 shows the results of the mesh sensitivity study. The results show that the mass flow rate quickly converges with two successive refinements. Mass flow rate is chosen as the solution parameter of interest for this investigation. The two coarse meshes have 8 m and 4 m cells. The next refinement has 2 m cells. Even with this strong evidence of convergence, the 8 m mesh is still very close to the converged solution. The conclusion of this investigation is that the 4 m mesh offers the best computational efficiency with the least amount of computational error. Moving forward, the 4 m mesh cell size is recommended for the external flow region.

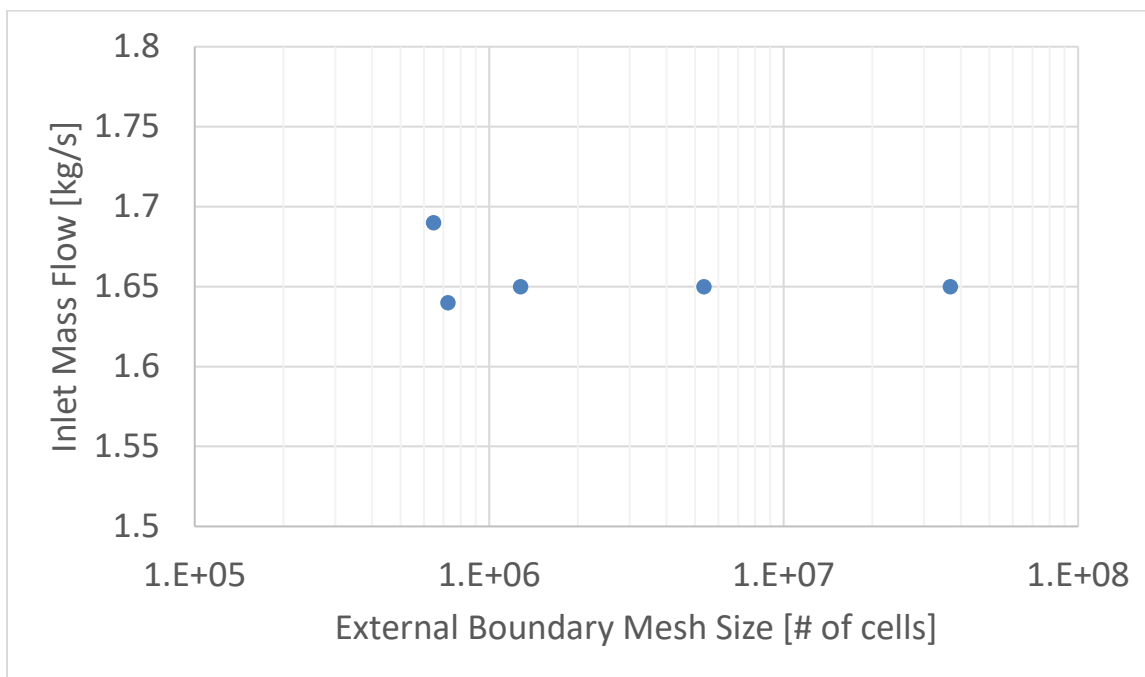


Figure 4-26. External Boundary Mesh Size Sensitivity Study Results for the STAR-CCM+ Wind Effects Model



Figure 4-27. Geometry for STAR-CCM+ Wind Effects Model

From this external boundary shape and mesh size study, the recommended external boundary is a 110 m radius (220 m diameter) semi sphere with a 4 m mesh size. Although the square external boundary shape offers slightly better performance over the semi-sphere boundary, the ease of boundary condition input for the semi-sphere model far outweighs the performance advantage.

The model was run at three different windspeeds: 0.5 m/s (1 mph), 2.5 m/s (6 mph), and 5 m/s (11 mph). The wind direction was varied from 0-degrees to 180-degrees in 15-degree increments, with 0-degrees corresponding to the wind blowing directly at the inlets (i.e., the air flow is perpendicular to the inlets). The STAR-CCM+ wind effects model was run assuming both no thermal loads (unheated canister with no solar loadings) and with a 40 kW heat load. For the no thermal load condition, air flow was driven by wind only, but for the high heat load cases (40 kW), the air flow was driven by both wind and natural convection. Figure 4-28 shows a cross-sectional velocity vector plot through the center of an inlet on the AHSM-HS at a 5 m/s wind and 0-degree wind angle. The results for the STAR-CCM+ wind effects model is presented in section 4.7.4.

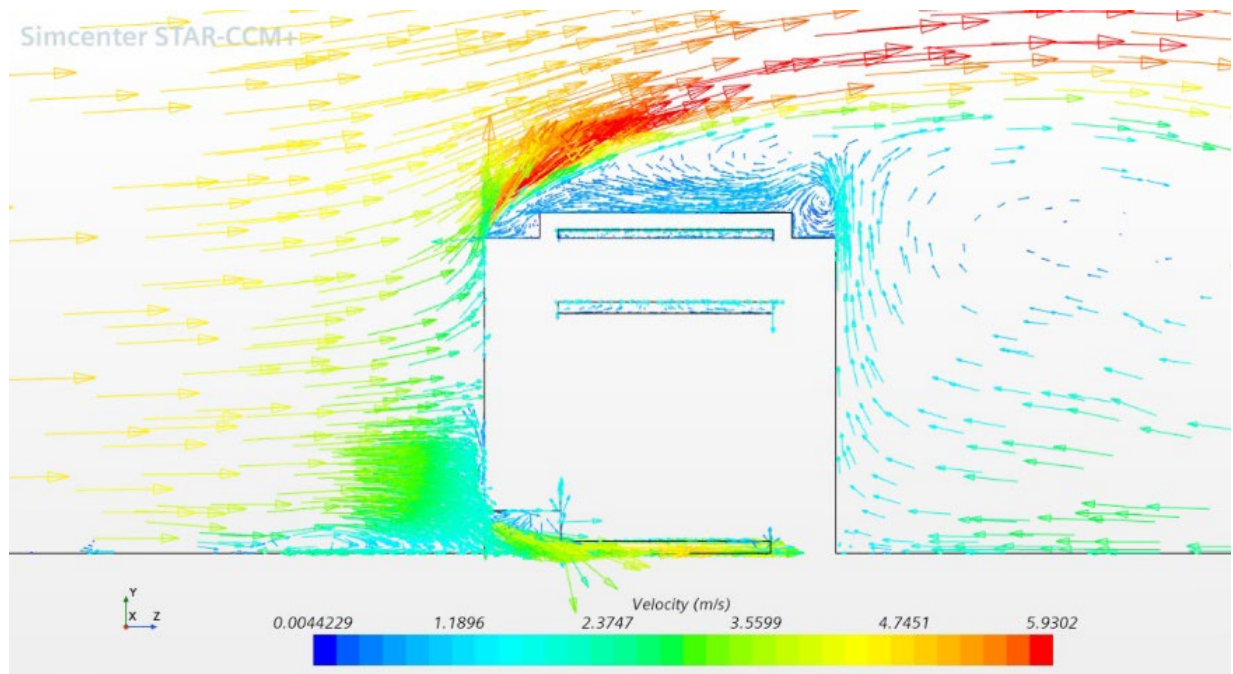


Figure 4-28. Cross-Sectional Velocity Vector Plot through the Center of an Inlet on the AHSM-HS for the STAR-CCM+ Wind Effects Model

4.7.2 FDS Wind Effects Model

An FDS wind effects model was constructed of a single AHSM-HS module with no flow through the module. The model applies a 50 m square domain to closely match the STAR-CCM model. The near-geometry cubic mesh has a 0.125 m resolution, which progressively coarsens to 0.5 m near the boundaries for computational efficiency. This mesh size distribution appeared reasonably converged in basic mesh sensitivity testing. Figure 4-29 shows the progressive mesh refinement zones.

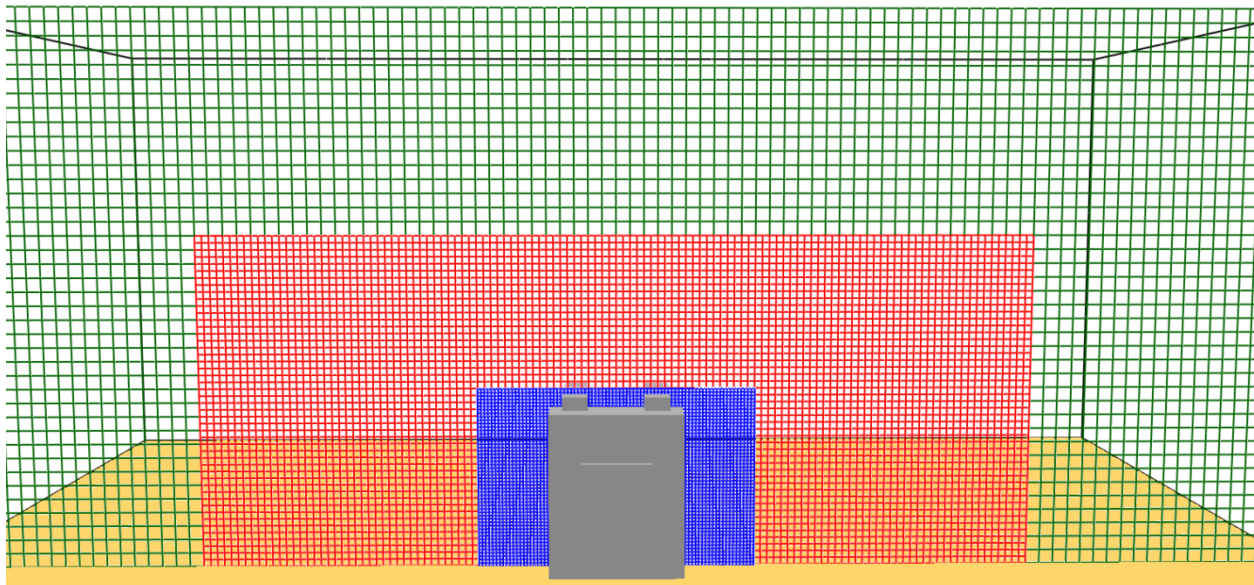


Figure 4-29. Cross Section View of Mesh for the FDS Wind Effects Model

Inlet pressures were measured by placing point probes near the center of the inlet surface in the nearest grid cell to the wall. Outlet pressures were measured by placing 3-point probes along the outlet surface—near the front edge, in the middle, and near the rear edge—and averaging the three pressures at each timestep. All probes used the FDS built-in “wall pressure” measurement, which reports the pressure on the wall at the chosen point. Figure 4-30 shows an example of inlet and outlet pressure probe locations, where the point probes are highlighted in green.

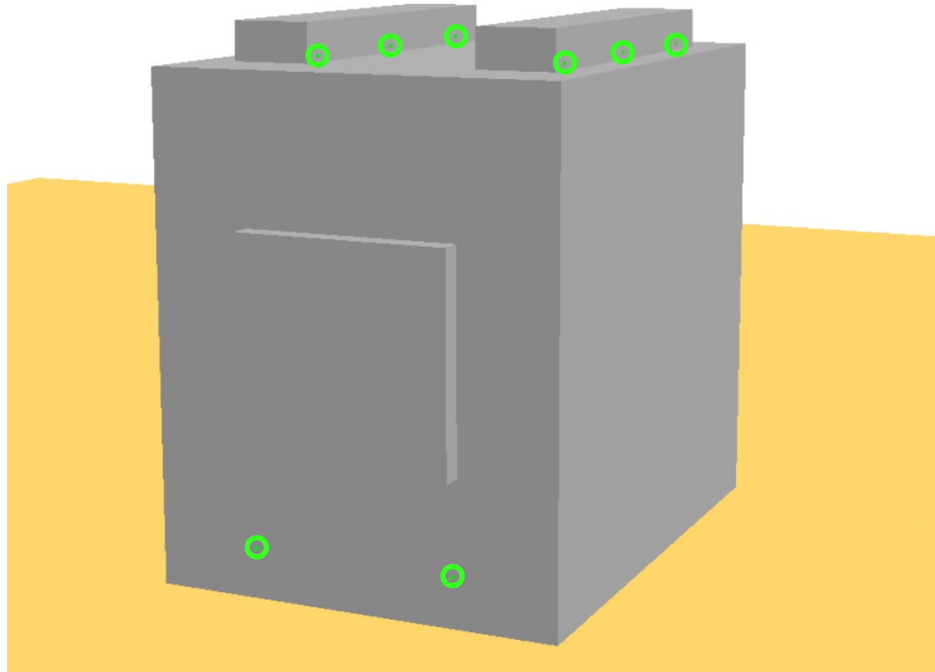


Figure 4-30. Example of FDS Wind Effects Pressure Probe Locations

The FDS wind effects model was also run at three different windspeeds of 0.5 m/s (1 mph), 2.5 m/s (6 mph), and 5 m/s (11 mph), and the wind direction was varied from 0-degrees to 180-degrees in 15-degree increments. The 0-degree wind angle corresponded to the wind blowing directly at the inlets (i.e., the air flow is perpendicular to the inlets). Figure 4-31 shows a velocity vector of flow around the AHSM-HS at a 5 m/s wind and 0-degree wind angle.

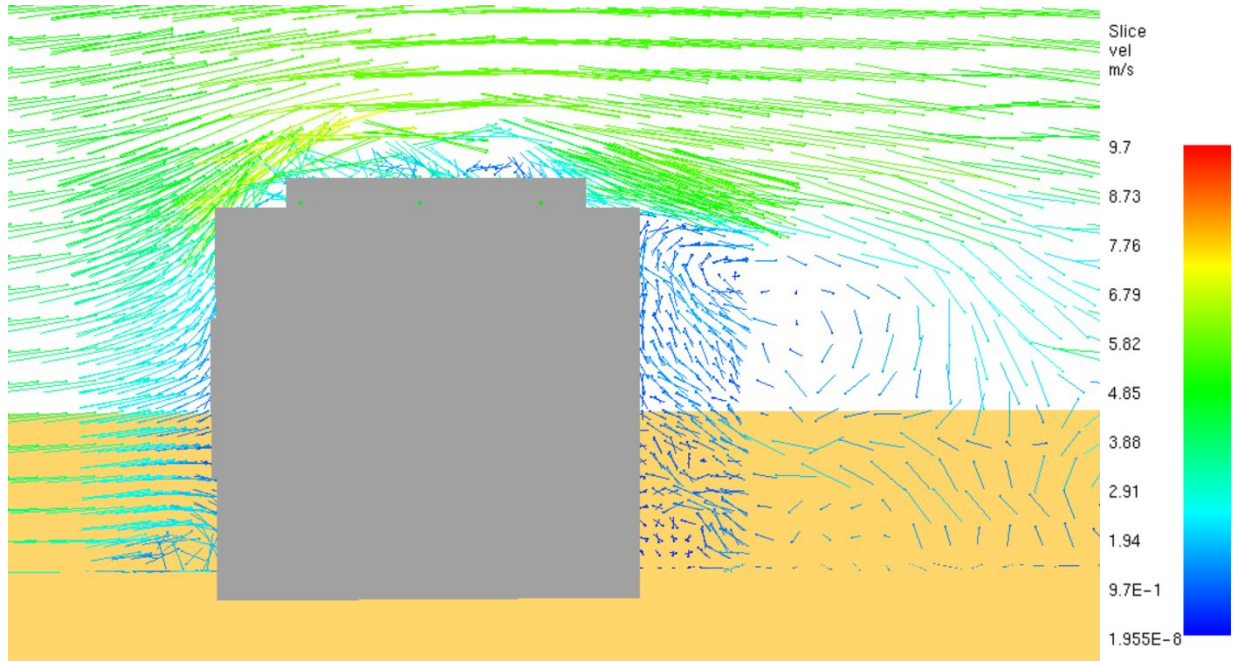


Figure 4-31. Velocity Vector Plot for Flow Around the AHSM-HS for the FDS Wind Effects Model

The resulting pressure differences for the FDS wind effects model are given in Table 4-6. The pressure difference represents the difference between the maximum inlet pressure and maximum outlet pressure:

$$\Delta P = P_{\max_inlet} - P_{\max_outlet} \quad \text{Eq. 4-10}$$

It was determined that using the difference in maximum pressure at the inlets and outlets was able to better capture flow effects across all wind angles than taking the average surface pressure difference at the inlet and outlet. Figure 4-32 shows the inlet and outlet numbering scheme. The maximum pressure difference between inlet 1 and outlets 1 and 2 were applied to inlet 1, and the maximum pressure difference between inlet 2 and outlets 3 and 4 were applied to inlet 2. A pressure of zero means that a positive pressure was not seen at the inlet for that wind speed and direction.

Table 4-6. FDS Wind Effects Pressure Difference Results

Wind Direction	Wind Speed	ΔP Inlet 1	ΔP Inlet 2
[deg]	[m/s]	[Pa]	[Pa]
0	0.5	0.4	0.4
30	0.5	0.3	0.2
45	0.5	0.4	0.2
60	0.5	0.5	0.3

Wind Direction	Wind Speed	ΔP Inlet 1	ΔP Inlet 2
90	0.5	0.0	0.2
120	0.5	0.0	0.2
135	0.5	0.1	0.1
150	0.5	0.2	0.2
180	0.5	0.1	0.1
0	2.5	5.3	5.3
30	2.5	6.1	4.3
45	2.5	5.9	3.2
60	2.5	5.0	1.7
90	2.5	0.0	2.3
120	2.5	0.0	0.0
135	2.5	0.0	0.0
150	2.5	2.6	2.1
180	2.5	1.5	1.5
0	5	17.1	17.0
30	5	21.5	15.1
45	5	21.4	9.5
60	5	18.8	4.1
90	5	0.0	0.0
120	5	0.0	0.0
135	5	0.0	0.0
150	5	9.1	0.0
180	5	4.2	4.2

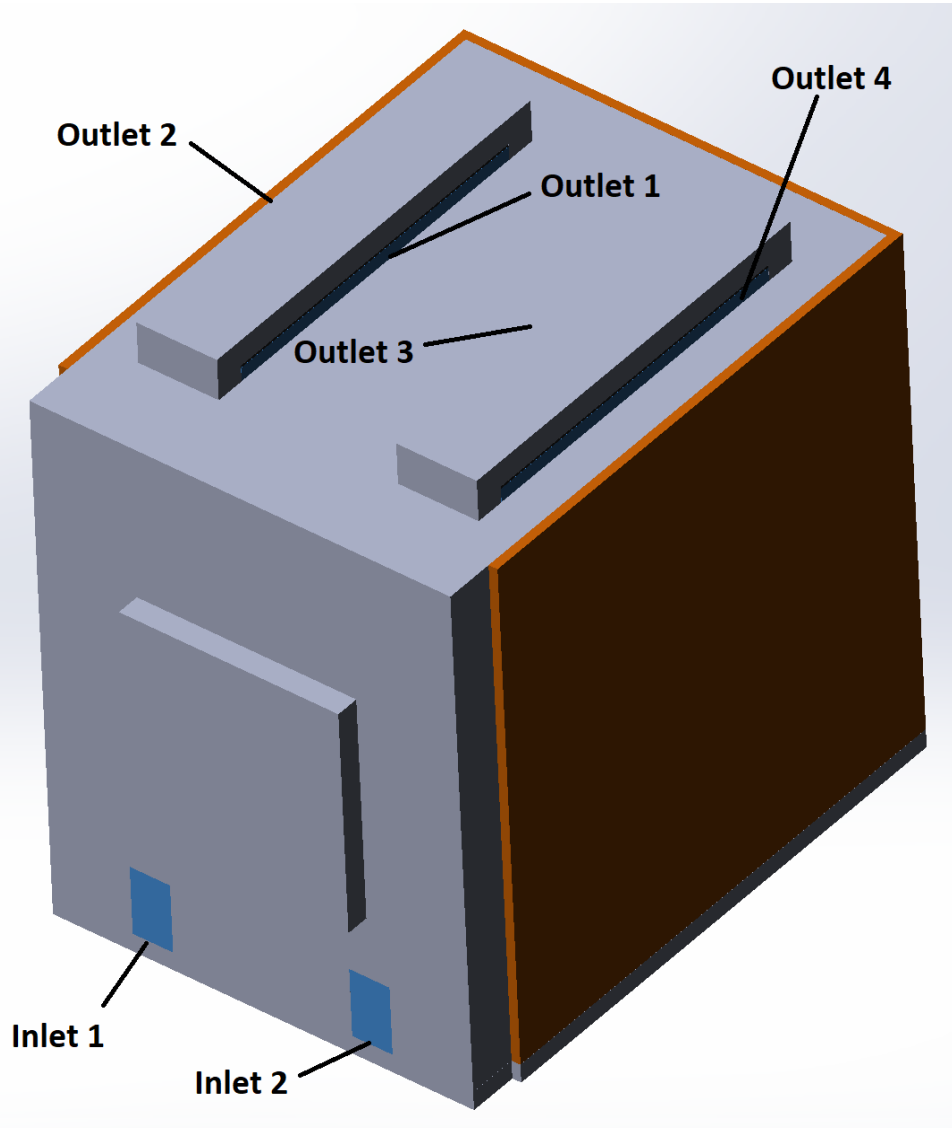


Figure 4-32. AHSM-HS Inlet and Outlet Numbering Scheme

4.7.3 Stand-Alone AHSM-HS Model

The pressure differences given in Table 4-6 were applied to the inlets of the stand-alone AHSM-HS 32PTH2 heater assembly model. The stand-alone model was then run with pressure conditions corresponding to the three different windspeeds of 0.5 m/s (1 mph), 2.5 m/s (6 mph), and 5 m/s (11 mph), and wind directions from 0-degrees to 180-degrees. Both no thermal load (0 kW) and high heat load (40 kW) cases were run with the stand-alone model.

4.7.4 Inlet Mass Flow Results

The resulting mass flow through the inlets of the AHSM-HS are plotted for both the STAR-CCM+ wind effects model and STAR-CCM+ stand-alone model in Figure 4-33 for the no thermal loads cases (0 kW) and Figure 4-34 for the high heat load cases (40 kW). The air flow for the stand-alone model with natural

convection flow only is also plotted with the results (for the 0 kW case, the mass flow is zero since there are no thermal loads to drive natural convection). Overall, the mass flow results compare well between the STAR-CCM+ wind effects model and stand-alone model. The FDS model pressure boundary conditions are capturing flow effects at most angles. This pressure difference method will be used to feed boundary conditions from the site model to the stand-alone AHSM-HS models.

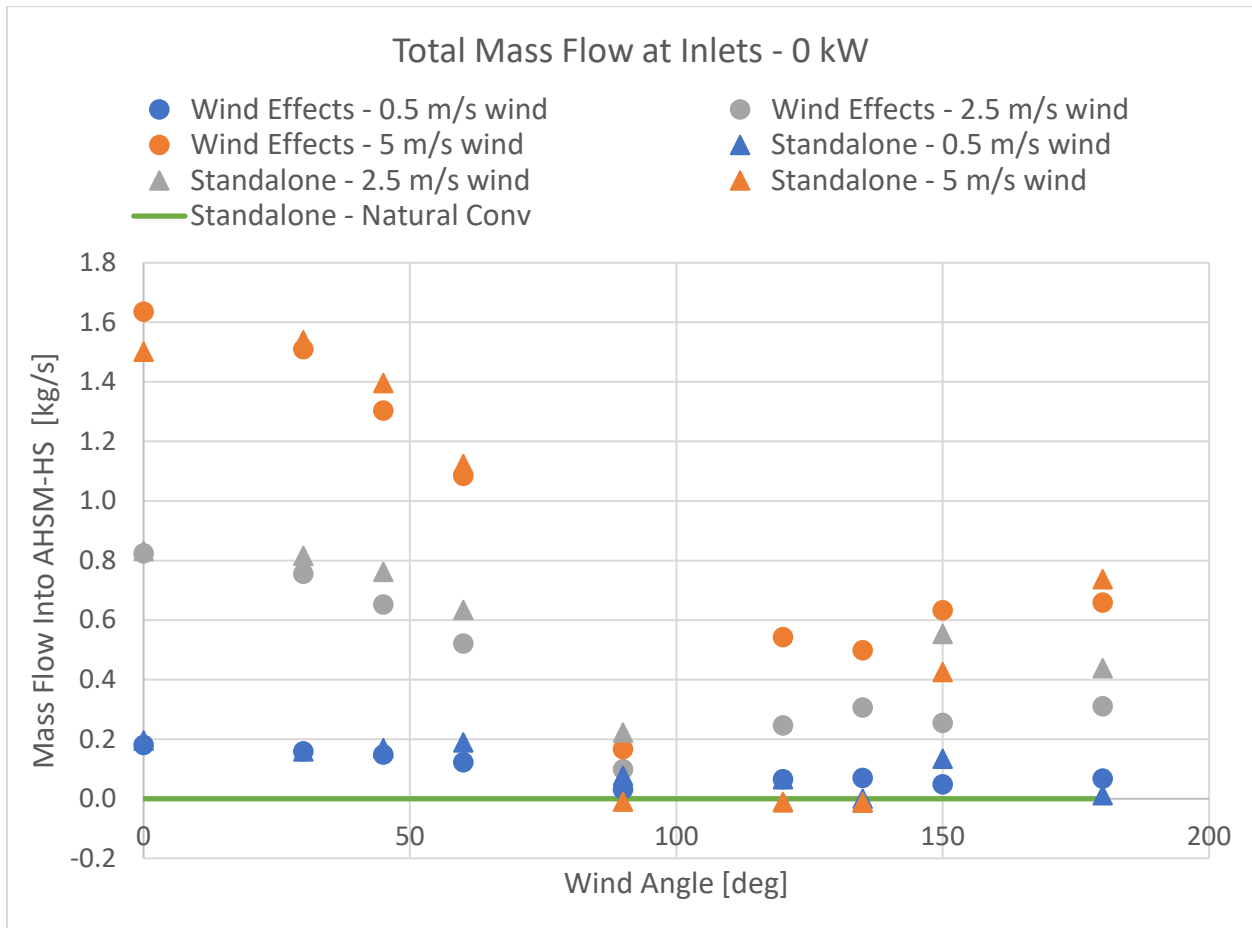


Figure 4-33. Total Mass Flow at AHSM-HS Inlets at 0 kW

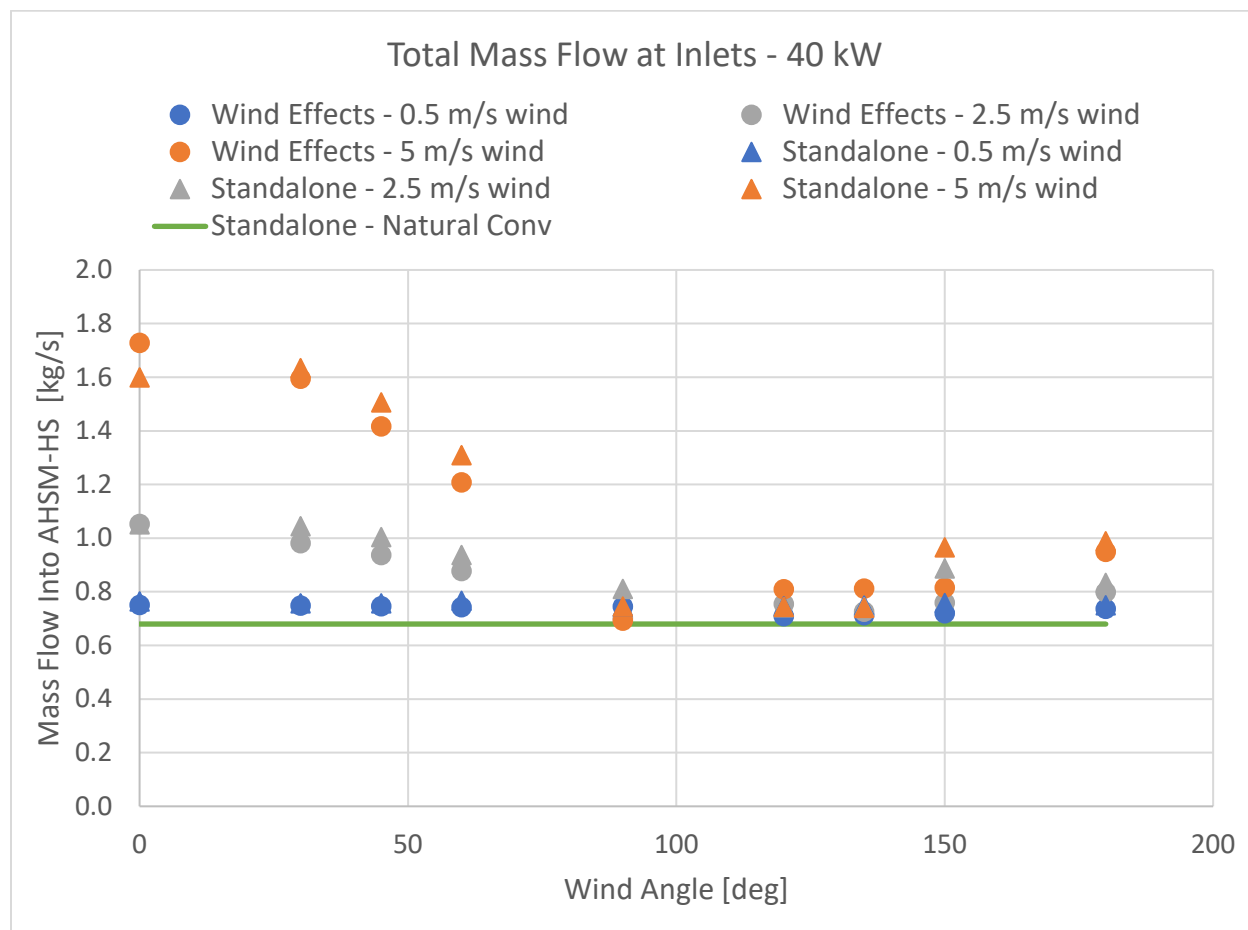


Figure 4-34. Total Mass Flow at AHSM-HS Inlets at 40 kW

4.7.5 Three AHSM-HS Wind Effects Models

A STAR-CCM+ and FDS three-module wind effects model was constructed following the same methodology applied to the single AHSM-HS module wind effects models described in Section 4.6.1 and Section 4.6.2.

A limited number of cases were run with the three-module wind effects models to verify that the pressure difference method was working on the larger model. The limited number of cases included a 5 m/s wind at wind angles of 0-degrees and 45-degrees. Figure 4-35 shows the velocity vector field around the three-module FDS model at 5 m/s and 0-degrees. Figure 4-36 shows a vector velocity plot for the three-module STAR-CCM+ model at the elevation of the inlets at a 5 m/s wind speed and 0-degree wind angle. For the three-module STAR-CCM+ wind effects model, all modules assumed no thermal loads (i.e., no canister heat load or solar loadings). Table 4-7 lists the resulting pressure differences at each inlet. Figure 4-37 shows the inlet and outlet numbering scheme for the three-module model. Even though no heat load was applied to the canisters, inlets 1 and 2 correspond to the high heat module, inlets 3 and 4 correspond to the no heat module, and inlets 5 and 6 correspond to the low heat module.

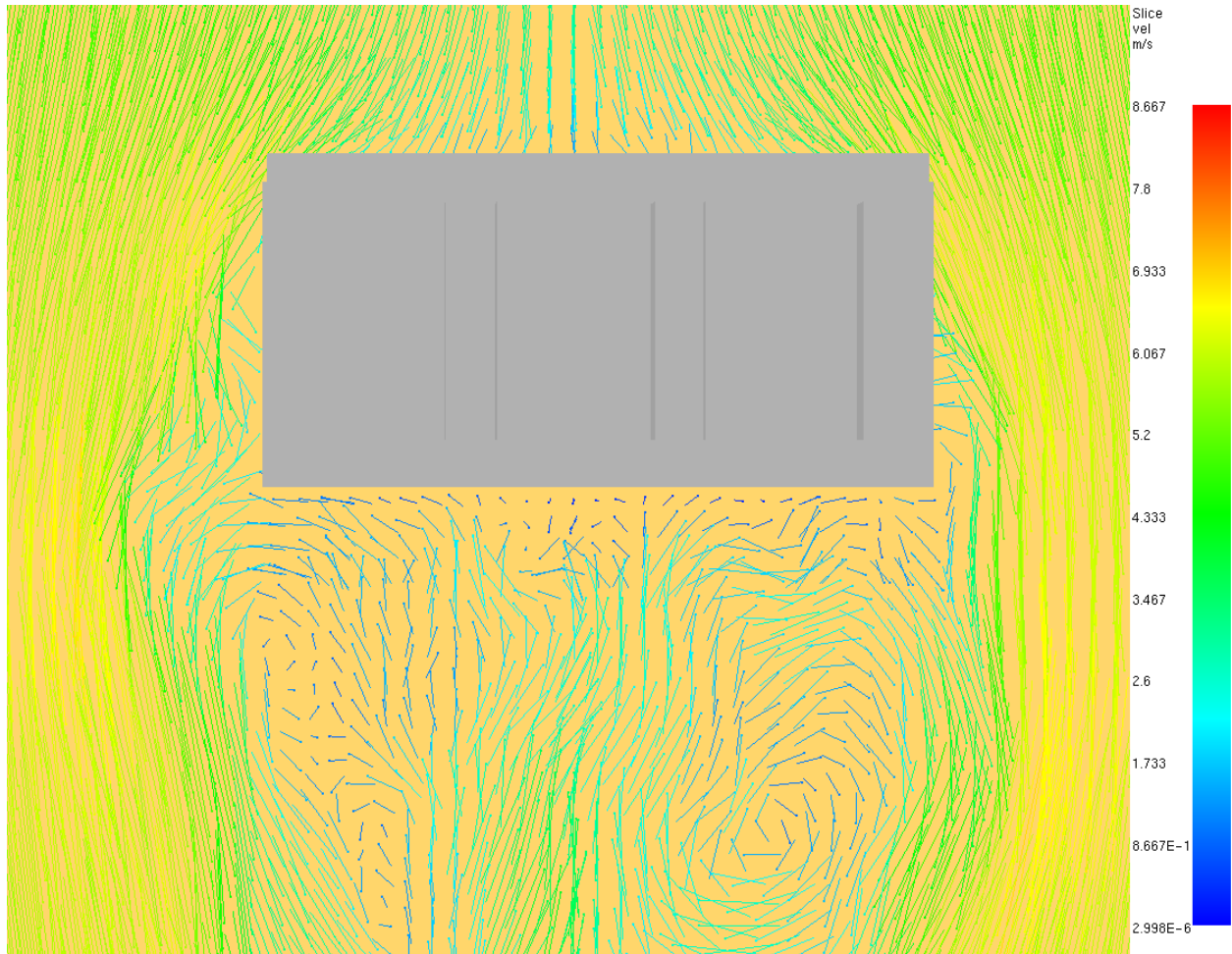


Figure 4-35. Velocity Vector Plot for Flow Around the three-Module AHSM-HS in FDS at 5 m/s and 0-Degrees

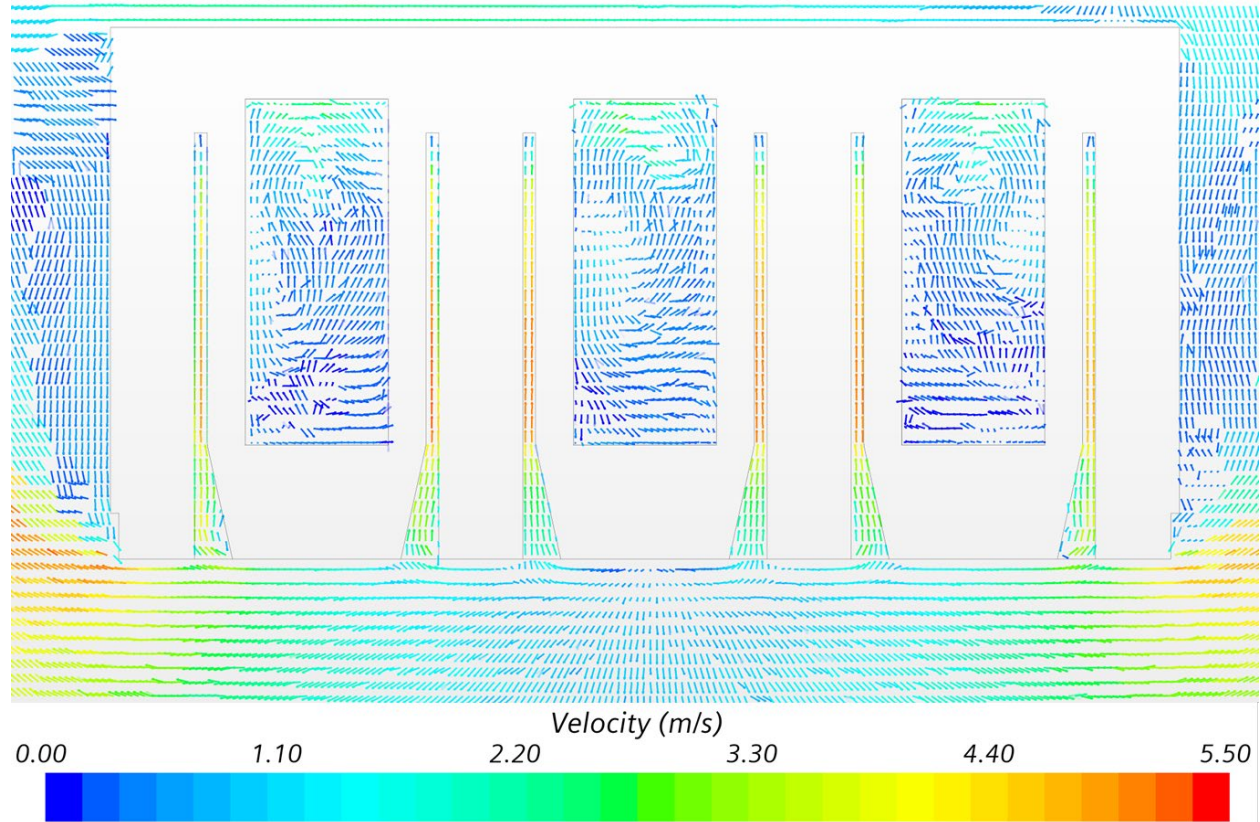


Figure 4-36. Velocity Vector Plot for Flow at the Inlets Elevation for the three-Module AHSM-HS in STAR-CCM+ at 5 m/s and 0-Degrees

Table 4-7. FDS Three-Module Wind Effects Pressure Difference Results

Wind Direction	Wind Speed	ΔP Inlet 1	ΔP Inlet 2	ΔP Inlet 3	ΔP Inlet 4	ΔP Inlet 5	ΔP Inlet 6
[deg]	[m/s]	[Pa]	[Pa]	[Pa]	[Pa]	[Pa]	[Pa]
0	5	23.5	22.7	28.6	29.4	28.8	28.6
45	5	10.3	23.9	14.8	22.6	10.2	22.6

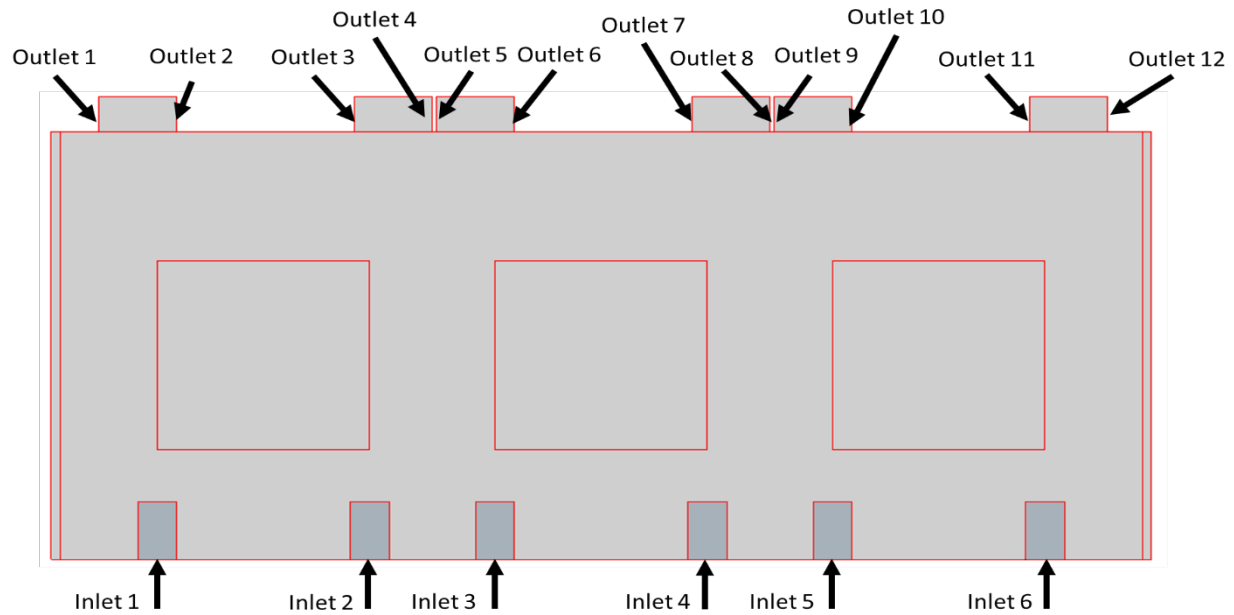


Figure 4-37. Three-Module AHSM-HS Inlet and Outlet Numbering Scheme

The pressure differences given in Table 4-7 were applied to the inlets of the stand-alone three-module AHSM-HS 32PTH2 heater assembly model for the wind speed and angles given in the table. The stand-alone model was run assuming no thermal loads (0 kW) for any of the modules. Figure 4-38 compares the resulting air flow at the inlets for the STAR-CCM+ wind effects and stand-alone three-module models. The natural convection flow air flow line on Figure 4-38 equals zero since there are no thermal loads to drive natural convection. The stand-alone model results slightly overpredict air flow entering the modules compared to the wind effects model. The 0-degree cases are within 0.5 kg/s and the 45-degree cases are within 0.25 kg/s between the two models. Future work will look at running a full suite of cases with the wind effects and stand-alone 3-module models.

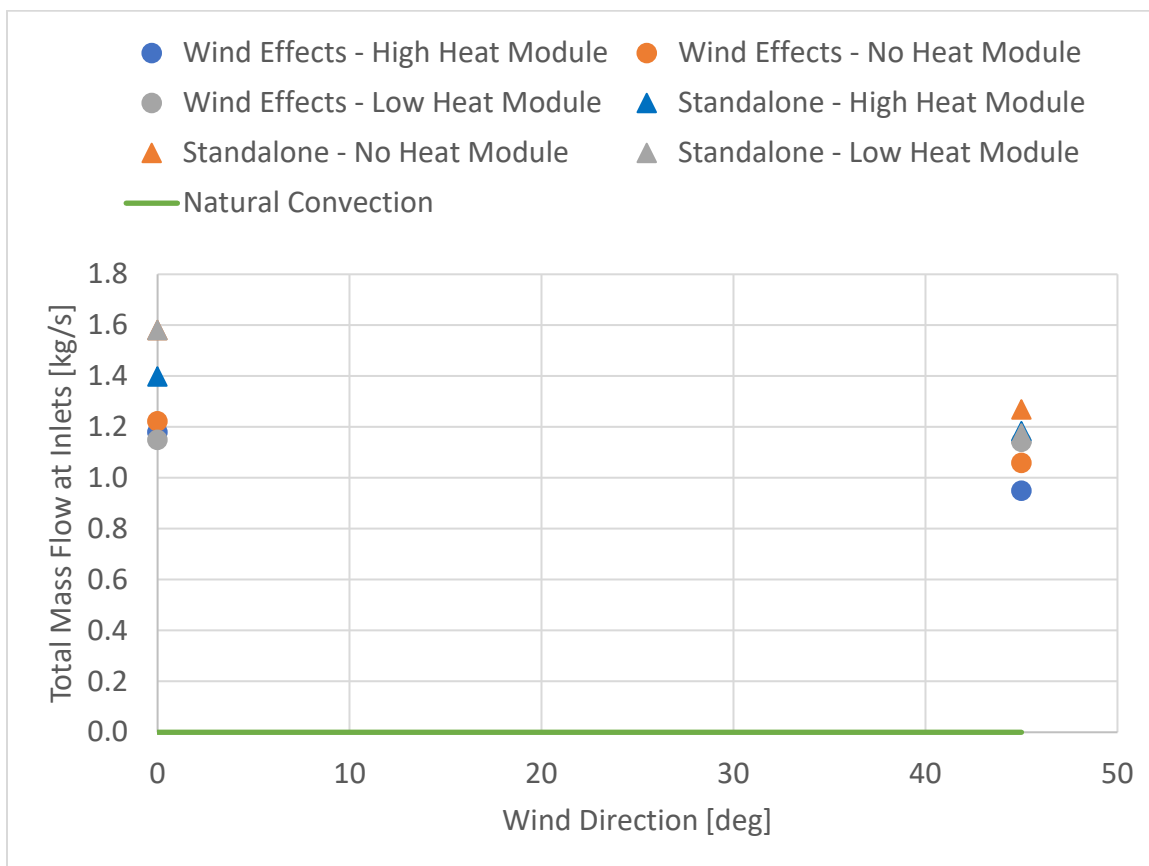


Figure 4-38. Total Mass Flow at Three-Module AHSM-HS Inlets at 0 kW

4.8 Uncertainty Analysis

An uncertainty analysis was run with the single AHSM-HS heater assembly model to look at the uncertainty in the deposition predictions and provide a range over which the predicted deposition efficiency is expected to vary due to environmental variance (i.e., wind speed and direction, ambient temperature, RH). It is important to note that the deposition models are unvalidated and have inputs such as particle size and distribution that have not been well characterized. This uncertain analysis is intended to provide a modeling methodology for applying variance captured in a transient site model (such as changing wind speed and direction) to the steady state standalone deposition model. All results are preliminary and will need to be reconsidered once a site has been identified and characterized. The uncertainty analysis was run using the software Dakota (Dakota 2021) as described in Section 2.4.4.

Four different perturbation parameters related to the external environment surrounding the storage module were used for the LHS analysis and are listed in Table 4-8. The parameters were assumed to have a uniform distribution based on the minimum and maximum values listed in Table 4-8. The minimum wind speed corresponds to natural convection flow only. The wind speed and angle ranges used the inlet pressures given in Table 4-6 from the FDS single AHSM-HS wind effects model. These ranges and the uniformity assumption are not representative of a specific site. Once a site has been selected, meteorological data could be used to provide a more realistic range and distribution for wind speed and angle (which may be dependent variables). The ambient temperature and RH values were based on an expected range for a coastal site.

Table 4-8. Perturbation Parameters

Parameter	Min	Max	Units
Wind Speed	0	5	m/s
Wind Angle	0	180	deg
Ambient Temperature	45	85	F
RH	50	80	%

Three different LHS analyses were run, one with no heat load (solar loadings are the only thermal loads driving natural convection), one with the low heat load applied (10 kW), and one with the high heat load applied (40 kW). For all LHS analyses, 50 cases were run.

4.8.1 Deposition Efficiency Results

The resulting deposition efficiency predicted by the STAR-CCM+ single AHSM-HS heater assembly model is shown in Figure 4-39 for the total and canister deposition. The error bars shown on the plots for each analysis represent the potential range over which deposition may vary due to variation in environmental conditions in the model inputs. Results show the heated canisters both had a mean canister deposition around 10%. The non-heated canister had a slightly lower mean canister deposition at 9% but had a larger range over which that value could vary. Air flow in the non-heated canister will be mainly driven by wind. The variance is smaller for the high heat load canister at 40 kW, meaning smaller error bars, compared to the low- and non-heated canisters. This may be due to the higher natural convection air flow, meaning higher mass flow rates at lower wind speeds than the lower heat and no heat canister. The maximum error bar range for the canister deposition varied from +10% to -7% in the no heat canister and had a minimum range from +6% to -5% in the 40 kW canister.

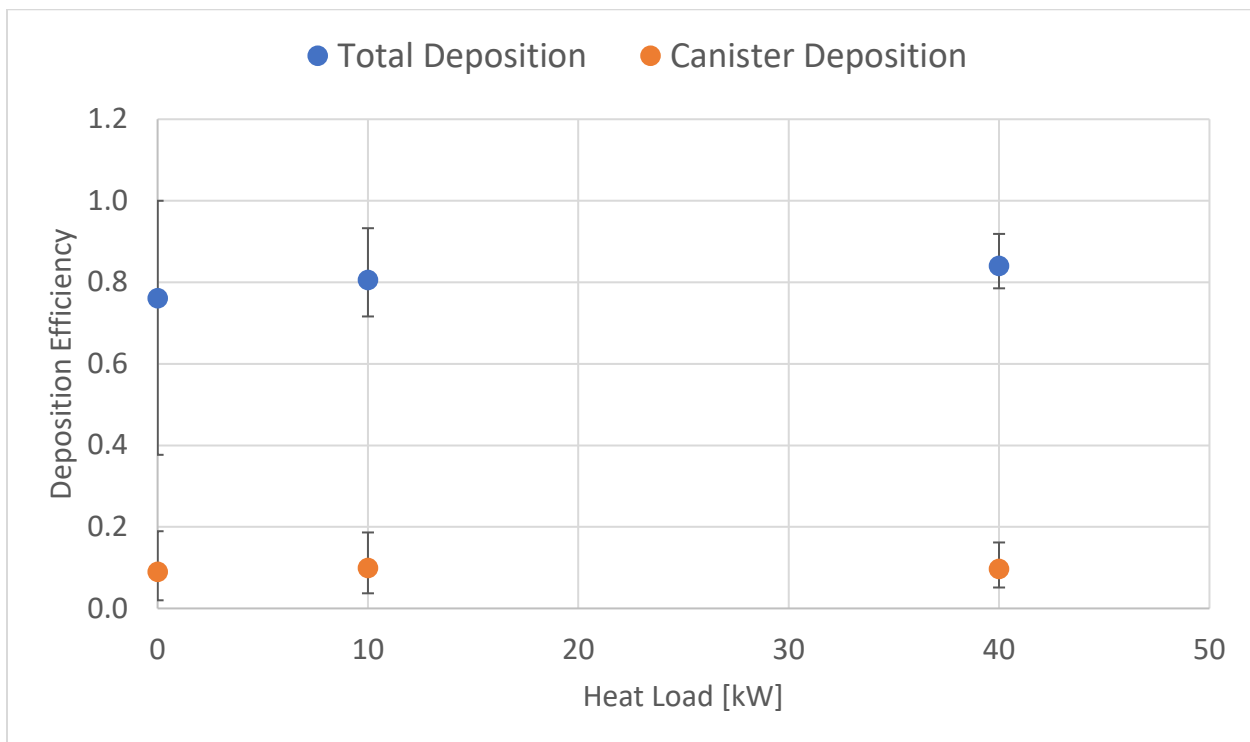


Figure 4-39. LHS Analysis Results for Total and Canister Deposition

4.8.2 Shear Velocity Results

Results from the LHS analysis were also used to look at the potential impact of particle resuspension. The model currently assumes a very simple “stuck” surface condition, where if the particle contacts the surface, it is indefinitely stuck to the surface. Section 4.5 computed a critical shear velocity curve based on particle detachment theory. The LHS analysis was used to look at the canister surface shear velocity and particles deposited at the planned sampling locations for the CDFD project. The sampling locations are shown in Figure 4-40 and described in Knight et al. (2023). Figure 4-41 shows the resulting wall shear velocity and particle deposition at the sampling locations for the low heat load canister at natural convection flow conditions (ambient temperature of 63.4°F and RH of 66.9%).



Figure 4-40. Proposed Sampling Layout from Knight et al. (2023)

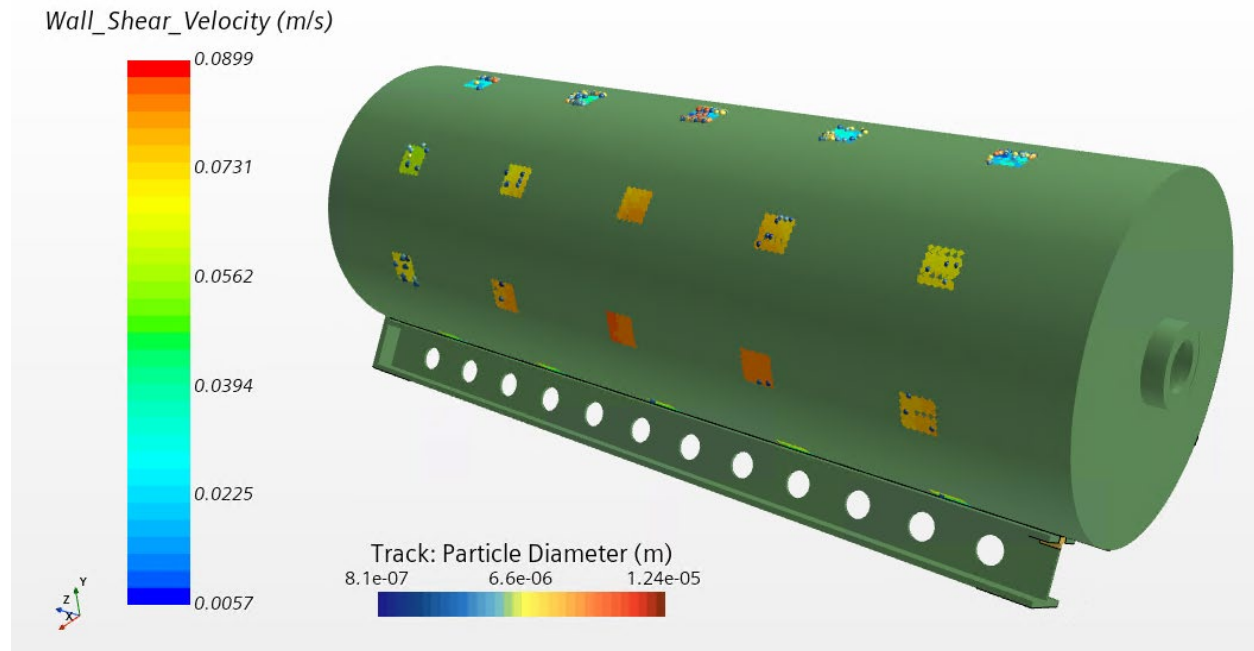


Figure 4-41. Resulting Plot for Particle Deposition and Shear Velocity at the Sampling Locations for 10 kW Heat Load and Natural Convection Flow

There are a total of 20 proposed sampling locations, with 5 sampling locations along the axial length of the canister at 4 different angular locations. The STAR-CCM+ model included an additional 5 sampling locations, for a total of 25 sampling locations based on an older sampling location layout (the extra 5 sampling locations were located along the radial bottom of the canister). Within the STAR-CCM+ model, the following naming convention is used to describe the sampling locations: the axial sampling locations are numbered from 1 to 5 with 1 corresponding to the sample closest to the bottom of the canister and 5 being the furthest from the bottom of the canister, and the angular location of the sample is given with 0-degrees corresponding to the top of the canister. For example, the sampling label “Sone-0deg” corresponds to the sample located at the top of the canister and closest to the bottom of the canister. Dakota computed the mean shear velocity and maximum particle diameter deposited at each sampling location and the expected variance associated with each sampling location based on the LHS analysis for the 50 samples. Figure 4-42 through Figure 4-44 plots the sampling location results for each heat load and compares against the critical shear velocity calculated in Section 4.3. The DMT Rolling Burst Smooth results were used for the critical shear velocity curve for conservatism since it provided lower critical shear velocity values. The results show that the sampling locations along the radial bottom of the canister at 180-degrees have the highest probability of being impacted by particle resuspension.

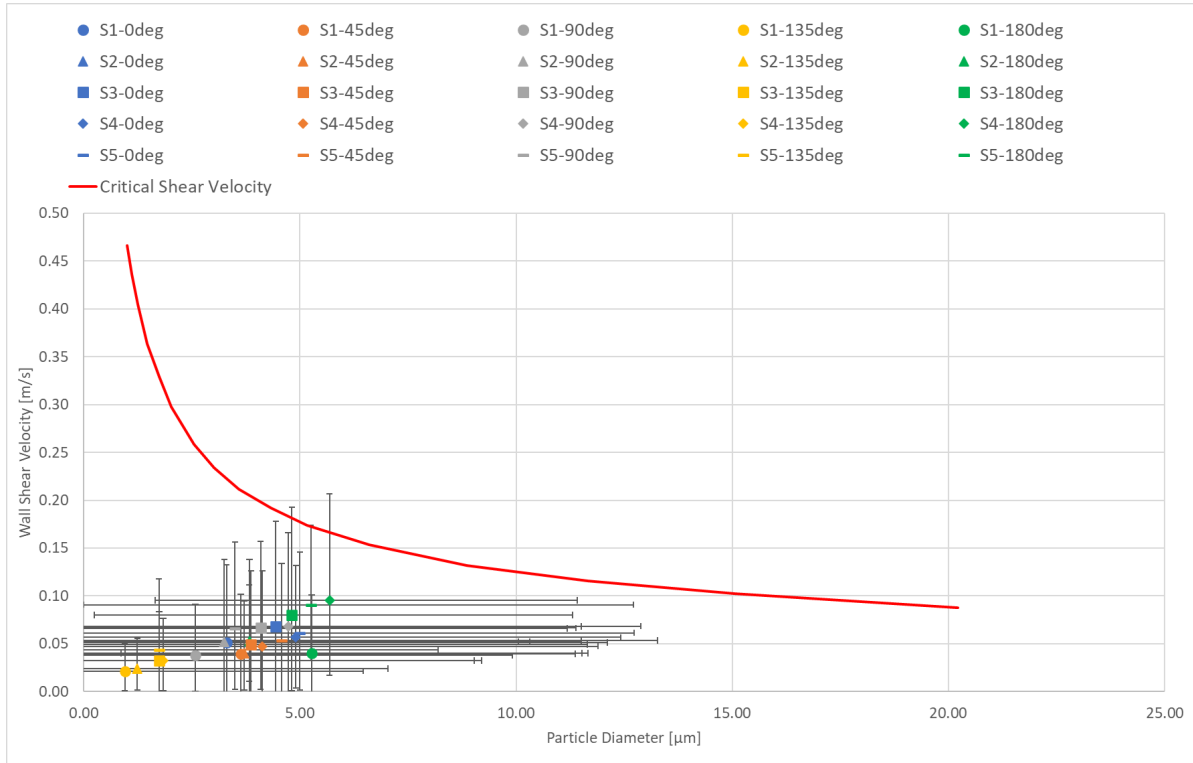


Figure 4-42. LHS Analysis 0 kW Heat Load Results for Shear Velocity

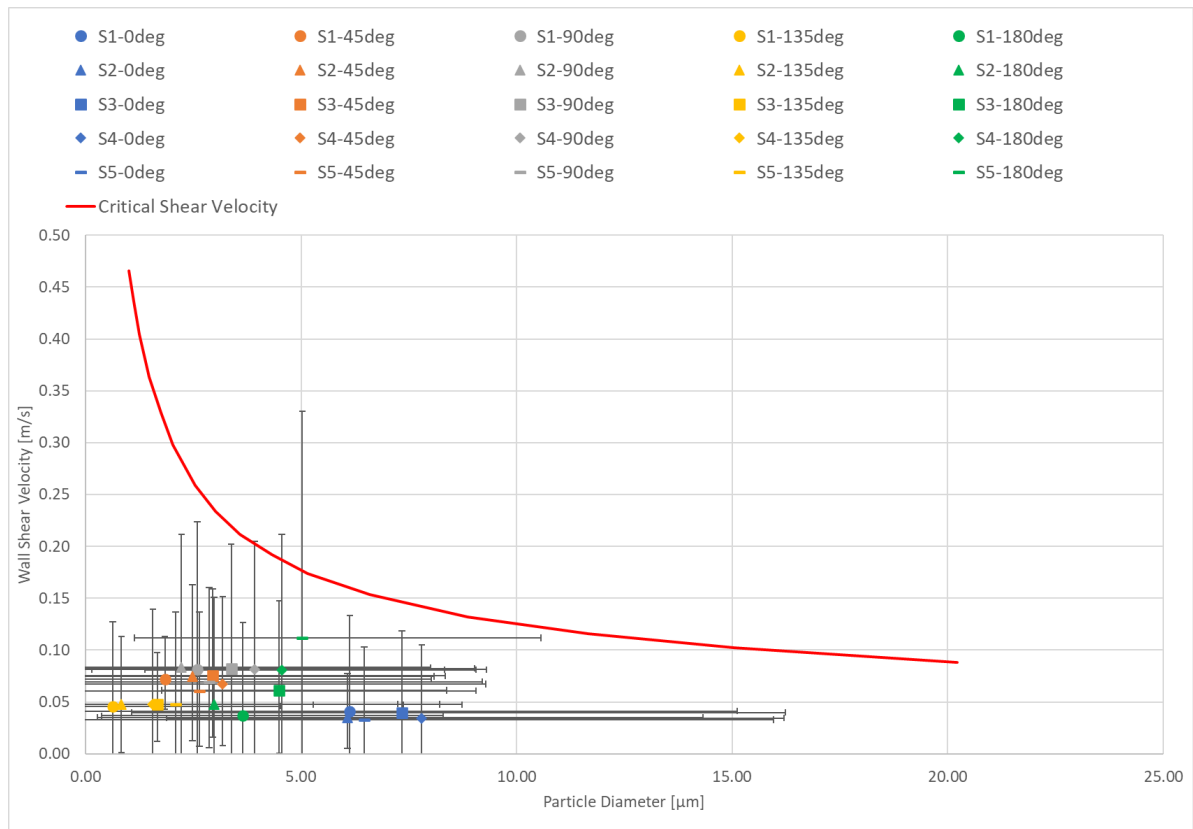


Figure 4-43. LHS Analysis 10 kW Heat Load Results for Shear Velocity

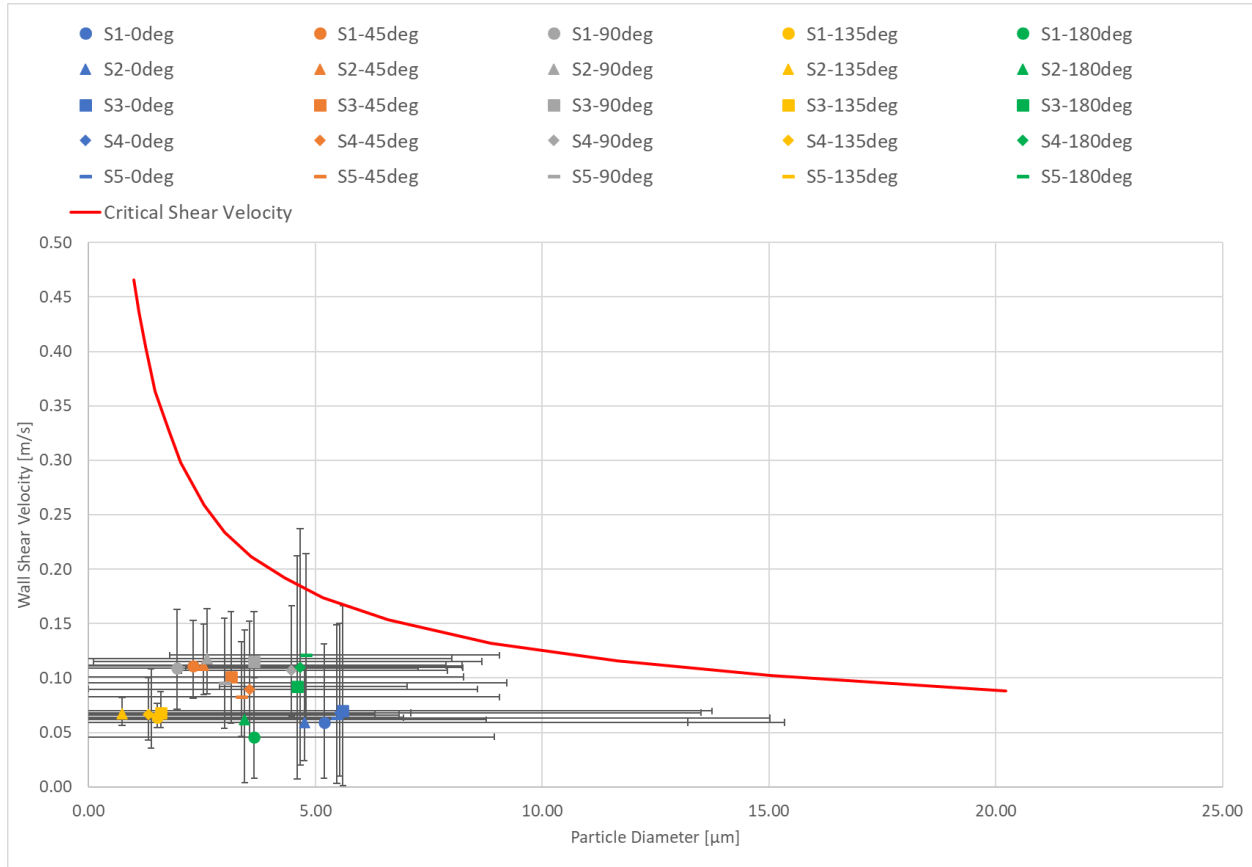


Figure 4-44. LHS Analysis 40 kW Heat Load Results for Shear Velocity

Figure 4-45 through Figure 4-47 plots the maximum deposited diameter versus shear velocity at each sample for all 50 cases run with the LHS analysis for each heated canister condition. The no heat canister had ~ 1% of particles exceed the critical shear velocity, the low heat canister had ~ 2% of particles exceed the critical shear velocity, and the high heat canister had ~ 1% of particles exceed the critical shear velocity. These results are preliminary and will be dependent on characterizing a particle size and distribution once a CFD site has been selected. Future work will continue to investigate the impact of particle resuspension.

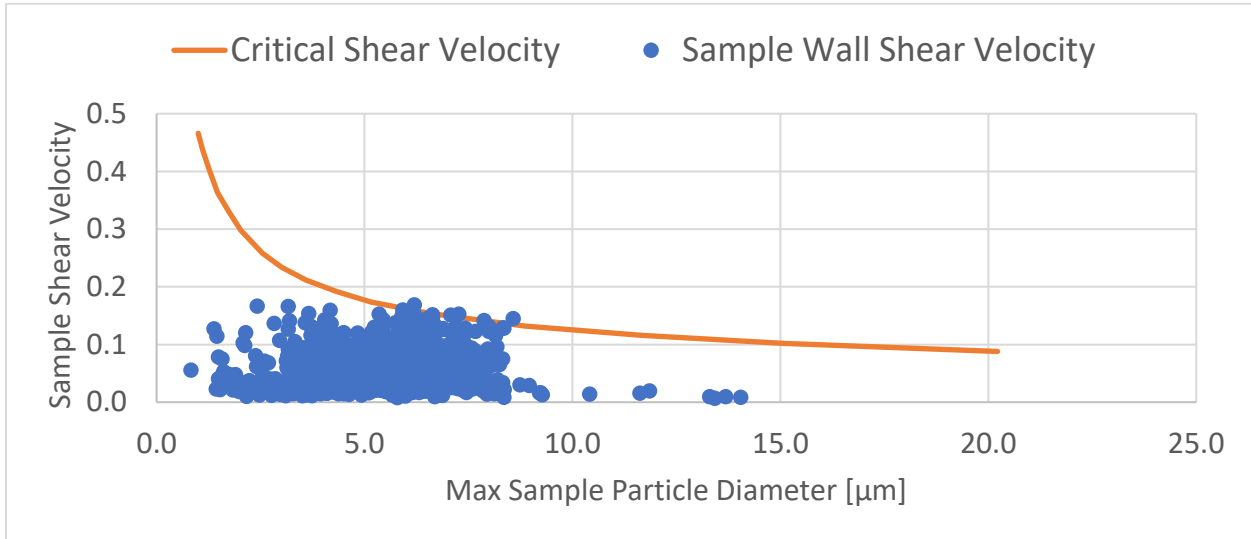


Figure 4-45. 0 kW Heat Load Results for Particle Resuspension

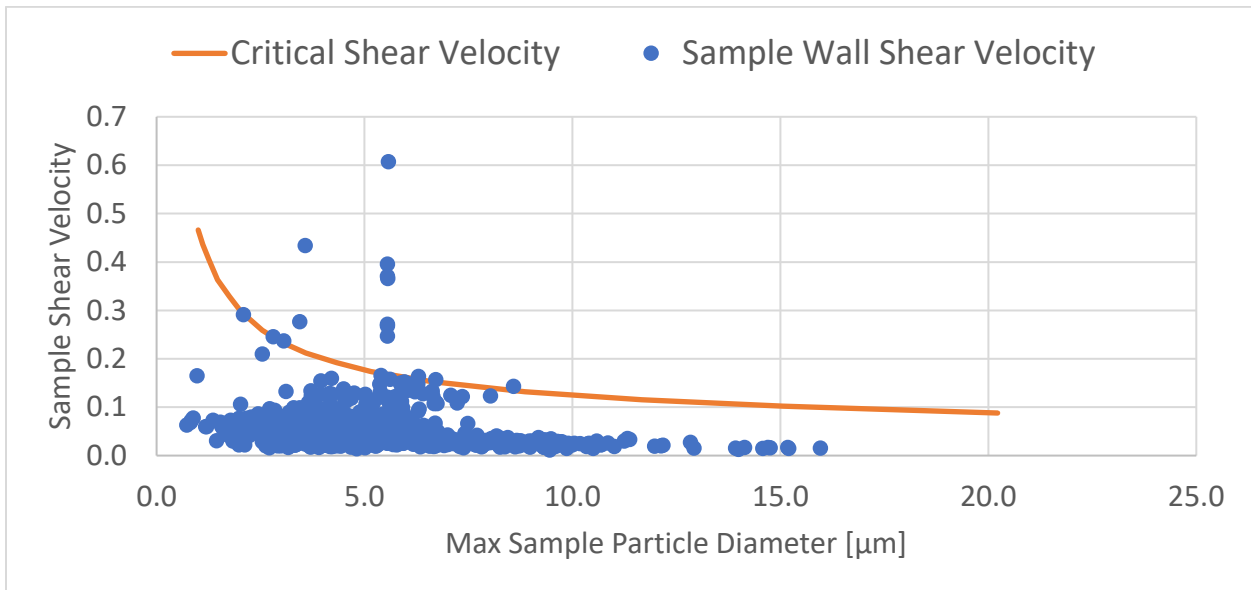


Figure 4-46. 10 kW Heat Load Results for Particle Resuspension

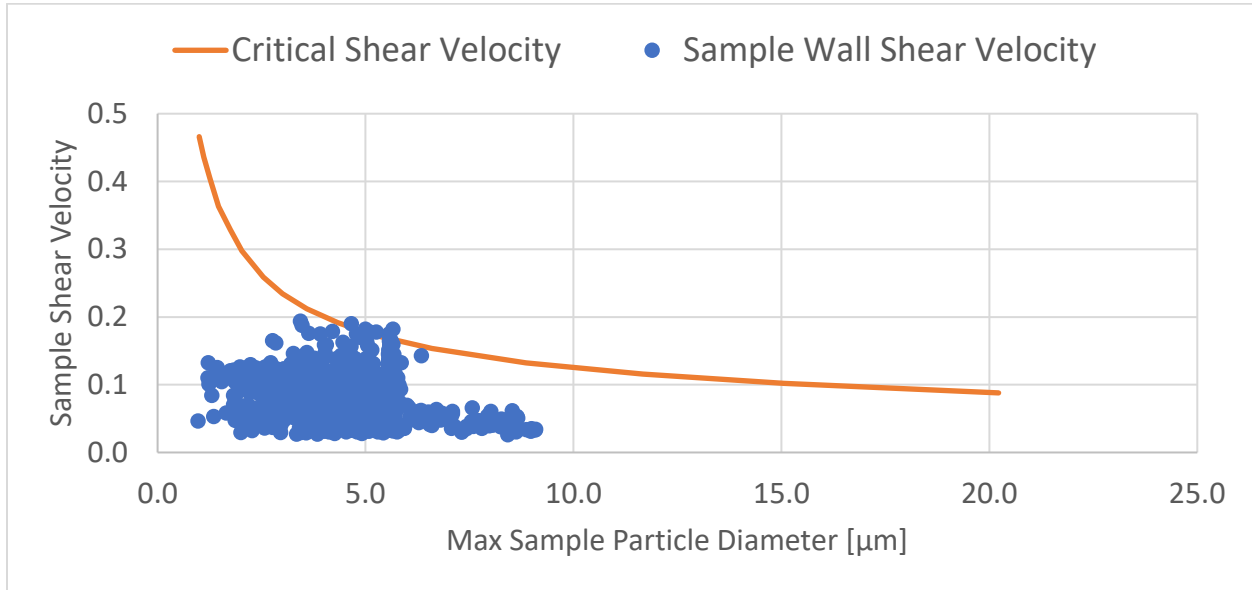


Figure 4-47. 40 kW Heat Load Results for Particle Resuspension

5. CONCLUSIONS AND RECOMMENDATIONS

Thermal and deposition models continue to be developed for the CDFD project. These models are preliminary, and development of the models will continue. Thermal modeling was used to help SNL design an electrical heater that will mimic the SNF assemblies in the 32PTH2 canisters and provide prototypic canister temperatures. Both the baseline model with SNF assemblies and the model with heater assemblies were updated to include tapered inlets and realistic canister to basket gap measurements provided by SNL. The heater assembly model was also updated to include the latest planned loading configuration for the electrical heaters and measured heater rod emissivities provided by SNL. Temperature comparison plots show that the canister surface temperatures between the baseline SNF model and heater assembly models are similar.

Thermal transients were also run with the SNF baseline and heater assembly models to compare the thermal response of the canister to changes that would affect the temperature profile of the canister surface, such as ambient temperature or air flow into the storage module. There are differences in canister mass between a 32PTH2 canister loaded with electrical heaters instead of SNF, with the SNF canister estimated to be 2 times heavier than the heater assembly canister. Transient cases were run looking at both changing ambient temperatures and changes in the air flow around the storage module (i.e., wind conditions). The modeling results indicate that there is no significant difference in the thermal response of the system with electrical heaters compared to a system loaded with SNF within a 12-hour time frame (environment conditions are expected to fluctuate between daytime and evening conditions). Based on the thermal transient results, there is no need to try to account for any canister mass differences with the control system for the electrical heaters.

The canister-only model with prototypic heaters was used to simulate current SNL testing. Cases were run to simulate heat load test conditions ranging from 4.8 kW to 35 kW. The resulting overall peak canister shell and peak heater temperatures predicted by the model compared well with the peak test measurements. An uncertainty analysis was run with the canister-only model at 9.6 kW and 35 kW to determine the uncertainty in the temperature predictions and provide a range over which the predicted temperatures are expected to vary. For the 35 kW case, most of the resulting canister surface temperature ranges predicted by the model were within range of the measured thermocouple (TC) value. The model predicted slightly higher canister surface temperatures for the 9.6 kW case compared to the measured TC data. Both heat loads showed the same temperature profile as the experiment.

The deposition models were updated with the latest thermal models. The deposition efficiency calculation for the steady state deposition models was updated to use the solid particle mass for calculating efficiency since the liquid droplet mass will be changing as it moves through the heated overpack and evaporates. Steady state simulations were run using both the SNF baseline and heater assembly models, and the resulting predicted canister deposition is within 1.5% between the SNF and heater assembly model at both the low heat load (10 kW) and high heat load (40 kW). An uncertainty analysis was run with the AHSM-HS heater assembly model to determine the uncertainty in the deposition predictions and provide a range over which the predicted deposition efficiency is expected to vary due to environmental variance (i.e., wind speed and direction, ambient temperature, RH). The resulting mean canister deposition efficiency was predicted to be 10% with a +9%/–6% variance.

A preliminary site model was constructed with FDS to support future ambient aerosol characterization for the CDFD program. The long-term plan is to develop a site model to provide boundary conditions, such as wind speed and direction, to the detailed stand-alone deposition models of the AHSM-HS and 32PTH2 canisters. At the time of this report, no official site has been selected for the CDFD project.

A modeling methodology was demonstrated for connecting the site model and stand-alone AHSM-HS models through the pressure difference created at the inlets and outlets. To demonstrate how to account for wind in the stand-alone model, two different wind effects models were developed: a STAR-CCM+ wind effects model that included air flow through the AHSM-HS module and an FDS wind effects model

that modeled the external environment surrounding the AHSM-HS but did not model flow through the module. The FDS wind effects model with no flow through AHSM-HS will be more representative of the FDS site model and will be used to feed boundary conditions to the stand-alone STAR-CCM+ AHSM-HS heater assembly model. The air flow through the STAR-CCM+ wind effects model was compared to the resulting air flow through the AHSM-HS with the stand-alone model and FDS pressure boundary conditions. Results showed that the FDS model pressure boundary conditions captured flow effects at most wind speeds and angles. This pressure difference method will be used to feed boundary conditions from the site model to the stand-alone AHSM-HS models.

An approach for starting to look at the impact of particle resuspension was developed based on particle detachment theory. A critical shear velocity curve for SSAs was computed. Preliminary modeling shows that a small number of particles may be impacted by particle resuspension, but further work is needed to explore this topic. These results are preliminary and will be dependent on characterizing a particle size and distribution once a CDFD site has been selected.

The PNNL deposition models have not been validated, and though the CDFD project will help validate the models, additional experimental data and modeling studies are recommended for the development of the deposition modeling.

To continue development of the thermal and deposition models, the following activities are recommended:

- Continue to simulate thermal testing of the canister at SNL and validate the thermal model.
 - Update the AHSM-HS 32PTH2 heater assembly models with the CDFD specific roller rail design.
 - Add more realistic solar loading. This will be important for the no heat canister since solar loadings are the only thermal loads driving natural convection.
 - Develop a site model once a specific site has been selected, using lessons learned from the current site modeling efforts.
 - Validate the FDS site model against data collected during the ambient aerosol characterization campaign.
 - Update deposition models with data gathered during the planned ambient aerosol characterization campaign.
 - Continue to explore adding particle resuspension to the deposition models.
 - Potential deposition modeling comparisons with deposition measurements taken at site inspections.
 - Validate the deposition model with benchtop testing (NEUP with Clemson University).
 - Continue to explore adding various particle forces and deposition mechanisms to the deposition model.
-

6. REFERENCES

- American Elements (2022). “Sodium chloride.” URL <https://www.americanelements.com/sodium-chloride-7647-14-5>.
- AZO Materials (2022). “Properties: Stainless steel - grade 304 (UNS S30400).” URL <https://www.azom.com/properties.aspx?ArticleID=965>.
- babaknasr (2019, October). “Particle-Detachment-Theory.” URL <https://github.com/babaknasr/Particle-Detachment-Theory>. GitHub repository, commit 0dfd0cd5.
- Babel, M. and B. Schreiber (2014). „Geochemistry of Evaporites and Evolution of Seawater.” In *Treatise on Geochemistry*, 483–560. Elsevier.
- Bergstörn, L. (1997, July). “Hamaker constants of inorganic materials.” *Advances in Colloid and Interface Science* 70, 125–169.
- Bryan, C. R. and D. G. Enos (2014, July). *Analysis of dust samples collected from spent nuclear fuel interim storage containers at Hope Creek, Delaware, and Diablo Canyon, California*. Technical Report SAND2014-16383, Sandia National Lab. (SNL-NM), Albuquerque, NM (United States).
- Bryan, C. R. and D. G. Enos (2016, March). *Understanding the risk of chloride induced stress corrosion cracking of interim storage containers for the dry storage of spent nuclear fuel: Evolution of brine chemistry on the container surface*. OnePetro.
- Bryan, C. R., A. W. Knight, R. M. Katona, A. C. Sanchez, E. J. Schindelholz, and R. F. Schaller (2022, June). “Physical and chemical properties of sea salt deliquescent brines as a function of temperature and relative humidity.” *Science of The Total Environment* 824, 154462.
- Dassault Systemes SolidWorks Corp. 2021. SolidWorks Premium 2021 (computer software). Waltham, Massachusetts: Dassault Systèmes.
- Dakota. 2021. Dakota 6.15 (computer software). Albuquerque, New Mexico: Sandia National Laboratories.
- Fascitelli, D. G., S. G. Durbin, R. J. M. Pulido, S. R. Suffield, J. A. Fort, and B. J. Jensen. 2022. *Status Update for the Canister Deposition Field Demonstration*. Sandia National Laboratories SAND2022-8167. Albuquerque, New Mexico.
- Fascitelli, D. G. and S. G. Durbin. 2023. *Predeployment Progress of the Canister Deposition Field Demonstration*. Sandia National Laboratories SAND202three-04194. Albuquerque, New Mexico.
- Fort, J. A., D. J. Richmond, J. M. Cuta, and S. R. Suffield. 2019. *Thermal Modeling of the TN-32B Cask for the High Burnup Spent Fuel Data Project*. Pacific National Laboratories PNNL-28915. Richland, Washington.
- Jensen, P. J., S. R. Suffield, C. L. Grant, C. J. Spits, and J. T. Simmons. 2020a. *Preliminary Deposition Modeling: For Determining the Deposition of Corrosive Contaminants on SNF Canisters*. Pacific Northwest National Laboratory PNNL-29620. Richland, Washington.
- Jensen, P. J., S. R. Suffield, and B. J. Jensen. 2020b. *Status Update: Deposition Modeling For SNF Canister CISCC*. Pacific Northwest National Laboratory PNNL-30793. Richland, Washington.
- Knight, A.W., D.G. Fascitelli, C.R. Bryan, S.G. Durbin, S. Verma, M. Maguire, and B. Nation. 2023. *FY23 Update: Surface Sampling Activities for the Canister Deposition Field Demonstration*. Sandia National Laboratories. SAND202three-01875. Albuquerque, New Mexico.
- Li, X., J. Liu, C. Li, J. Hong, D. Wang. 2021. “Research on the influence of air-gap eccentricity on the temperature field of a motorized spindle.” *Mechanical Sciences* 12: 109–122. DOI: 10.5194/ms-12-109-2021.
- McGrattan, K., R. McDermott, C. Weinschenk, and G. Forney. 2013. *Fire Dynamics Simulator Users Guide, Sixth Edition*. National Institute of Standards and Technology Special Publication (NIST SP) 1019. Gaithersburg, MD.
- McGrattan, K., R. McDermott, C. Weinschenk, and K. Overholt. 2017. *Fire Dynamics Simulator; Technical Reference Guide, Volume 1: Mathematical Model*. National Institute of Standards and Technology Special Publication (NIST SP) 1018-1. Gaithersburg, MD.
-

- Nasr, B., S. Dhaniyala, and G. Ahmadi (2017, January). Chapter 2 - particle resuspension from surfaces: Overview of theoretical models and experimental data. In R. Kohli and K. L. Mittal (Eds.), *Developments in Surface Contamination and Cleaning: Types of Contamination and Contamination Resources*, 55–84. William Andrew Publishing.
- NIST. 2018. “Advanced Fire Modeling.” National Institute of Standards and Technology. Accessed 07/13/2021. <https://www.nist.gov/programs-projects/advanced-fire-modeling>.
- Richmond, D. J., S. R. Suffield, J. A. Fort, and M. E. Higley. 2022. *Uncertainty in Thermal Modeling of Spent Nuclear Fuel Casks*. Pacific National Laboratories PNNL-33409. Richland, Washington.
- Shurtz, R.C., 2018. *Total Hemispherical Emissivity of Metals Applicable to Radiant Heat Testing*. Sandia National Laboratories SAND2018-13271. Albuquerque, New Mexico.
- Siemens PLM Software. 2022. STAR-CCM+ 17.06 (computer software). Plano, Texas: Siemens PLM Software.
- Soltani, M. and G. Ahmadi (1994, January). On particle adhesion and removal mechanisms in turbulent flows. *Journal of Adhesion Science and Technology* 8(7): 763–785.
- Suffield, S. R., D. J. Richmond, and J. A. Fort. 2019. *Modeling of the of the Boiling Water Reactor Dry Cask Simulator*. Pacific National Laboratories PNNL-28424. Richland, Washington.
- Suffield, S. R., D. J. Richmond, B. J. Jensen, J. A. Fort, and C. Grant. 2020. *Modeling of the of the Horizontal Boiling Water Reactor Dry Cask Simulator*. Pacific National Laboratories PNNL-30145. Richland, Washington.
- Suffield, S. R., J. A. Fort, P. J. Jensen, W. A. Perkins, B. J. Jensen, C. Grant, R. Ekre, B. D. Hanson, and S. B. Ross. 2021. *Thermal and Deposition Modeling of the Canister Deposition Field Demonstration*. Pacific Northwest National Laboratory PNNL-31882. Richland, Washington.
- Suffield, S. R., J. A. Fort, B.J. Jensen, W. A. Perkins, P. J. Jensen, and C. Grant. 2022. *Update of Thermal and Deposition Modeling for the Canister Deposition Field Demonstration*. Pacific Northwest National Laboratory PNNL-33254. Richland, Washington.
- United States Nuclear Regulatory Commission (NRC). 2012. *Potential Chloride-Induced Stress Corrosion Cracking of Austenitic Stainless Steel and Maintenance of Dry Cask Storage System Canisters*.
- Visser, J. (1972, December). On Hamaker constants: A comparison between Hamaker constants and Lifshitz-van der Waals constants. *Advances in Colloid and Interface Science* 3 (4): 331–363.
- Zakowski, K., A. Narozny, M. Szocinski, and K. Darowicki. 2014. “Influence of water salinity on corrosion risk – the case of the southern Baltic Sea coast.” *Eviron Monit Assess* 186: 4871–4879. DOI: 10.1007/s10660-014-3744-3.
-